Polimery w Medycynie

Polymers in Medicine

**WROCLAW
MEDICAL UNIVERSITY**

Polimery w Medycynie
Polymers in Medicine

"Polymers in Medicine" is an independent, multidisciplinary forum to exchange scientific and clinical information, which publishes original papers (technical, analytical, experimental, clinical), preliminary reports and reviews regarding the use of polymers (natural and synthetic) and biomaterials in different specialties of medicine (biochemistry, clinical medicine, pharmacology, dentistry, implantology), biotechnology and veterinary science.

Address of Editorial Office

Marcinkowskiego 2–6
50-368 Wrocław, Poland
Tel.: +48 71 784 11 33
E-mail: redakcja@umed.wroc.pl

Publisher

Wroclaw Medical University
Wybrzeże L. Pasteura 1
50-367 Wrocław, Poland

Online edition is the original version of the journal

Editorial Policy

Contents

Phytosynthesis of zinc oxide nanoparticles using methanol extract of *Senna alata* leaf: Characterization, optimization, antimicrobial properties, and its application in cold cream formulation

Bukola Christianah Adebayo-Tayo[1,A,D–F], Samuel O. Borode[1,B–D,F], Olusola Ademola Olaniyi[2,A,E,F]

[1] Department of Microbiology, University of Ibadan, Nigeria

[2] Department of Mathematics and Computer Science, University of North Carolina, Pembroke, USA

A – research concept and design; B – collection and/or assembly of data; C – data analysis and interpretation;
D – writing the article; E – critical revision of the article; F – final approval of the article

Address for correspondence
Bukola Christianah Adebayo-Tayo
E-mail: emailbukola.tayo@gmail.com

Abstract

Background. Phyto-reduction using *Senna alata* methanol leaf extract for nanoparticle (NP) biosynthesis is of great importance for the production of value-added nanomaterial with antimicrobial potential.

Objectives. The aim of this study was to investigate the biosynthesis of zinc oxide nanoparticles (ZnONPs) using crude methanol leaf extract of *S. alata* (SaZnONPs), antimicrobial efficacy of this extract, optimization of its production parameters, and its application in cold cream formulation.

Material and methods. Phytosynthesized SaZnONPs were characterized using UV-Vis absorption spectroscopy, Fourier-transform infrared spectroscopy (FTIR), scanning electron microscopy (SEM), thermogravimetric analysis (TGA), dynamic light scattering (DLS), X-ray diffraction (XRD) analysis, and energy-dispersive X-ray (EDX) spectroscopy. The antimicrobial activity of SaZnONPs and the formulated cold cream was evaluated.

Results. The SaZnONPs surface plasmon resonance (SPR) was 400 nm. Functional groups such as alkenes, alkynes and alkyl aryl ether were present. The SEM image showed NPs 7.10 nm in size and with a needle-like shape. The TGA values show the formations of stable ZnONPs, while the DLS showed the particle diameter average of 89.7 nm and 855.4 nm with 0.595 polydispersity index. The EDX analysis confirmed the formation of pure ZnONPs, and the crystallinity was confirmed with XRD analysis. Twenty-four hours of incubation and production at pH13 was optimal for NPs synthesis. The SaZnONPs and the formulated cold cream have antimicrobial properties against some pathogenic bacteria and *Pichia* sp. (16.00 mm) and *Trichophyton interdigitale* (11.00 mm).

Conclusions. *Senna alata* was able to serve as a stabilizing and capping agent for SaZnONPs biosynthesis. The SaZnONPs had good antimicrobial potential and can be used in cold cream formulation.

Key words: antibacterial, zinc oxide nanoparticles, *Senna alata*, cold cream formulation, *Pichia* species

Introduction

The problem of drug resistance has been a serious challenge to the wellbeing of the world population, which necessitates the search for new drugs with high antimicrobial potency to combat the existing resistant microorganisms. Nanotechnology has proven to be one of the most valuable means of synthesizing antimicrobial agents with a broad spectrum of activity. Noble metals such as silver, gold, zinc, copper, and iron are bio-converted by microbial and plant metabolites for nanoparticle (NP) synthesis; the NPs are widely used in drug delivery systems. Nanoparticle synthesis is an important field in nanotechnology as a result of material properties based on size.[1]

Zinc oxide nanoparticles (ZnONPs) have received considerable attention due to their unique antibacterial, antifungal and UV filtering properties, and high catalytic and photochemical activities, which are not observed at bulk phase.[2–4] Specifically, ZnONPs have a tremendous potential in biological applications like biological sensing, biological labelling, gene delivery, drug delivery, and nano-medicines due to their antibacterial, antifungal, anti-diabetic, anti-inflammatory, wound-healing, anti-oxidant, and optical properties.[5,6]

Zinc oxide nanoparticles can be synthesized using direct precipitation, homogeneous precipitation, solvothermal, sonochemical, reverse micelles, sol-gel, hydrothermal, thermal decomposition, and microwave irradiation methods.[7] Applerot et al. reported that ZnONPs exhibited stronger inhibitory activity against pathogenic microorganisms than chemically synthesized NPs.[8] The antibacterial potential of ZnONPs against some clinical pathogens has been reported.[9]

Green method of ZnONPs biosynthesis is gaining importance due to its simplicity, eco-friendliness, broad antimicrobial efficiency, and environmental control of chemical toxicity.[10,11] There is an increasing interest in the biosynthesis of metal NPs using plants as bio-reducing and capping agents based on their suitability for large scale production of NPs. Nanoparticles produced using plants are characterized by better stability and diversity in shape and size compared to the NPs produced using other organisms.[12]

Among the wide range of medicinal plants are members of the genus *Senna*. *Senna alata* is an ornamental shrub which is mostly used as antimicrobial agent.[13,14] The plant has been used for treating a wide variety of infections and diseases.[15,16] *Senna alata* has been reported to contain phytochemicals which are responsible for their biological actions against various pathogens. This has made it an important plant in various fields of relevance.[14,16]

Biosynthesis of ZnONPs using different plants such as *Aloe vera* extract, *Citrus aurantifolia* extract, *Plectranthus amboinicus*, orange juice, *Ocimum basilicum* L. var. *urpurascens*, and *Parthenium hysterophorus* L. has been reported.[17–21]

The antibacterial efficacy of the biosynthesized ZnONPs using ethanol extract of *Murraya koenigii* against some bacteria has been reported.[22] This research aimed at examining the phytosynthesis of ZnONPs using crude methanol leaf extract of *S. alata*, as well as at optimization of production parameters, antimicrobial efficacy and application of the ZnONPs in cold cream formulation.

Material and methods

Plant collection and extraction

Fresh leaves of *S. alata* were collected from the premises of the University of Ibadan, Nigeria. The leaves were cleaned with running tap water and rinsed with distilled water to remove debris and contaminants. The leaves were air-dried at room temperature, chopped into small pieces, milled, poured into a macerating jar, and methanol was added and filled to the brim. The solvent was then stirred with the solute using a sterilized glass rod and this was repeated every 8 h during a cycle which lasted for 72 h. After 72 h of extraction, the extract was decanted and filtered using a Whatman's filter paper (No. 1), and then concentrated using a rotary evaporator under reduced pressure and low temperature.

Collection of test cultures

Typed strains (*Pseudomonas aerogenosa* (ATCC 27853), *Staphylococcus aureus* (ATCC 29213), *Bacillus* sp., *Escherichia coli* (ATCC 11775), and *E. coli* (ATCC 35218)) and clinical strains (5 strains of Multi Drug Resistant Staphylococci (MRS) and fungi (*Candida albicans*, *Candida krusei*, *Candida tropicalis*, *Trichophyton* sp., *Aspergillus niger*, and *Penicillium* sp.)) were obtained from the Department of Microbiology of the University of Ibadan.

Photosynthesis of zinc oxide nanoparticles

The ZnONPs was biosynthesized using methanol leaf extract of *S. alata*. The plant extract was added to 10 mM zinc acetate solution in ratio of 1:50. The mixture was incubated for 24 h to facilitate the formation of NPs. Aqueous leaf extract and zinc acetate solution were used as controls throughout the experiments. Change in the color of the solution indicated the presence of ZnONPs. The NPs were dried at 60°C to obtain a pale white powder.

Characterization of nanoparticles

Visual observation and UV-Vis spectra analysis

The gradual color change of the mixture in the test bottle was visually observed and noted. The formation and stability of the NPs was monitored by measuring the absorbance using UV–Vis spectrophotometry (UV–Vis spectrophotometer; Ocean Optics, Winter Park, USA). The optical property

of the NPs was determined using ultraviolet and visible absorption spectroscopy in the range of 200–800 nm at a resolution of 1 nm. The UV-Vis spectra were recorded at 24–72 h.

Fourier-transform infrared spectroscopy analysis

The functional group and composition of the ZnOPS synthesized using crude methanol leaf extract of *S. alata* (SaZnONPs) was determined using Fourier-transform infrared spectroscopy (FTIR) spectroscopy (Shimadzu, Kyoto, Japan). Two milligrams of the SaZnONPs was ground with KBr salt at 25°C and pressed into a mold to form a pellet. The spectra were recorded at a wave range of 500–4000 cm^{-1} and at a resolution of 4 cm^{-1}.

Scanning electron microscopy analysis

The size and shape of the SaZnONPs were determined using scanning electron microscopy (SEM). Thin films of dried SaZnONPs were gold-coated using a coater (Model No. JFC-1600; JEOL, Akishima, Japan). The images of SaZnONPs were obtained in a SEM (Zeiss EVO-MA 10; Carl Zeiss AG, Oberkochen, Germany). Details regarding applied voltage, magnification and size of the contents of the images were also implanted on the images.

Thermogravimetric analysis

Thermogravimetric analysis (TGA) was done on the dried SaZnONPs in SDT 2960 device (TA Instruments, New Castle, USA). The samples were heated in open alumina pans from 40°C to 600°C, under an oxidant atmosphere (O$_2$), flux of 50 mL/min and a heating rate of 10°C/min. The estimation of the zinc content in SaZnONPs was done using the residue at 600°C.

Dynamic light scattering

Particle size distribution and average size of SaZnONPs was determined using PSI Online Diameter-Measuring Particle Size Analyzer (DFMC, Dandong, China). Liquid sample before centrifugation was diluted 10 times using deionized water and transferred to cuvette, and analysis was performed using dynamic light scattering (DLS) (Malvern Zetasizer Nano Z500; Malvern Panalytical, Malvern, UK). The sample holder temperature was maintained at 25°C.

Energy-dispersive X-ray spectroscopy

The elemental analysis of SaZnONPs was determined using an energy-dispersive X-ray (EDX) spectroscopy. The dried SaZnONPs powder was used for the analysis and pure ZnO was used as standard. The EDX analysis software from Oxford Instruments (Abingdon, UK) was used. All measurements were performed at an accelerated voltage of 10 kV.

X-ray diffraction analysis of SaZnNPs

The purity and crystalline structure of the SaZnONPs was determined using X-ray diffraction (XRD) analysis. X-ray diffraction patterns were obtained in a Siemens Kristalloflex diffractometer (Siemens AG, Munich, Germany) using nickel-filtered Cu-Kα radiation from 4° to 70° (2θ angle).

Determination of antimicrobial potential of the SaZnONPs

The antibacterial and antifungal potential of the SaZnONPs was determined using agar well diffusion method.[23] The isolates were cultured overnight in peptone water and 18 hour-old culture of the isolate was seeded on Mueller–Hinton agar (Lab M Ltd., Heywood, UK) plates. Uniform wells of 7 mm were cut on the dried agar plate and the wells were filled with 20 μL of the SaZnONPs. Zinc acetate solution, methanol extract of *S. alata* leaves, dimethyl sulfoxide (DMSO), streptomycin, and fungusol (miconazole nitrate BP 2%; Afrab Chem Ltd, Lagos, Nigeria) were used as controls. The inoculated plates were incubated at 37°C for 24 h for bacteria and at 28°C for 72 h for fungi. Diameters of clear zones of inhibition (ZOI) around the wells were measured in millimeters. Diameters greater than 1 mm were considered positive after subtracting the original diameter of the cork borer (7 mm) from the final reading.

Minimum inhibitory concentration determination of the SaZnONPs

To determine the minimum inhibitory concentration (MIC) of the SaZnONPs, wells were bored on inoculated agar plates. The wells were filled with 20 μL of different concentration (10–100%) of the SaZnONPs. The plates were incubated appropriately at 37°C for 24 h for bacteria and at 28°C for 72 h for fungi. The zones of inhibition were then observed and recorded. The lowest concentration of the SaZnONPs that completely inhibited the growth of the test microorganism was taken as the MIC of the NPs.

Optimization of production conditions for SaZnONPs phytosynthesis

The production parameters such as incubation time (2–72 h), different concentration of zinc acetate (1–20 mM) and the leaves extract (0.2–0.8 mL), incubation temperature (28–45°C) and pH (4–13) for NP biosynthesis was optimized. UV-visible spectra of and the FTIR of the biosynthesized SaZnONPs were evaluated.

Formulation of SaZnONPs cold cream

The cold cream formulation was done by first preparing the oil phase and aqueous phase. To prepare the base, the oil phase was prepared by adding beeswax (10 g) to

liquid paraffin (30 g) and the mixture was placed in a water bath (90°C). For the aqueous phase preparation, borax (0.5 g) was dissolved in distilled water (9.5 mL) and heated up to 50°C. The SaZnONPs was dissolved in the aqueous phase to form a mixture. The cold cream SaZnONPs was formulated by slowly adding the oil phase to the aqueous phase with continuous stirring until it become semisolid. The control cold cream was formulated without the addition of SaZnONPs. The formulated samples were kept for further analysis.

Determination of pH and the viscosity of the of the formulated cream

The pH of the formulated cold creams was measured using direct immersion of the electrode of pH meter into formulated creams. The viscosity of the formulated cold cream samples at different shear rates was done using a Brookfield viscometer DV-II+ pro (Brookfield Engineering Laboratories, Middleboro, USA) with spindle No. S−64 at 20 rpm at 25°C, and the analysis was done in duplicate.

Determination of the antimicrobial activity of the cold cream

The antimicrobial potential of the formulated cold cream samples was evaluated using agar well diffusion method. The test pathogens were spread on Mueller agar using sterile cotton swabs. Wells were bored in the inoculated agar plates and the formulated cream samples were introduced into the wells. Formulated cream samples without the NPs, zinc acetate solution, streptomycin, and fungusol were used as controls. The plates were incubated and the diameters of clear zones of inhibition (ZOI) around the wells were recorded in millimeters.

Results and discussion

The visual observation of the ZnONPs synthesized using the crude methanol extract of *S. alata* after 24 h incubation is shown in Fig. 1A−C. The mixture turned pale brown after 24 h of incubation, indicating the formation of SaZnONPs.

The UV-Vis absorption spectrum of SaZnONPs is shown in Fig. 2. The absorption spectrum was recorded for the NPs in the range of 200–800 nm. The surface plasmon resonance (SPR) peak was observed at 400 nm after 24 h.

The absorption spectrum of SaZnONPs 400 nm may be ascribed to the nanometric size effect of the synthesized ZnO, which is characteristic of hexagonal ZnONPs.[24] The SPR peak of 370 nm has been reported by different researchers.[21,25,26] This absorption peak shows evidently the monodispersion of the SaZnONPs formed. The sharp and prominent absorption band may arise due to the transitions from a valence band to conduction band.
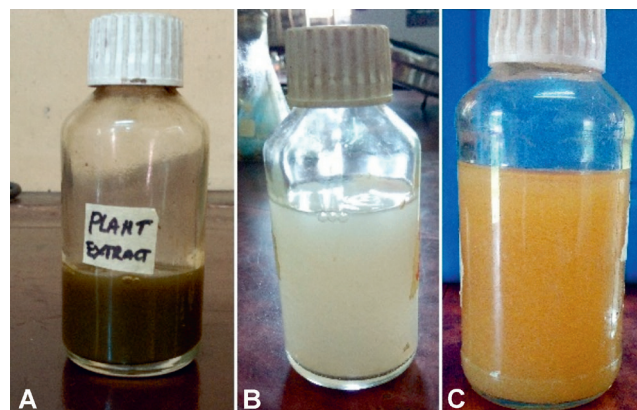
Fig. 1. Visual observation of photosynthesized SaZnONPs. A. *Senna alata* crude methanol leaf extract. B. Zinc acetate. C. Biosynthesized ZnONPs
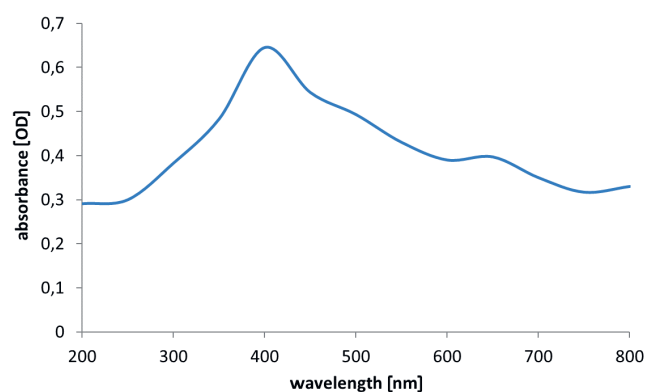
Fig. 2. UV-Vis spectra of photosynthesized SaZnONPs

The spectra of the biosynthesized SaZnONPs characterized using FTIR are shown in Fig. 3. Twelve peaks were observed – from 3,852.04 cm⁻¹ to 464.73 cm⁻¹. The FTIR spectrum showed a broad peak at 3,444.43 cm⁻¹, which corresponds to the stretching vibrations of hydroxyl OH band. The peak at 2,075.73 cm⁻¹ indicates an alkyne C≡C bending vibration. The peaks at 1,643.73 cm⁻¹ and 1,633.71 cm⁻¹ showed the stretching vibrations of cyclic and conjugated alkenes (C=C) group. Furthermore, the peaks at 3,852.04 cm⁻¹ and 1,416.09 cm⁻¹ indicate the presence of alcohol (O−H) group. The peak at 1,650.78 cm⁻¹ indicates the presence of phosphine (X=C=Y) groups. The band at 1,011.78 cm⁻¹ corresponds to the bending vibration of the alkyl aryl ether (C−O), while the peak at 569.06 cm⁻¹ shows the presence of an alkyl halides (C−X) group. Finally, the band at 464.73 cm⁻¹, 651.76 cm⁻¹ and 716.56 cm⁻¹ corresponds to the stretching of Zn-O compound.

The FTIR results show the possible plant biomolecules involved in the NP biosynthesis and as functioning capping agents. It also shows that the biosynthesized SaZnONPs were surrounded by proteins and other metabolites.[27] Based on the FTIR spectra, it can be stated that the presence of these functional groups suggests that the biological molecules play an important role in the biosynthesis of NPs, and could possibly perform dual functions of formation and stabilization of SaZnONPs in an aqueous medium.
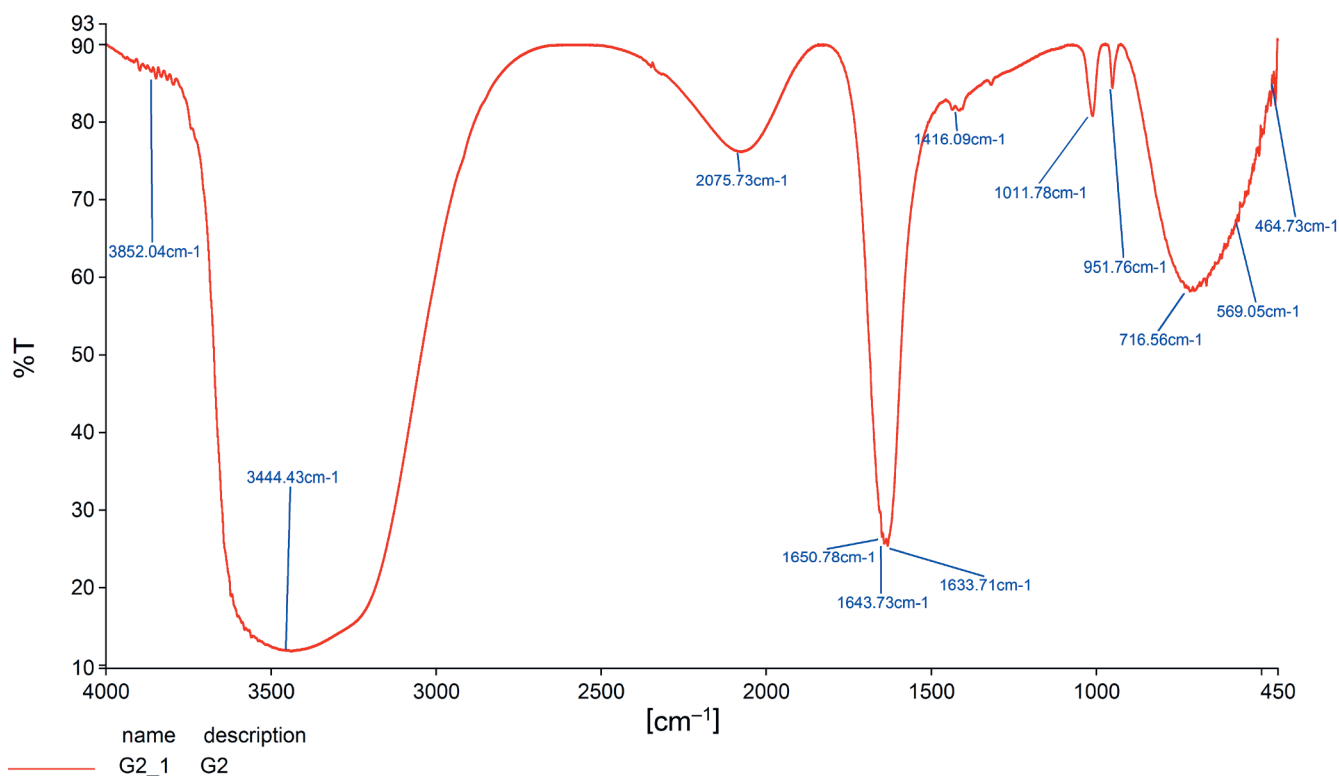
Fig. 3. FTIR spectra of SaZnONPs

The SEM image of SaZnONPs is presented in Fig. 4. It shows needle-like shape NPs with 10.3 nm in diameter.
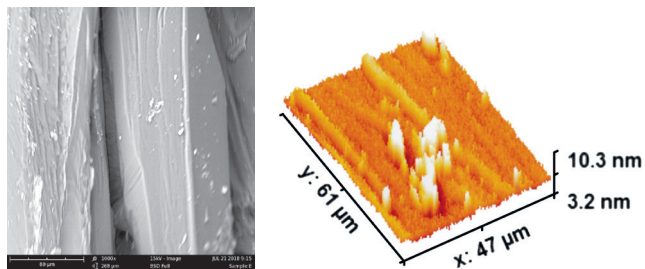
Fig. 4. SEM image of SaZnONPs

The SEM images of the crystals showed some non-uniform distribution in the form of a needle-like structure without agglomeration. The boundaries between single crystallites were visible. Agglomerates were composed of several individual nano-sized crystals.

The TGA of SaZnONPs is showed in Fig. 5. The TGA profile showed a continuous weight loss with 2 quasi-sharp changes occurring at 234.02°C and 473.75°C, followed by a nearly constant plateau. The annealing above 473.75°C seems to guarantee the formation of stable SaZnONPs. After heating to 234.02°C, the excess water seems to be driven off and the material initiates organic carbon decomposition. The material continues to decompose. Oxidation of the catalyst particles is seen after 473.75°C, leading to dramatic mass changes with a residual mass of 4.95% at 846.87°C.

The TGA showed a two-stage weight loss, which indicates the decomposition and vaporization of various functional groups at different temperatures. The large weight loss may be attributed to the breakdown of the organic carbon coordinated with ZnONPs in extract-zinc acetate hybrid. Oxidation of the catalyst particles is seen after 473.75°C, leading to dramatic mass changes with a residual mass of 4.95% at 846.87°C. This report differs from the observation of Ramesh et al.,[27] who observed thermal dehydration at 165°C and 318°C respectively, with an endothermic peak at 390°C during the decomposition of zinc nitrate to ZnO.
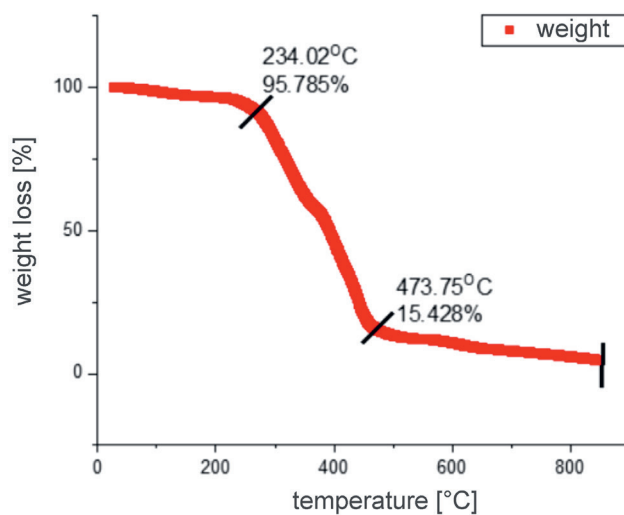
Fig. 5. The results of TGA of SaZnONPs

The TGA shows the interaction between the NPs and the stabilizer. Singh et al.[28] reported that the TGA of NPs and of capping agents not only provides information about the stability of NPs, but can also evaluate the yield of NPs in the final product.

Figure 6 shows the average particle size, size distribution, and polydispersity index (PDI) of SaZnONPs using DLS measurement. It shows average particle sizes of 412.0 nm and 155.2 nm with a polydispersity index of 0.481.

The hydrodynamic diameter, which uses the diffusion coefficient of the SaZnONPs colloids and the autocorrelation function measured with DLS techniques, showed the size and distribution of the NPs. The large average diameter of 549.2 nm can be attributed to the aggregation of the NPs over time. This is in line with the work of Chitsazi et al., who observed that there was an increase in the average diameter of synthesized NPs with an increase in reaction time.[29]

The EDX spectrum of the biosynthesized SaZnONPs is shown in Fig. 7. The spectrum of the optimized sample confirmed the presence of zinc and oxygen in the powder. Consequentially, there are no other elements except zinc, thereby sustaining the pure chemical form of the formed ZnONPs.
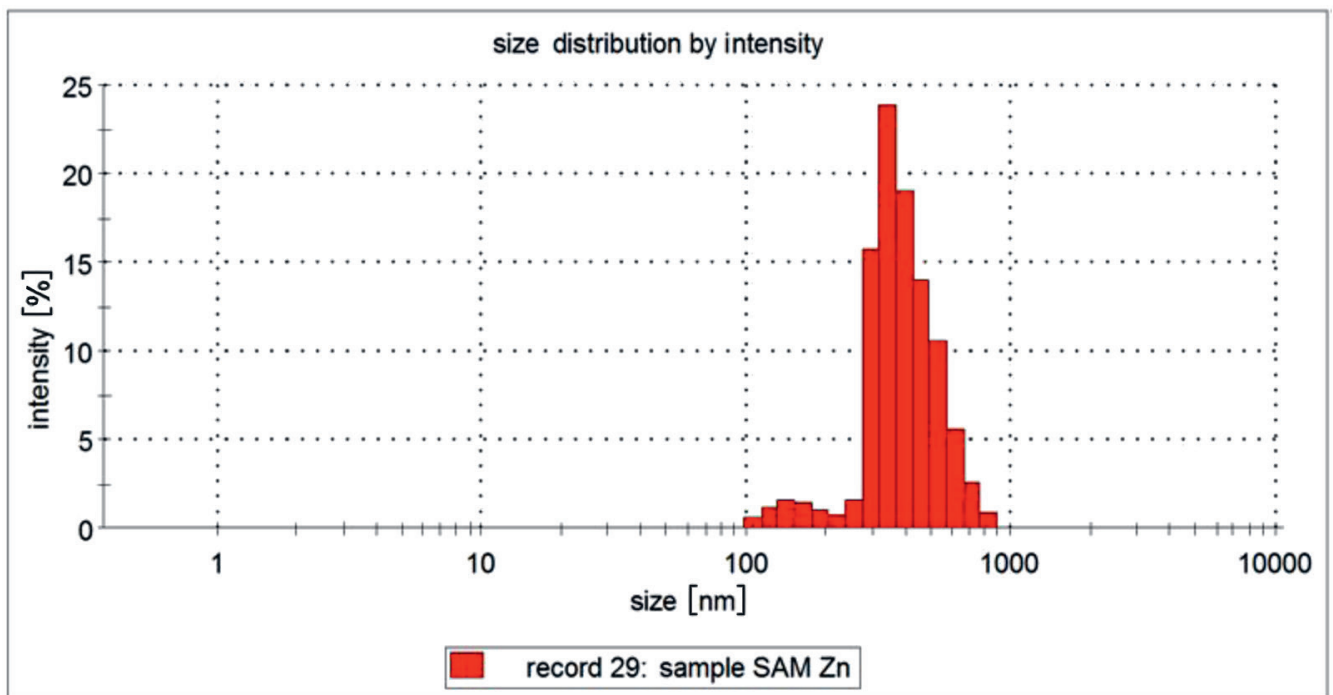
Fig. 6. DLS showing the particle size distribution of SaZnONPs
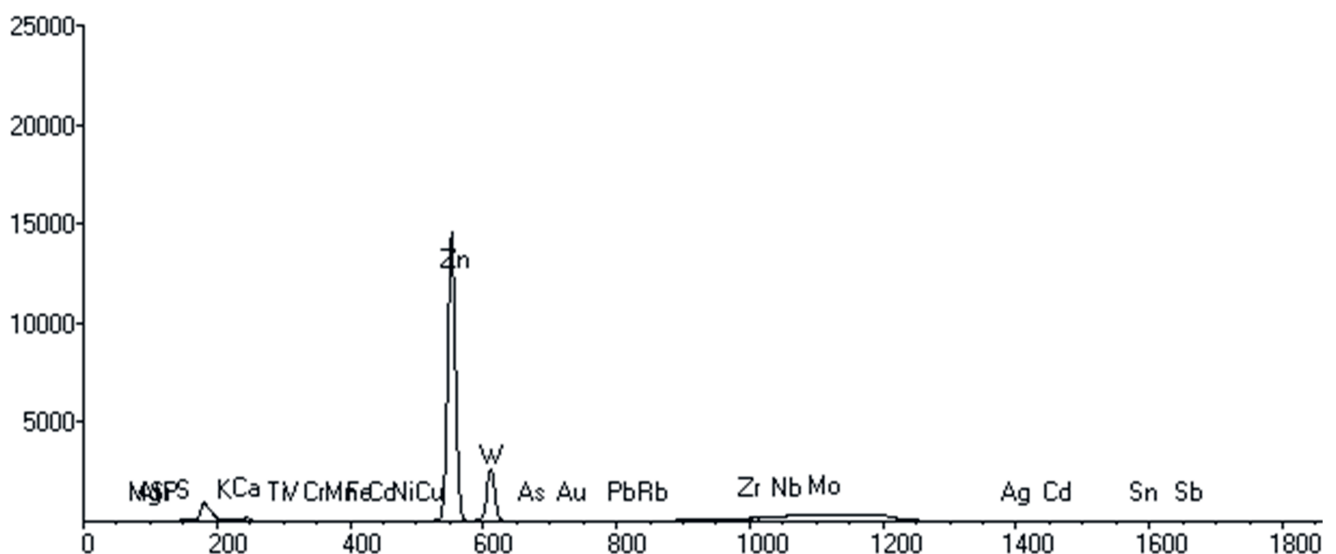
Fig. 7. EDX spectra of SaZnONPs

Figure 8 shows the results of XRD analysis of the SaZnONPs. It was observed that the 7 reflection peaks of 2θ degree with corresponding Miller indices (hkl) showed values at 15.32° (002), 37.39° (110), 40.58° (002), 42.15° (101), 43.09° (101), 44.18° (002), and 46.99 (101), which are matched with the Crystallography Open Database (COD; http://www.crystallography.net/cod) in MATCH! Phase Identification (https://www.crystalimpact.com/match) from Powder Diffraction software.

The EDX spectrum of SaZnONPs sample confirmed the presence of zinc in the powder. The EDX clearly showed the purity of biosynthesized metal NPs and of the SaZnONPs.[30]

The antifungal potential and MIC of the SaZnONPs against pathogenic fungi is shown in Table 1. The SaZnONPs presented activity only against *Pichia* sp. and *T. interdigitale* with a zone of 16 mm and 11 mm, respectively, while the remaining fungi strain were resistant. The activity of the SaZnONPs against *Pichia* sp. and *T. interdigitale* was up to 10%, showing that the 2 organisms are highly susceptible to SaZnONPs.
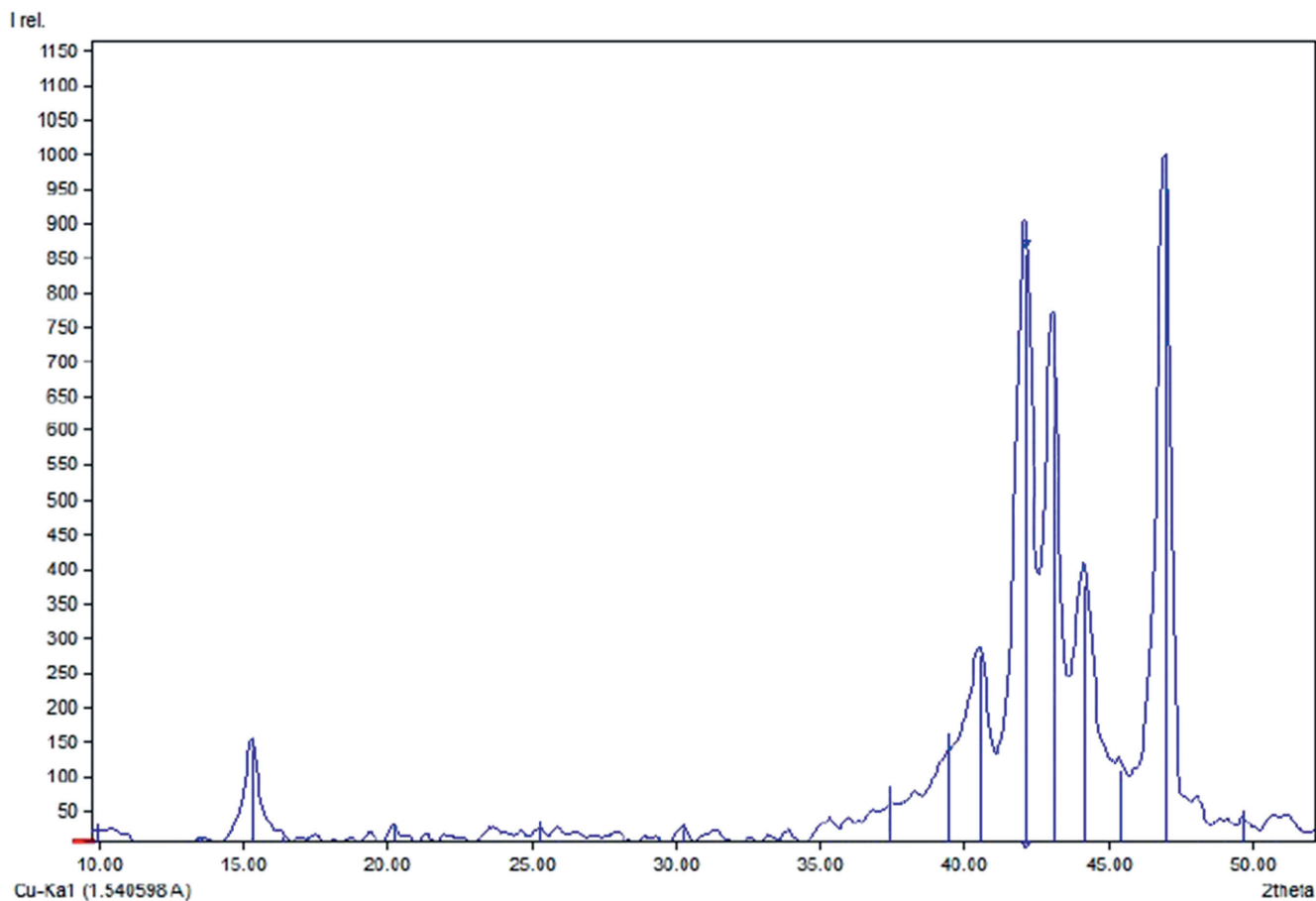
Fig. 8. XRD pattern of SaZnONPs

Table 1. Antifungal activity and MIC of SaZnONPs against some pathogenic fungi

| Test bacteria | Antibacterial activity [mm] | | | MIC for SaZnONPs [%] | | | | | |
| | | | | zone of inhibition [mm] | | | | | |
	SaZnONPs	zinc acetate solution	fungusol	100	90	70	50	30	10
C. albicans A	–	–	2	–	–	–	–	–	–
C. albicans B	–	–	6	–	–	–	–	–	–
C. albicans C	–	–	8	–	–	–	–	–	–
Rhizopus sp.	–	–	4	–	–	–	–	–	–
Pichia sp.	16	6	8	16	16	14	12	10	8
C. tropicalis	–	–	4	–	–	–	–	–	–
C. krusei	–	–	2	–	–	–	–	–	–
T. interdigitale	11	4	6	11	15	14	12	8	8

SaZnONPs – zinc oxide nanoparticles biosynthesized using crude methanol leaf extract of *Senna alata*; MIC – minimum inhibitory concentration.

The antibacterial activity and MIC of the SaZnONPs against pathogenic bacteria is shown in Table 2. The SaZnONPs presented activity against *S. aureus* D *E. coli* 35218, *S. saprophyticus* B and *S. epidermidis* C with zone of inhibition of 9 mm, 5 mm and 2 mm, respectively. The SaZnONPs had a low activity (1.00 mm) against *S. aureus* D at 10% concentration, while there was no activity recorded against it for *S. saprophyticus* B and *S. epidermidis* C beyond the full 100% concentration of the SaZnONPs.

The SaZnONPs showed activity against only 2 of the fungi species. Rajiv et al. observed that plant pathogenic fungi were susceptible to ZnONPs.[21] The susceptibility of tested fungi pathogens can be attributed to the nature of the particles, i.e., their nanoscale structure.[31] The SaZnONPs showed activity against different species of *Staphylococcus* and against *E. coli* 3521. Gunalan et al.[10] observed that ZnONPs were active against *S. aureus*, while Ambika and Sundrarajan[24] recorded antibacterial activity against *S. aureus* and *E. coli*. Gunalan et al. revealed that the nanosize of NPs enables the permeability of bacteria cell membrane and gives access to the organelles of the cell.[10]

The MIC of the NPs against both the fungi and bacteria pathogens showed a continuous decrease in activity along with the reduction in the concentration of the NPs used. This showed that the activity of the NPs depends on its concentration. This is in accordance with the report of Dubey et al.[32] and Oboh and Abulu[33] who stated that antimicrobial activity is a function of the concentration of the active ingredient that is in contact with the organism.

Optimization of conditions of different production parameters on the biosynthesis of ZnONPs was investigated. Figure 9A shows the UV-Vis spectra during op-timization of incubation time (2–72 h) on the biosynthesis of SaZnONPs. The optimum incubation time for the biosynthesis was recorded at 24 h. The SPR shows a high sharp peak after 24 h of synthesis at a wavelength of 400 nm.

Figure 9B shows the UV-Vis spectra during optimization of SaZnONPs biosynthesis at different molar concentration of zinc acetate; 10 mM supported the optimum SaZnONPs biosynthesis. The SPR showed a sharp peak at 400 nm for 10 mM zinc acetate molar concentration. Broad peaks were observed for other concentrations at 500 nm.

Figure 10A shows the UV-Vis spectra during optimization of different incubation temperature (4–45°C) for the biosynthesis of SaZnONPs. The temperature of 4°C supported optimum SaZnONPs production and the SPR was recorded at 600 nm.

Figure 10B shows the UV-Vis spectra for optimization of SaZnONPs biosynthesized using different volume of the extract (0.2–0.8 mL). 0.8 mL of the extract supported optimum SaZnONPs biosynthesis. The SPR showed peaks was at 450 nm.

Figure 11 shows the UV-Vis spectra for optimization of pH (4–13) for biosynthesis of SaZnONPs. pH 13 supported optimum biosynthesis with SRP at 450 nm.

It is well known that the morphology and size of metal NPs produced from a metallic precursor in a solution depend on various reaction conditions, such as the concentration of metal ion, ratio of metallic salt/reducing agent, time, temperature, and pH.[34] The optimization of conditions for SaZnONPs synthesis in this study indicated the effect of the different parameters – time, temperature,

Table 2. Antibacterial activity and MIC of SaZnONPs against some pathogenic bacteria

Test bacteria	Antibacterial activity [mm]			MIC for SaZnONPs [%]					
				Zone of inhibition [mm]					
	SaZnONPs	zinc acetate solution	streptomycin	100	90	70	50	30	10
S. aureus A	–	–	8.00	–	–	–	–	–	–
S. aureus B	–	–	9.50	–	–	–	–	–	–
S. aureus C	–	–	12.50	–	–	–	–	–	–
S. aureus D	9	–	12.00	9	10	8	8	5	1
S. aureus 29213	–	–	7.00	–	–	–	–	–	–
E. coli 35218	5	4	7.00	5	–	–	–	–	–
E. coli 11775	–	–	6.50	–	–	–	–	–	–
P. aeruginosa 27853	–	–	7.00	–	–	–	–	–	–
C. freundii	–	–	8.00	–	–	–	–	–	–
S. typhi 14028	–	–	7.00	–	–	–	–	–	–
B. cereus	–	–	7.50	–	–	–	–	–	–
S. saprophyticus A	–	–	8.50	–	–	–	–	–	–
S. saprophyticus B	2	–	8.00	2	–	–	–	–	–
S. epidermidis A	–	–	8.00	–	–	–	–	–	–
S. epidermidis B	–	–	8.00	–	–	–	–	–	–
S. epidermidis C	2	2	6.50	2	–	–	–	–	–
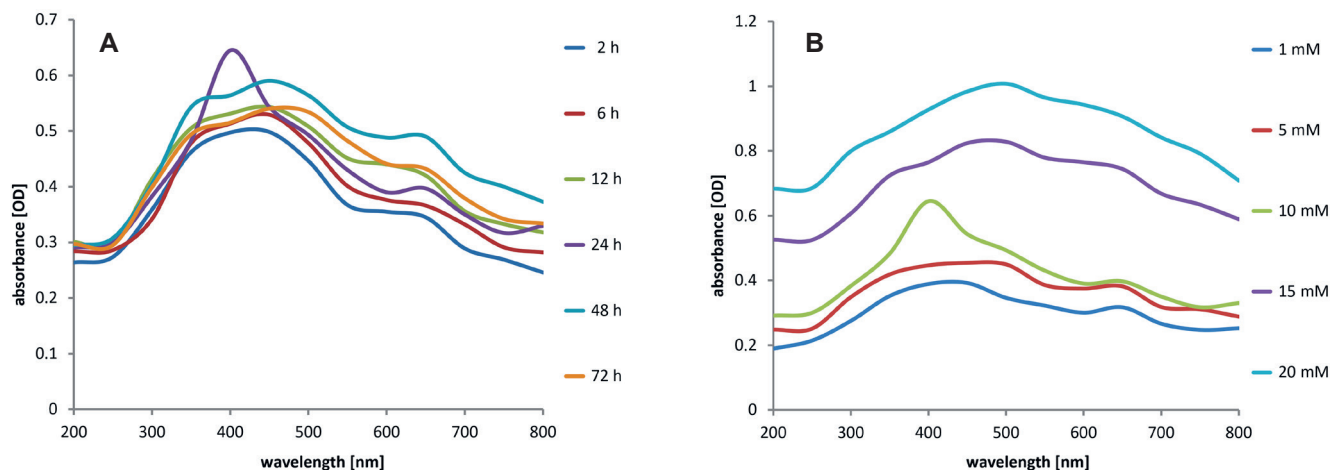
Fig. 9. UV-Vis spectra of the SaZnONPs biosynthesized at different (A) incubation time and (B) molar concentrations of zinc acetate
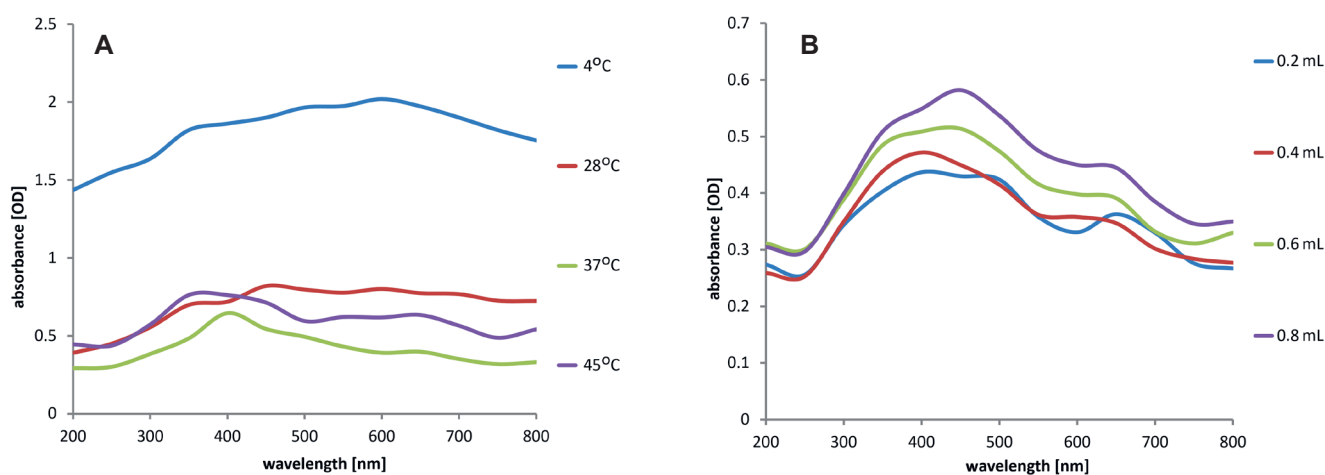
Fig. 10. UV-Vis spectra of the SaZnONPs biosynthesized at (A) different incubation temperature and (B) different concentration of the extract
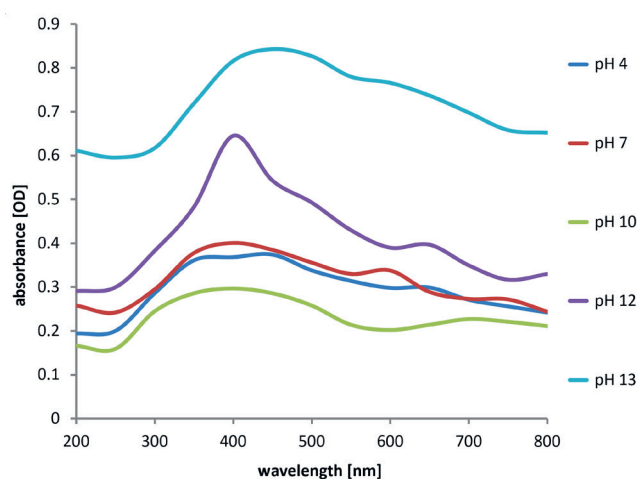
Fig. 11. UV-Vis spectra of the SaZnONPs biosynthesized at different pH

concentrations of zinc salt and extract, and pH on the NPs phytosynthesis. The effect of time is a significant factor that affects production of SaZnONPs. The SPR was recorded after 24 h which is a period considered being enough for the maximal production of SaZnONPs. This finding was in contrast with the report of Raliya and Tarafdar,[29] where it was observed that the biosynthesis of ZnONPs was optimal after 72 h of incubation. The incubation temperature of 4°C showed the highest plasmon peak of the biosynthesis of SaZnONPs while the SPR was observed using 10 mM of zinc acetate. Different volume of *S. alata* leaf extracts were used for the synthesis of SaZnONPs, and 0.8 mL of the extract was most suitable. These results also indicate that basic pH had the highest peak during SaZnONPs biosynthesis. A sharp peak was recorded at pH 12. pH affects the amount of NPs production and their stability, which is a critical factor in the control of the size and morphology of NPs.[35]

Figures 12–15 show shows the FTIR spectra of the different optimized conditions for the biosynthesis of SaZnONPs. Five troughs corresponding to the hydroxyl O–H stretching bonds, alkynes and amides were prominent in all the spectra.

The FTIR spectra under different optimization conditions showed that the peaks around 3,400 cm^{-1} and 1,600 cm^{-1}, which corresponds to the O–H stretch and C=C stretch, were constant under all conditions. This shows that under different optimization conditions, there are large amounts of compounds that can actively chelate
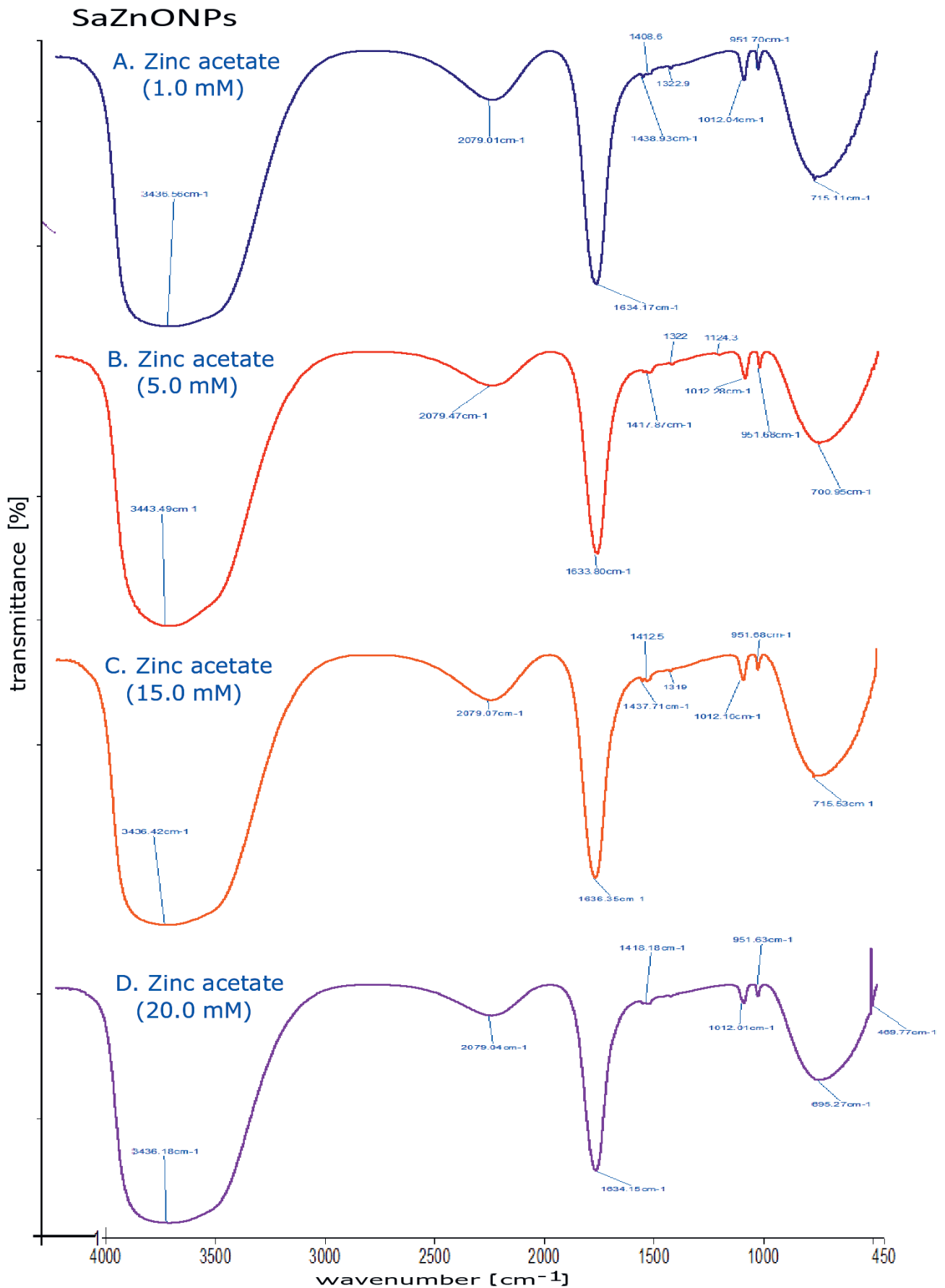
Fig. 12. FTIR spectra of SaZnONPs biosynthesized under optimized concentration of zinc acetate: A) 0.1 mM zinc acetate; B) 5.0 mM zinc acetate; C) 15.0 mM zinc acetate; and D) 20.0 mM zinc acetate

and reduce the NPs, which is confirmed in the finger-print regions of the latter end of the spectrum. The effect of different parameters could have inhibited the activity of some of the components of the plant extract, as seen in the absence of some functional groups under different conditions. The biological entities act as capping and sta-bilizing agents in the synthesis process. Good examples are the phytochemicals like flavonoids, phenolics, terpe-noids, and cofactors, which act mainly as reducing and stabilizing agents during synthesis.
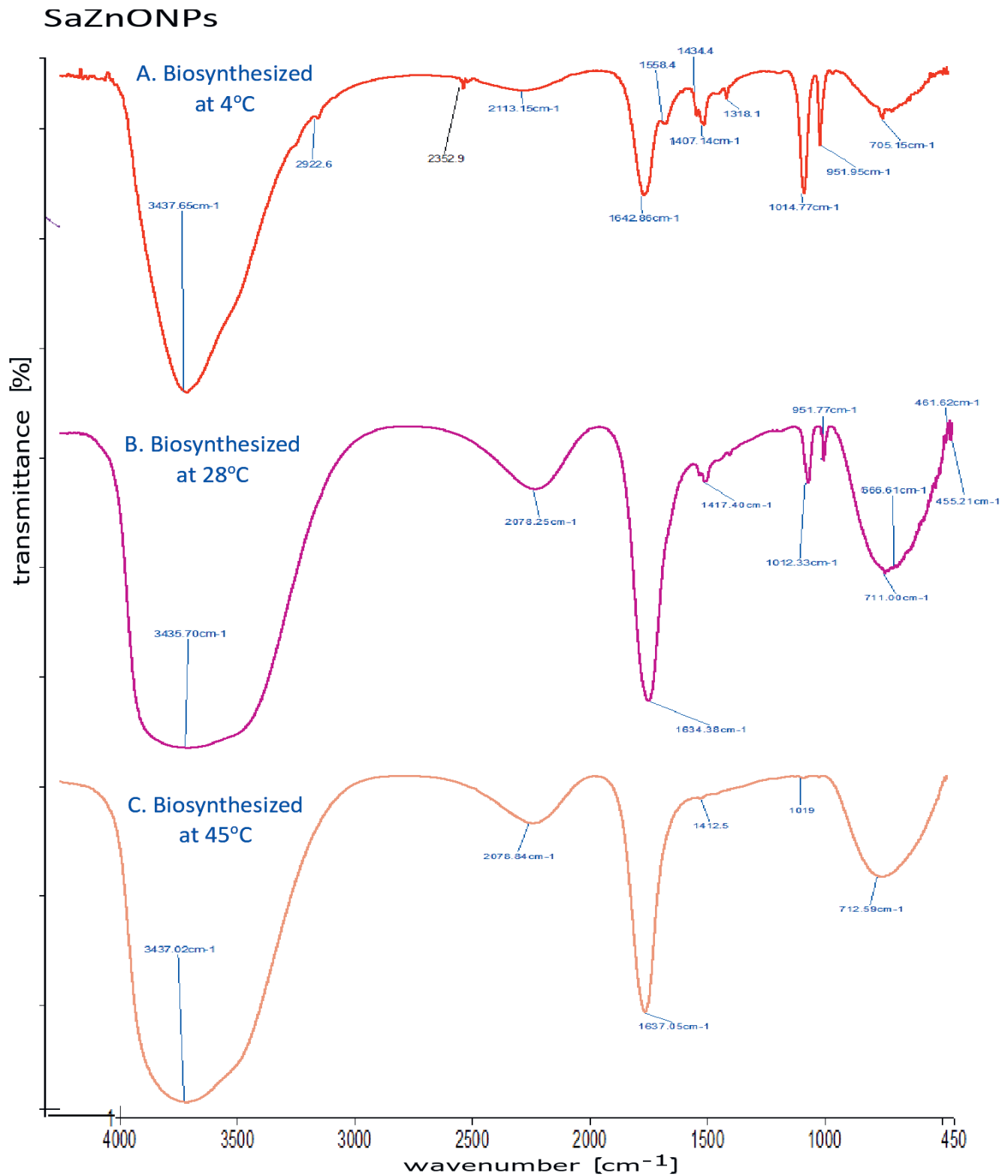
Fig. 13. FTIR spectra of SaZnONPs biosynthesized under optimized temperature: A) 4°C; B) 28°C; and C) 45°C

SaZnONPs

Fig. 14. FTIR spectra of SaZnONPs biosynthesized under optimized extract to zinc acetate ratio: A) 1:100; B) 3:100; and C) 4:100

SaZnONPs

Fig. 15. FTIR spectra of SaZnONPs biosynthesized under optimized pH: A) pH 4; B) pH 7; C) pH 10; and D) pH 13

Table 3 shows the viscosity and pH measurement of the cold cream incorporated with 1% SaZnONPs (C1) and cold cream combined with 2% SaZnONPs (C2). The viscosity was reported in a unit of centipoises (cps) and torque. The apparent viscosity and torque were shown in relation to the revolutions per minute (rpm or shear stress) for the formulations. T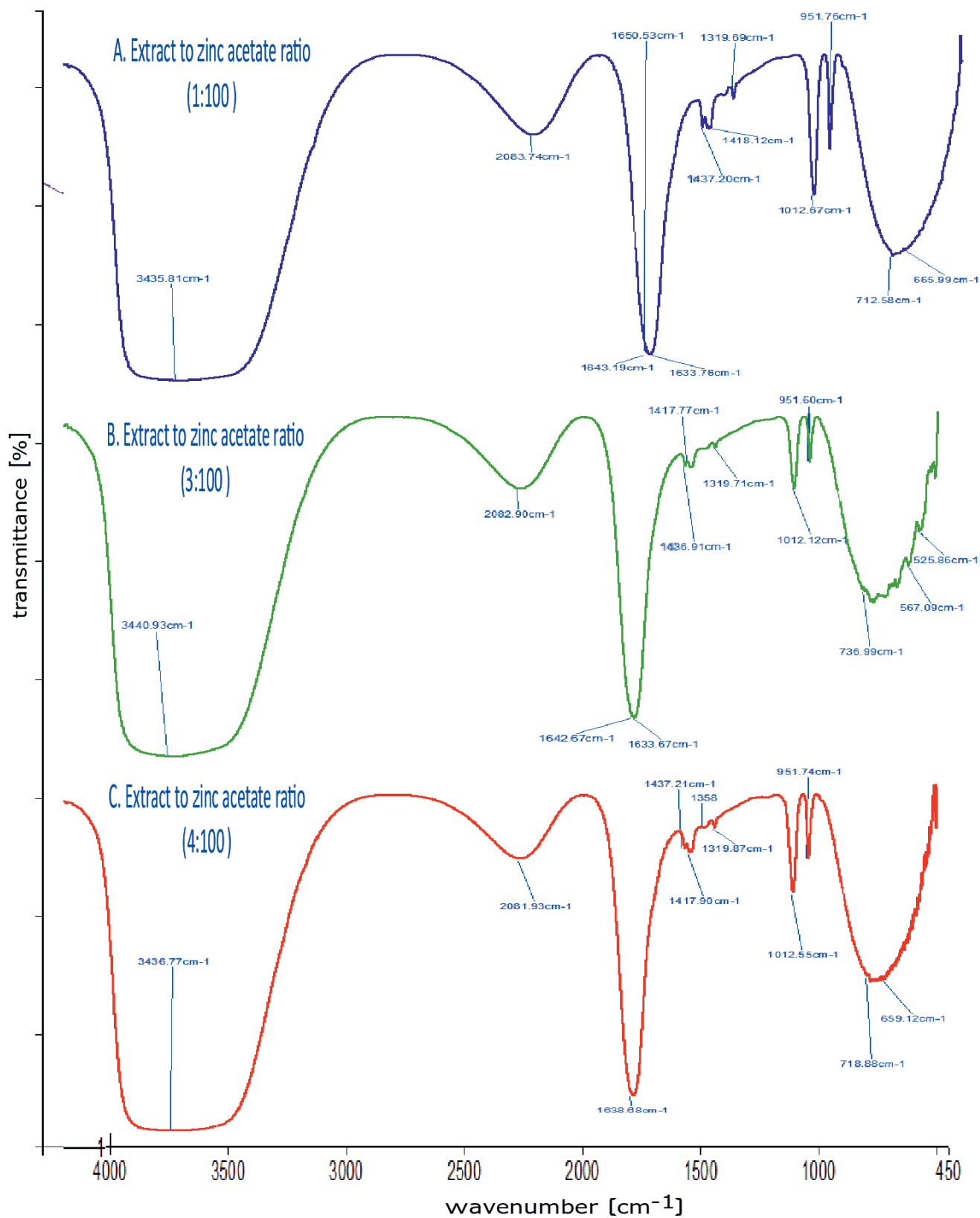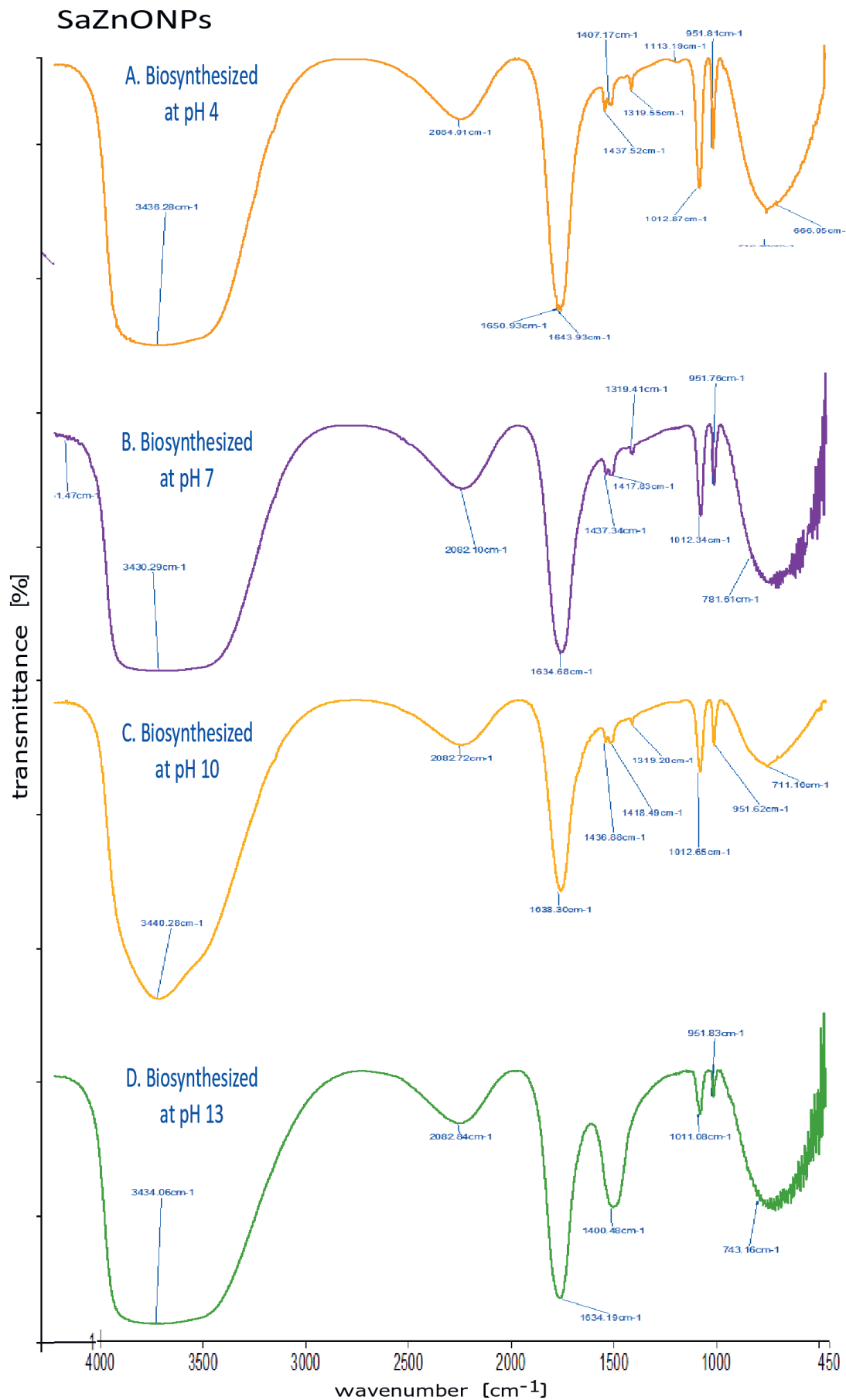he viscosity for the C1 and C2 formulated cold cream samples were 14,400 cps and 12,240 cps at 50 rpm and 8,080 cps and 6,920 cps at 100 rpm, respectively.

The pH of the cream base was 5.64, while the pH of the C1 and C2 samples were 8.16 and 7.56. There was an increase in pH when 1% and 2% SaZnONPs was incorporated into the cream base.

Table 4 shows the antibacterial and antifungal activity of cold cream incorporated with SaZnONPs against the test pathogen. Only 1 strain of *S. aureus* was susceptible to the formulated cream with a 3.0 mm zone of inhibition. The cream showed activity against 25% (2) of the fungal pathogens – *Pichia* sp. (2.0 mm) and *T. interdigitale* (5.0 mm).

The pH of the human skin typically ranges from 4.5 to 6.0, and 5.5 is considered to be the average pH of the skin.[36] Therefore, the formulations intended for application to the skin should have pH close to this range. In this study, all the cream formulations were close to the pH of the skin. The cream formulations also showed proper viscosity, which is needed for good cream-based formulations.

Conclusions

Senna alata methanol leaf extract was a good bioreducing, stabilizing and capping agent for zinc acetate in the phytosynthesis of SaZnONPs. The biosynthesized NPs exhibited good antibacterial and antifungal activity against some of the test pathogens. The SaZnONPs formulated cream has good viscosity and pH and appreciable antimicrobial efficiency against a few of the test bacteria and fungi.

ORCID iDs

Bukola Christianah Adebayo-Tayo 🔵
    https://orcid.org/0000-0003-2404-1686
Samuel O Borode 🔵 https://orcid.org/0000-0003-4929-4786
Olusola Ademola Olaniyi 🔵 https://orcid.org/0000-0002-5811-2270

Table 3. Viscosity and pH values of the different cream formulations

Sample code	Viscosity				pH
	50 RPM		100 RPM		
	centipoise	torque	centipoise	torque	
C1	14,400	18.05	8,080	20.2	8.16
C2	12,240	15.3	6,920	17.3	7.56
C3	–	–	7,560	–	6.92
Cream base	–	–	3,160	–	5.64

C1 – cold cream incorporated with 1% SaZnONPs;
C2 – cold cream incorporated with 2% SaZnONPs;
C3 – cold cream incorporated with 2% zinc acetate.

Table 4. Antibacterial and antifungal activity of SaAgNPs-incorporated cold cream formulation

S/N	Test bacteria	Antibacterial activity of SaZnONPs cold cream [mm]	S/N	Test fungi	Antifungal activity of SaZnONPs cold cream [mm]
1	*S. aureus* A	3.0	1	*C. albicans* A	–
2	*S. aureus* B	–	2	*C. albicans* B	–
3	*S. aureus* C	–	3	*C. albicans* C	–
4	*S. aureus* D	–	4	*Rhizopus* sp.	–
5	*S. aureus* 29213	–	5	*Pichia* sp.	2.0
6	*E. coli* 35218	–	6	*C. tropicalis*	–
7	*E. coli* 11775	–	7	*C. krusei*	–
8	*P. aeruginosa* 27853	–	8	*T. interdigitale*	5.0
9	*C. freundii*	–			
10	*S. typhi* 14028	–			
11	*B. cereus*	–			
12	*S. saprophyticus* A	–			
13	*S. saprophyticus* B	–			
14	*S. epidermidis* A	–			
15	*S. epidermidis* B	–			
16	*S. epidermidis* C	–			
17	*S. typhi* 14028	–			
18	*B. cereus*	–			

S/N – sample number.

References

1. Prakasham RS, Kumar BS, Kumar YS, Kumar KP. Production and characterization of protein encapsulated silver nanoparticles by marine isolate *Streptomyces parvulus* SSNP11. *Indian J Microbiol.* 2014;54(3):329–336.

2. Sun YG, Mayers B, Herricks T, Xia YN. Polyol synthesis of uniform silver nanowires: A plausible growth mechanism and the supporting evidence. *Nano Lett.* 2003;3(7):955–960.

3. Duran N, Marcato PD, Alves OL, Souza G, Esposito E. Mechanistic aspects of biosynthesis of silver nanoparticles by several *Fusarium oxysporum* strains. *J Nanobiotechnology.* 2005;3:1–7.

4. Meruvu H, Vangalapati M, Chippada SC, Bammid SR. Synthesis and characterization of zinc oxide nanoparticles and its antimicrobial activity against *Bacillus subtilis* and *Escherichia coli. Rasayan J Chem.* 2011;4(1):217–222.

5. Yedurkar S, Maurya C, Mahanwar P. Biosynthesis of zinc oxide nanoparticles using *Ixora coccinea* leaf extract: A green approach. *Open J Synth Theor Appl.* 2016;5(1):1–14.

6. Agarwal H, Venkat Kumar S, Rajeshkum S. A review on green synthesis of zinc oxide nanoparticles: An eco-friendly approach. *Resource-Efficient Technologies.* 2017;3(4):406–441.

7. Kolekar TV, Bandgar SS, Shirguppikar SS, Ganachari VS. Synthesis and characterization of ZnO nanoparticles for efficient gas sensors. *Arch Appl Sci Res.* 2013;5(6):20–28.

8. Applerot WE, Holleman AF. *Inorganic Chemistry.* Elsevier 22: 24–34 Brayner, Basu, 2006. Elsevier 2009; 1225–1229.

9. Lakshmi JV, Sharath R, Chandraprabha MN, Neelufar E, Abhishikta H, Malyasree P. Synthesis, characterization and evaluation of antimicrobial activity of zinc oxide nanoparticles. *J Biochem Technol.* 2012;3(5):S151–S154.

10. Gunalan S, Sivaraj R, Rajendran V. Green synthesized ZnO nanoparticles against bacterial and fungal pathogens. *Prog Nat Sci Mat Inter.* 2012;22(6):693–700.

11. Mahanty A, Mishra S, Bosu R, Maurya UK, Netam SP, Sarkar B. Phytoextracts-synthesized silver nanoparticles inhibit bacterial fish pathogen *Aeromonas hydrophila. Indian J Microbiol.* 2013;53(4):438–446. http://dx.doi.org/10.1007/s12088-013-0409-9

12. Ramesh P, Rajendran A, Meenakshisundaram M. Green synthesis of zinc oxide nanoparticles using flower extract *Cassia auriculata. Journal of NanoScience and NanoTechnology.* 2014;2(1):41–45.

13. Burkill HM. *The Useful Plants of West Africa, Familie E-I and J-L, 2 and 3.* 2nd ed. Kew, UK: Royal Botanic Gardens; 1995:151–153.

14. Doughari JH, Okafor B. Antimicrobial activity of *Senna alata* Linn. *East Central African J Pharmaceut Sci.* 2007;1(10):17–21.

15. Ogunti EO, Elujoba AA. Laxative activity of *Cassia alata* oil leaf. *Fitoterapia.* 1993;64:437–439.

16. Ogunjobi AA, Abiala MA. Antimicrobial activity of *Senna alata* and *Phyllanthus amarus. Global J Pharmacol.* 2013;7(2):198–202.

17. Salam AH, Sivaraj R, Venckatesh R. Green synthesis and characterization of zinc oxide nanoparticles from *Ocimum basilicum* L. var. *purpurascens* Benth.-Lamiaceae leaf extract. *Mater Lett.* 2014;131:16–18. http://dx.doi.org/10.1016/j.matlet.2014.05.033

18. Samat NA, Nor RM. Sol–gel synthesis of zinc oxide nanoparticles using *Citrus aurantifolia* extracts. *Ceram Int.* 2013;39:S545–S548.

19. Vijayakumar S, Vinoj G, Malaikozhundan B, Shanthi S, Vaseeharan B. *Plectranthus amboinicus* leaf extract mediated synthesis of zinc oxide nanoparticles and its control of methicillin resistant *Staphylococcus aureus* biofilm and blood sucking mosquito larva. *Spectrochim Acta Part A Mol Biomol Spectrosc.* 2015;137:886–891.

20. Jha AK, Kumar V, Prasad K. Biosynthesis of metal and oxide nanoparticles using orange juice. *J Bionanosci.* 2011;5(2):162–166. http://dx.doi.org/10.1166/jbns.2011.1053

21. Rajiv P, Rajeshwari S, Venckatesh R. Rambutan peels promoted biomimetic synthesis of bioinspired zinc oxide nanochains for biomedical applications. *Spectrochim Acta Part A Mol Biomol Spectrosc.* 2013;112:384–387.

22. Divyapriya S, Sowmia C, Sasikala S. Synthesis of zinc oxide nanoparticles and antimicrobial activity of *Murraya koenigii. World J Pharm Pharm Sci.* 2014;3(12):1635–1645.

23. Balouiri M, Sadiki M, Ibnsouda SK. Methods for in vitro evaluating antimicrobial activity: A review. *J Pharm Anal.* 2016;6(2):71–79.

24. Ambika, S, Sundrarajan M. Antibacterial behaviour of *Vitex negundo* extract assisted ZnO nanoparticles against pathogenic bacteria. *J Photochem Photobiol B.* 2015;146:52–57.

25. Suresh D, Nethravathi PC, Gowda UCH, Raja NNH, Bhushana N, Sharma SC. Green synthesis of multifunctional zinc oxide (ZnO) nanoparticles using *Cassia fistula* plant extract and their photodegradative, antioxidant and antibacterial activities. *Mat Sci Semiconductor Proc.* 2015;31:446–454.

26. Jamdagni P, Khatri P, Rana JS. Green synthesis of zinc oxide nanoparticle using flower extract of *Nyctanthes arbor-tristis* and their antifungal activity. *J King Saud Uni Sci.* 2018;30(2):168–175.

27. Ramesh M, Anbuvannan M, Viruthagiri G. Green synthesis of ZnO nanoparticles using *Solanum nigrum* leaf extract and their antibacterial activity. *Spectrochim Acta Part A Mol Biomol Spectrosc.* 2015;136 (Pt B):864–870.

28. Singh C, Sharma V, Naik PK, Khandelwal V, Singh H. A green biogenic approach for synthesis of gold and silver nanoparticles using *Zingiber officinale. Dig J Nanomat Bios.* 2010;6(2):535–542.

29. Chitsazi MR, Korbekandi H, Asghari G, Najafi RB, Badii A, Iravani S. Synthesis of silver nanoparticles using methanol and dichloromethane extracts of *Pulicaria gnaphalodes* (Vent.) Boiss. aerial parts. *Artif Cells Nanomed Biotechnol.* 2016;44(1):328–333.

30. Raliya R, Tarafdar JC. Biosynthesis and characterization of zinc, magnesium and titanium nanoparticles: An eco-friendly approach. *Interl Nano Let.* 2014;4:93.

31. He L, Rodda T, Haynes C, et al. Detection of a foreign protein in milk using surface-enhanced Raman spectroscopy coupled with antibody-modified silver dendrites. *Anal Chem.* 2011;83(5):1510–1513.

32. Dubey SP, Lahtinen M, Sillianpaa M. Tansy fruit mediated greener synthesis of silver and gold nanoparticles. *Process Biochem.* 2010;45(7):1065–1071.

33. Oboh PA, Abulu EO. The antimicrobial activities of extracts of *Psidium guajava* and *Citrus aurantifolia. Nig J Biotechnol.* 1997;8:25–27.

34. Dias MA, Lacerda ICA, Pimentel PF, de Castro HF, Rosa CA. Removal of heavy metals by an *Aspergillus terreus* strain immobilized in a polyurethane matrix. *Let Appl Microbiol.* 2002;34(1):46–50.

35. Iravani S, Zolfaghari B. Green synthesis of silver nanoparticles using *Pinus eldarica* bark extract. *Biomed Res Inter.* 2013;2013:639725.

36. Suliman RS, Ali H, Nurulain I, et al. Cinnamon bark extract for the formulation and characterisation of antimicrobial cream. *Inter J Res Ayurveda Pharm.* 2017;8(2):200–206.

The design of ibuprofen-loaded microbeads using polymers obtained from *Xanthosoma sagittifolium* and *Dillenia indica*

Tolulope Omolola Ajala[1,A–F], Boladale Olanrewaju Silva[2,A,C,E,F]

[1] Department of Pharmaceutics and Industrial Pharmacy, Faculty of Pharmacy, University of Ibadan, Nigeria
[2] Department of Pharmaceutics and Industrial Pharmacy, Faculty of Pharmacy, University of Lagos, Akoka, Nigeria

A – research concept and design; B – collection and/or assembly of data; C – data analysis and interpretation;
D – writing the article; E – critical revision of the article; F – final approval of the article

Address for correspondence
Tolulope Omolola Ajala
E-mail: tolulola1721@gmail.com

Abstract

Background. Ibuprofen is used both for acute and chronic disorders, such as ankylosing spondylitis, osteoarthritis and rheumatoid arthritis; however, ibuprofen causes gastrointestinal disturbances. Therefore, it would be desirable to design it as a sustained-release preparation.

Objectives. To design ibuprofen microbeads using polymers obtained from *Xanthosoma sagittifolium* starch and *Dillenia indica* mucilage to provide sustained-release delivery of ibuprofen.

Material and methods. The polymers were extracted using standard methods and characterized by their material, physicochemical, elemental, and rheological profiles. Microbeads loaded with ibuprofen were prepared using the ionotropic gelation method utilizing blends of the polymers and sodium alginate. The microbeads were evaluated using particle shape, particle size, swelling index, entrapment efficiency, and release assays.

Results. The results showed that the polymers have distinct material and physicochemical properties unique to their botanical sources. The microbeads were spherical and free-flowing, and they rolled without friction. The swelling properties ranged from 47.62 ±2.74% to 79.49 ±3.66%. The particle size of the microbeads ranged from 88.14 ±68.57 µm to 214.90 ±66.95 µm, while the encapsulation efficiencies ranged from 20.67 ±4.66% to 83.61 ±6.35%. The dissolution times suggested that the concentration of the natural polymers in the bead formulation could be used to modulate the dissolution properties. Generally, formulations containing the mucilage yielded higher dissolution times than those containing the starch. The kinetics of drug release from the microbeads containing the polymer blends generally fitted the Korsmeyer–Peppas model. The highest similarity was found between formulations C6 and D4 with f2 of 81.07.

Conclusions. The microbeads prepared with polymers obtained from *Xanthosoma* and *Dillenia* showed acceptable physicochemical properties, dependent upon polymer type, blend and concentration.

Key words: polymers, sodium alginate, ibuprofen microbeads, *Xanthoxylum sagittifolium* starch, *Dillenia indica* mucilage

Introduction

The oral route of drug administration constitutes the most convenient and preferred means of drug delivery into the systemic circulation. This is due to the ease of administration, the higher patient acceptance, adherence and compliance to medication, and the cost-effective manufacturing process.[1] Tablets and capsules are the most common oral dosage forms and are mostly prepared for immediate release, which enables rapid absorption.[2] Nonetheless, drugs with a low therapeutic index are prone to eliciting adverse effects because of fluctuating drug levels. In addition, drugs with a short half-life need to be frequently administered, which affects patient adherence and overall compliance to the treatment regimen.

The production of polymeric gel beads is a novel approach for achieving the controlled release of many therapeutic agents.[3] Microbeads are free-flowing and roll without friction, thus ensuring a dust-free environment during processing, in addition to a constant release rate for active agents embedded in the core.[5] Beads are discrete, spherical microcapsules that serve as a solid substrate; the drug is coated on this substrate or encapsulated within the core. Microbeads provide sustained-release properties and more uniform distribution of drugs within the gastrointestinal tract and enhance drug bioavailability. They are also called microspheres and described as carrier-linked drug delivery systems, in which particle size ranges from 1 μm to 1000 μm and the active drug is embedded in the core and coated at the outer layers with polymers. Microspheres can be described as structures made up of a continuous phase of 1 or more miscible polymers in which drug particles are dispersed at the molecular or macroscopic level. Microspheres constitute an important part of particulate drug delivery systems by virtue of their small size and efficient carrier capacity. Thus, drugs embedded in the microsphere matrix are released at a slow, constant and controlled rate; therefore, they are capable of being used for targeted delivery. The size, surface charge and surface hydrophilicity of microspheres have all been found to be important in determining the fate of the particles in vivo.[4] The use of small and round microbeads of the same size nullifies the disadvantages that are encountered with powders and granules.

Ibuprofen is widely known as a first-line non-steroidal anti-inflammatory drug (NSAID) for rheumatoid arthritis and chronic arthropathies. It also has an analgesic property and a mild antipyretic action. It acts mainly by inhibiting prostaglandin synthesis, reducing the production of pro-inflammatory cytokines such as interleukin 1β (IL-1β) and tumor necrosis factor α (TNF-α). It inhibits the lipoxygenase pathway, leading to a decrease in the production of leukotrienes by the leukocytes and the synovial cells. Furthermore, it masks the T cells, thereby suppressing the production of rheumatoid factors.

It is more active than indomethacin, naproxen and other NSAIDs. This drug is indicated for the relief of mild to moderate pain and inflammation in conditions such as dysmenorrhea, migraine, and postoperative and dental pain. In these disorders, an immediately available dose is required. Ibuprofen is also used in chronic disorders – such as ankylosing spondylitis, osteoarthritis and rheumatoid arthritis – for which a sustained release is desirable. The most frequent adverse effect occurring with ibuprofen is gastrointestinal disturbance; peptic ulceration, gastrointestinal bleeding, nausea, dyspepsia, dizziness, and unexplained rash have also been reported.[6] Low single-dose administration of ibuprofen and its short half-life in plasma (about 1.8–2.0 h) make it a very good candidate for the formulation of controlled-release, multiple-unit dosage forms.

Dillenia indica L. is a large evergreen shrub native to southeastern Asia, India, Bangladesh, and Sri Lanka.[7] The common English name is elephant apple or Indian catmon. Its characteristic fruits are large, round and greenish yellow, have many seeds and are edible.[7] The fruit pulp is bitter-sour and is used in curries, jams and jellies in India. It is often mixed with coconut and spices to make chutneys. The leaf, bark and fruit of this plant are traditionally used as medicine in different forms for their therapeutic value, such as their antidiabetic, antioxidant and antimicrobial properties.[8,9] The mucilage of the fruit is used to wash hair and has a conditioning effect.[10] There is potential to exploit the usefulness of *Dillenia* mucilage in microbead formulation, thus harnessing its potential as a pharmaceutical drug carrier. Cocoyam (*Xanthosoma sagittifolium* L. Schott) contains between 22% and 40% of starch, which is an essential component of food, providing about 60–70% of the daily caloric intake of humans.[11] Cocoyam starches are used as fillers in biodegradable plastics, as well as in aerosols because of their small size.[12] Despite the usefulness of cocoyam starch, it has remained largely underutilized, especially in different industrial applications.

The focus of the study, therefore, was to develop ibuprofen as microbeads using polymers obtained from *Dillenia indica* and *Xanthoxylum sagittifolium*. It is hoped that the ibuprofen microbeads will enable the administration of the drug as a controlled-release oral preparation which will protect the gastric mucous membrane from drug irritation, mask its unpleasant taste, avoid premature release in the gastrointestinal tract, reduce the frequency of administration, enhance patient compliance, minimize total drug quantity, improve bioavailability, prevent fluctuation in drug levels, and reduce the incidence of gastrointestinal disturbances. The use of natural polymers obtained from renewable resources will also aid in the development of local industries if those materials are eventually found to be acceptable. In the present study, therefore, an ibuprofen microbead was designed using polymers obtained from *Dillenia indica* and *Xanthoxylum sagittifolium*.

Material and methods

Material

The materials used were: sodium alginate (Carl Roth GmbH & Co, Karlsruhe, Germany), calcium acetate (Alfa Aesar GmbH & Co, Karlsruhe, Germany); potassium dihydrogen phosphate (Lab Tech Chemicals, Windsor, Australia), disodium hydrogen dodecahydrate (Hopkin and Williams, Essex, UK), sodium hydroxide pellets (Lab Tech Chemicals), xylene (BDH Chemicals Ltd., Poole, UK), and ibuprofen (Fidson Healthcare Plc, Ota, Nigeria). All other reagents were of analytical grade. The tubers of *Xanthosoma sagittifolium* (cocoyam) were procured from a local market in Ibadan, in the southwestern part of Nigeria, while the *Dillenia indica* fruits were obtained from the botanical garden of the University of Ibadan, Nigeria.

Extraction and purification of polymers

Preparation of *Xanthosoma* starch

The *Xanthosoma* starch was extracted from mature tubers according to an established procedure. The cocoyam tubers were peeled, cut into pieces, washed, weighed (10.0 kg), and soaked in distilled water containing sodium metabisulfite for 24 h to encourage softening. The mass was then reduced to a fine pulp through wet milling using a milling machine (GEC Machines Ltd., Blackheath, UK). The fine pulp was passed through a muslin cloth to remove all debris and fibers, resulting in a milky liquid. This liquid was washed several times with distilled water and sieved through a 250-micrometer mesh sieve. The washing was continued until the supernatant no longer tested positive in an acidity test. The starch was dried at 50°C for 18 h. The dried starch was powdered in a laboratory mill, passed through a 125-micrometer mesh sieve, and weighed before being packaged in an airtight container and stored at room temperature.

Preparation of *Dillenia* mucilage[13]

Fruits of *Dillenia indica* were cut open and the inner part containing the mucilaginous material was scooped out and soaked for 24 h in chloroform water. It was strained through a muslin cloth to remove extraneous materials and then precipitated using ethanol (96% v/v). The precipitated mucilage was filtered and washed with diethyl ether before being dried at 50°C for 48 h. It was pulverized and kept in airtight containers.

Determination of particle size for polymers

The particle sizes were measured using an optical microscope fitted with a camera and Motic MC 1000 computer software (Motic China Group Co. Ltd., Xiamen, China). One hundred particles were measured and the mean size was calculated.

Determination of particle density

The particle densities were determined using a pycnometer with xylene as the displacement fluid. An empty 50-milliliter pycnometer was weighed (W), then filled with xylene; the excess fluid was wiped off and the full bottle was weighed (W_1). The difference between W_1 and W was recorded as W_2. A two-gram sample was weighed (W_3) and transferred into the full pycnometer. The excess solvent was wiped off and the bottle was weighed again (W_4). The particle density (pt) in g/cm^3 was then calculated using Equation 1:

$$\text{particle density } = \frac{W_2 * W_3}{50\{(W_3 - W_4) + (W_2 - W_1)\}} \tag{1}$$

Determination of ash content

A porcelain crucible was washed and dried in an oven. It was then allowed to cool in a desiccator before being weighed. The dried polymer material was weighed into the empty crucible. The material was ignited over a low flame in the fume cupboard to char the organic matter. The crucible was then placed in a muffle furnace maintained at 600°C for 6 h. On removal from the furnace, the crucible was transferred into a desiccator, cooled and weighed immediately. The percentage of ash content was calculated using Equation 2:

$$\text{ash content (\%) } = \frac{(\text{weight of crucible} + \text{ash}) - (\text{weight of empty crucible}) \times 100}{\text{sample weight}} \tag{2}$$

Crude fat analysis

Each thimble was loaded with about 3 g of the starch sample and plugged with cotton wool.[14] The thimbles were dried and then inserted into a Soxtec^{TM} HT device (Foss, Hilleroed, Denmark) and extracted for 15 min in the "boiling" position, then for 45 min in the "rising" position. The solvent was then evaporated and the cups were released and dried at 100°C for 30 min. After this, the cups were cooled in a desiccator and weighed. The same procedure was repeated for the mucilage and the fat content was calculated using Equation 3,

$$\text{fat content (\%) } = \frac{(W_3 - W_2)}{W_1} \times 100 \tag{3}$$

where W_3 = the weight of the cup with the extracted fat
W_2 = the weight of the empty cup
W_1 = the weight of the sample.

Determination of crude protein content

The dried starch sample (1 g) was weighed into a digestion tube and 15 mL of concentrated sulfuric acid was added to it. Seven Kjeldahl catalyst tablets were added into the tube which was pre-set at 410°C. It was then digested for 45 min until there was a clear solution.

The tube was placed in the distillation unit and 50 mL of 40% sodium hydroxide solution was dispersed into it. The digest was distilled into 25 mL of 4% boric acid for 5 min. The distillate was titrated against 0.47 M hydrochloric acid until a grey color was obtained.

$$\% \text{ crude protein} = \% \text{ total nitrogen} \times \text{conversion factor} \qquad (4)$$

Determination of swelling index

The starch or mucilage was transferred to a 100-milliliter cylinder (V1), 90 mL of distilled water was added, and the slurry was shaken for 5 min and then topped up to 100 mL. The suspension was allowed to stand for 24 h and the sedimentation volume (V2) was measured. The swelling index was calculated using Equation 5:

$$\text{Swelling index} = \frac{V_2 - V_1}{V_1} \times 100 \qquad (5)$$

Solubility

Starch/mucilage (1 g) was weighed (W) into a 150-milliliter conical flask. Distilled water (15 mL) was added and the mixture shaken for 5 min, then placed into a heated water bath and kept at 80°C for 40 min with constant stirring. The starch slurry was then transferred into a pre-weighed centrifuge tube (W1); 7.5 mL of distilled water was added and the slurry centrifuged at 2,200 rpm for 20 min. The supernatant was carefully decanted into a tarred dish (W2) and dried at 100°C to a constant weight (W3), then it was cooled in a desiccator. The solubility was calculated using Equation 6:

$$\text{Solubility (\%)} = \frac{(W_2 - W_3)}{W_1} \times 100 \qquad (6)$$

Water absorption capacity

To each 1-gram sample, 15 mL of distilled water was added in a weighed 25-milliliter centrifuge tube. The tube was agitated in a vortex mixer for 2 min and centrifuged at 4,000 rpm for 20 min. It was then decanted and the clear supernatant discarded. The residue was weighed (W1). The adhering droplets of water were removed by drying the residue at 60°C to a constant weight (W2). The water absorption capacity (WAC) was then calculated as the weight of water bound by 100 g of dry powder.

Fourier-transform infrared spectroscopy

The Fourier-transform infrared (FTIR) spectra were recorded on the polymer samples prepared in potassium bromide (KBr) discs using an FTIR system (Spectrum BX 273; PerkinElmer, Waltham, USA). The scanning range was 350–4400 c^{-1}.

Preformulation studies

Preformulation studies were carried out in order to optimize the formulation and physicochemical properties of the microbeads. Several formulation trials were carried out using varying concentrations (5%, 7.5% and 10% w/v) of the extracted polymers alone. The polymers alone did not form discrete beads, and the few which did form could not retain their integrity outside the chelating agents. Thus, various polymer blends consisting of different ratios of natural polymers and sodium alginate were used, as shown in Table 4.

Preparation of microbeads

Ibuprofen microbeads were prepared from the hot gel blend (90°C) of natural polymer and sodium alginate using the ionotropic gelation method.[15] The natural polymer and sodium alginate were blended in order to obtain a total polymer concentration of 2% w/v at ratios of 1:1, 1:2, 1:3, 1:4, 2:1, 3:1, and 4:1. An appropriate quantity of the drug (1 g) was added, such that the ratio of total polymer to drug was 2:1. The resulting dispersion was extruded using a syringe with a 0.90-millimeter needle at a dropping rate of 2 mL/min into a calcium acetate solution (10% w/v) maintained under agitation at 300 rpm using a magnetic stirrer (Talboys Laboratory Stirrer Model No. 102; Troemner, Thorofare, USA). The formed beads were allowed to cure for 30 min and were then left standing for another 30 min. The beads were collected by decanting, washed repeatedly with distilled water, and then dried for 24 h in a hot-air oven (Gallenkamp BS 250 Oven; Riley Industries Ltd, West Midlands UK) at 40°C.

Size and morphology of beads

The particle sizes of the microbeads were determined using the optical microscopy method. The particle sizes of 100 prepared microbeads were determined with optical microscopy using a light microscope (Leitz Laborlux II; Leica Microsystems, Wetzlar, Germany). The shape of the beads was also determined using light microscopy.

Swellability of beads

In order to determine the swellability, 100 mg of microbeads was soaked in 20 mL of phosphate buffer (pH 6.8) for 3 h. The microbeads were then removed and excess buffer was wiped away using a dry filter paper; the final weight of microbeads was determined. The swollen microbeads were handled carefully in order to avoid any loss of mass due to erosion. The experiment was repeated after 6 h and 24 h. Swellability – otherwise known as the swelling index – was computed using Equation 7,

$$\text{swelling index (\%)} = \frac{C}{I} \times 100 \qquad (7)$$

where C is the weight gain and I is the initial weight of the microbeads.

Entrapment efficiency

The ibuprofen microbeads (50 mg) were accurately weighed and crushed in a glass mortar and suspended in 10 mL of phosphate buffer (pH 6.8) with intermittent stirring. After 24 h, the solution was filtered. The filtrate was appropriately diluted using phosphate buffer (pH 6.8) and analyzed spectrophotometrically at 225 nm with a UV/VIS spectrophotometer (LAMBDA 12; Perkin Elmer GmbH, Rodgau, Germany). The drug entrapment efficiency (E) was calculated as in Equation 8,

$$E\,(\%) = \frac{A}{T} \times 100 \qquad (8)$$

where A and T are the actual and theoretical contents of ibuprofen, respectively.

Drug release study

The drug release behavior of the microbeads was evaluated in 900 mL of phosphate buffer (pH 6.8) maintained at 37 ±0.5°C using the paddle method (USP XXI), rotated at 100 rpm. Samples (10 mL) were withdrawn at different time intervals and replaced with an equal amount of fresh medium. The amount of ibuprofen released was determined at a wavelength of 225 nm using a UV/visible spectrophotometer (LAMBDA 12). Measurements were done in triplicate.

Modeling of release profile

Data obtained from in vitro release studies were used in various kinetic equations to determine the kinetics and mechanism of drug release from the microbeads. The results of the drug release for the formulation was fitted to zero order, first order, Higuchi, Hixson–Crowell, Korsemeyer–Peppas, and Hopfenberg equations.[16–19] The model of best fit was identified by comparing the values of correlation coefficients.

Data presentation and analysis

The experiments were conducted in triplicate and the mean determined. Statistical analysis was carried out using analysis of variance in GraphPad Prism v. 4.0 (Graph-Pad Software Inc., San Diego, USA) to compare the differences between formulations. The similarity factor (f_2) was used to determine whether formulations prepared using the extracted polymers were similar to those prepared using the standard polymer sodium alginate. A p-value ≤0.05 was considered statistically significant.

Results and discussion

Material and physicochemical properties of the polymers

The material and physicochemical properties of *Xanthosoma sagittifolium* starch and *Dillenia indica* mucilage are presented in Table 1. It includes values for pH, moisture content, solubility, water absorption capacity, swelling index, crude protein, fat, ash and carbohydrate contents, density values, and flow parameters. There were distinct differences between the starch and mucilage, though both polymers had low values of water absorption capacity. Generally, low values of this parameter indicate a compact structure of polymers.[20] In this study, the starch was found to be more compact than the mucilage. The starch also had low levels (<1%) of protein fat and ash content, which implies high purity as a high ash content would imply the presence of sand. The content of these proximate parameters usually vary with the botanical source of the starch: for the mucilage, which is gummy, the protein and fat content were >1% and the ash content was also very low. Generally, gums and mucilage have nitrogenous compounds, hence the protein. The starch had a higher carbohydrate content than the mucilage. The carbohydrate content is higher than any other proximate parameter, illustrating that they are true polysaccharides.

The pH of the starch was higher than that of the mucilage, but within the acceptable range for excipients used in oral formulations. It is not expected that the pH should be acidic, hence in terms of PH, the polymers were acceptable. The moisture content of the mucilage was higher than that of the starch, but both were within the acceptable range to keep an excipient free of microbial growth and deterioration. The maximum water content prescribed for safe storage of starch is 13%w/w, while pharmacopoeial limit for natural gums and mucilage is ≤15.0%; the moisture in a material should be moderate to prevent enzymatic activation of the degradation processes.[21]

Table 1. Material and physicochemical properties of *Xanthosoma sagittifolium* starch and *Dillenia indica* mucilage

Parameters	*Xanthosoma sagittifolium* starch	*Dillenia indica* mucilage
pH	6.471 ±0.281	4.120 ±0.181
Moisture content [%]	6.011 ±0.005	7.271 ±0.010
Solubility [%]	1.851 ±0.07	2.462 ±0.101
Water absorption capacity [%]	8.23 ±0.25	5.67 ±2.12
Swelling index [%]	1.172 ±0.112	272.741 ±0.211
Crude protein [%]	0.470 ±0.001	4.841±0.002
Fat [%]	0.401 ±0.004	3.402 ±0.021
Ash [%]	0.498 ±0.022	0.461 ±0.003
Carbohydrate [%]	91.23 ±1.03	89.56 ±0.17
Particle density [g/mL]	1.257 ±0.004	1.358 ±0.023
Particle size [µm]	16.870 ±8.08	47.372 ±5.26

The moisture content of the natural polymers used in this study was within the pharmacopoeial limits, testifying to their quality. The mucilage was more soluble than the starch, but the starch was better at binding water. The mucilage was bulkier and had denser particles than the starch, while the tapped density for the starch was higher, indicating an improved packing property over the mucilage. The mucilage has significantly larger particles (p < 0.05).

The functional group bands of the natural polymers obtained from FTIR spectra are presented in Table 2. The characteristic functional groups are reflected from the peaks of absorbance. The different classes of functional groups present in the polymers imply that they are complex polysaccharides.

Viscosity of polymer blends

The viscosity of polymer blends is presented in Table 3. *Dillenia* had higher viscosity (52.00 ±0.01 cP) than *Xanthosoma* (14.00 ±0.06 cP) at the same concentration, but the viscosity of alginate (532.00 ±14.00 cP) was significantly higher (p < 0.05) than of each of the polymers. Generally, *Dillenia*/alginate blends yielded significantly higher viscosities (p < 0.05).

Physicochemical properties of the microbeads

The freshly prepared microbeads were spherical in shape, as shown in Fig. 1. Those prepared using *Xanthosoma* alginate blends (C1 and C4) were whitish in color, while those prepared using *Dillenia*/alginate blends were light brown in color. The photomicrographs of the dried microbeads

Table 2. Antibacterial activity and MIC of SaZnONPs against some pathogenic bacteria

Wave number [cm^{-1}]	Class	Assignment
Xanthosoma		
604	alkynes	R CH
880	aromatics, amines	C–H out of plane
894	alkenes	R2C=CH2
1172	alkyl halides	R–F
1306	carboxylic acid esters	C–O stretch
2950	alkanes	CH2 CH3
3040	aromatics	Ar–H
Dillenia		
772	aromatics	C–H out of plane
1095	alcohols	C–O stretch
1451	alkanes	CH2 CH3
1541	miscellaneous	N–H out of plane
2705	aldehydes	RCHO C–H
3353	carboxylic acids	dimer OH
3447	amines	N–H stretch

Table 3. The composition and viscosity of polymer blends used for the formulation of ibuprofen-loaded microbeads (mean ±SD; n = 3)

S/N	Polymers	Polymer ratio	Microbead formulation code	Viscosity [cP]
1	Alginate	1:0	A1	532.00 ±4.00
2	*Xanthosoma*/alginate	1:1	C1	666.67 ±15.28
3	*Xanthosoma*/alginate	1:2	C2	763.33 ±15.28
4	*Xanthosoma*/alginate	1:3	C3	826.67 ±24.17
5	*Xanthosoma*/alginate	1:4	C4	896.00 ±4.57
6	*Xanthosoma*/alginate	2:1	C5	520.00 ±4.00
7	*Xanthosoma*/alginate	3:1	C6	470.00 ±17.32
8	*Xanthosoma*/alginate	4:1	C7	372.00 ±4.00
9	*Xanthosoma*/alginate	1:0	C8	14.00 ±0.06
10	*Dillenia*/alginate	1:1	D1	3883.33 ±76.38
11	*Dillenia*/alginate	1:2	D2	4029.33 ±8.33
12	*Dillenia*/alginate	1:3	D3	4516.67 ±37.86
13	*Dillenia*/alginate	1:4	D4	4856.67 ±40.42
14	*Dillenia*/alginate	2:1	D5	2256.00 ±4.00
15	*Dillenia*/alginate	3:1	D6	2532.00 ±4.00
16	*Dillenia*/alginate	4:1	D7	2800.00 ±62.45
17	*Dillenia*/alginate	1:0	D8	52.00 ±0.01

SD – standard deviation; S/N – sample number.

are presented in Fig. 2. Generally, they were spherical and had a rough surface, possibly due to the drying procedures. The bead shape and rough surface are consistent with the findings of Akin-Ajani et al.[22] who used date mucilage blended with sodium alginate to prepare beads.

The physicochemical properties and dissolution times of the microbeads are presented in Table 4. The microbeads prepared with blends of the polymers and alginate yielded a higher swelling index than the one from alginate alone. Microbeads from *Xanthosoma*/alginate blends resulted in a swelling index ranging between 47.62 ±2.74% and 60.52 ±5.02%, while *Dillenia*/alginate blends yielded a 51.92 ±3.45% to 79.49 ±3.66% swelling index. This shows that *Dillenia* imparted higher swelling properties than *Xanthosoma*. Equal blends of *Xanthosoma* and alginate resulted in 50.17 ±4.91%, while blends of *Dillenia* and alginate (70.32 ±2.43%) had significantly higher swelling (p < 0.05). Generally, swelling increased over time, but the differences were not significant; within 3 h, the beads would have swollen to about 90% of their capacity.

Bead size is an important parameter in the evaluation of microbeads, since the size determines where it fits within the classification.[23] All the formulations were within the acceptable size range for microbeads (1–1000 μm). The size of the beads prepared using *Xanthosoma*/alginate blends was from 88.14 ±68.57 μm to 189.00 ±54.20 μm. The sizes increased as the concentration of alginate increased in the blends (C1 to C4), which was also true for beads which contained more *Xanthosoma* than alginate (C5 to C7). The particle size for the beads prepared using *Dillenia*/alginate
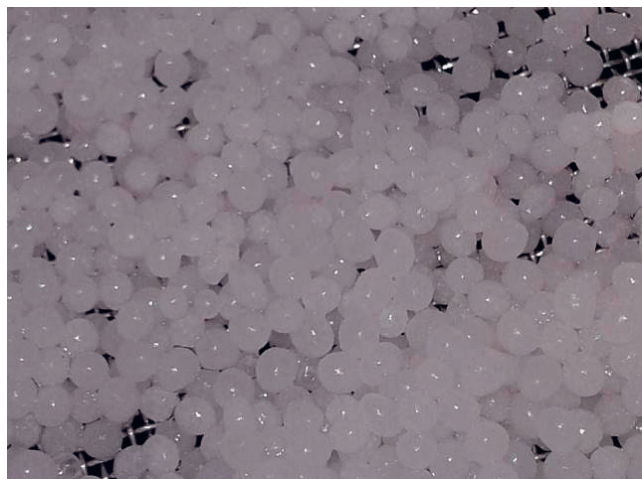
Polymer blends of *Xanthosoma sagitifolium* starch and sodium alginate in ratio 1:1 (C1)
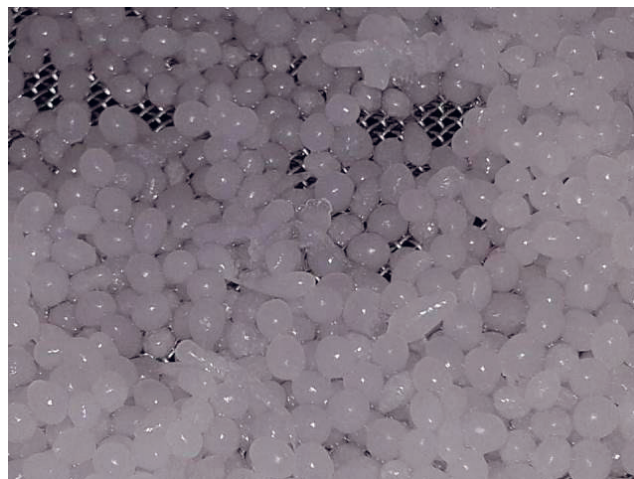
Polymer blends of *Xanthosoma sagitifolium* starch and sodium alginate in ratio 1:4 (C4)

Polymer blends of *Dillenia indica* and sodium alginate in ratio 1:1 (D1)

Polymer blends of *Dillenia indica* and sodium alginate ratio 1:3 (D3)

Fig. 1. Representative figures of freshly prepared ibuprofen-loaded microbeads using different polymer blends

Table 4. Physicochemical properties and dissolution times of ibuprofen-loaded microbeads prepared with polymer blends

| Formulation code	Swelling index		Mean particle size [μm]	Encapsulation efficiency [%]	Dissolution times [min]	
	3 h	24 h			t_{25}	t_{80}
A1	44.41 ±2.67	53.49 ±3.78	178.80 ±2.46	57.72 ±3.31	94.68	302.96
C1	50.17 ±4.91	59.18 ±4.44	88.14 ±68.57	52.90 ±2.77	84.95	271.84
C2	47.62 ±2.74	50.02 ±5.23	88.37 ±59.74	56.60 ±4.24	77.74	248.77
C3	56.54 ±4.32	64.22 ±3.45	147.20 ±46.46	64.86 ±5.43	83.82	268.24
C4	50.02 ±1.89	60.98 ±3.08	189.00 ±54.20	71.83 ±5.63	111.27	356.06
C5	52.70 ±3.28	56.96 ±7.09	158.23 ±62.81	40.00 ±3.94	107.18	342.99
C6	49.95 ±3.57	57.84 ±6.78	162.70 ±57.46	51.96 ±5.22	85.44	273.41
C7	60.52 ±5.02	69.22 ±3.45	183.10 ±46.55	83.61 ±6.35	79.38	254.01
D1	70.32 ±2.43	75.09 ±5.62	170.70 ±50.54	69.51 ±5.11	121.36	388.34
D2	57.98 ±5.12	63.28 ±5.32	175.10 ±50.06	20.67 ±4.66	76.97	246.29
D3	51.92 ±3.45	57.23 ±4.14	175.50 ±53.88	28.13 ±5.39	113.36	362.76
D4	57.36 ±3.62	60.24 ±5.68	190.00 ±66.36	60.82 ±7.18	86.70	277.44
D5	68.25 ±4.55	76.77 ±4.65	214.90 ±66.13	52.39 ±3.79	97.94	313.39
D6	79.49 ±3.66	82.83 ±5.56	174.11 ±54.92	64.09 ±4.66	128.14	410. 05
D7	76.77 ±7.09	78.21 ±5.64	195.32 ±53.06	66.07 ±5.35	125.78	402.50
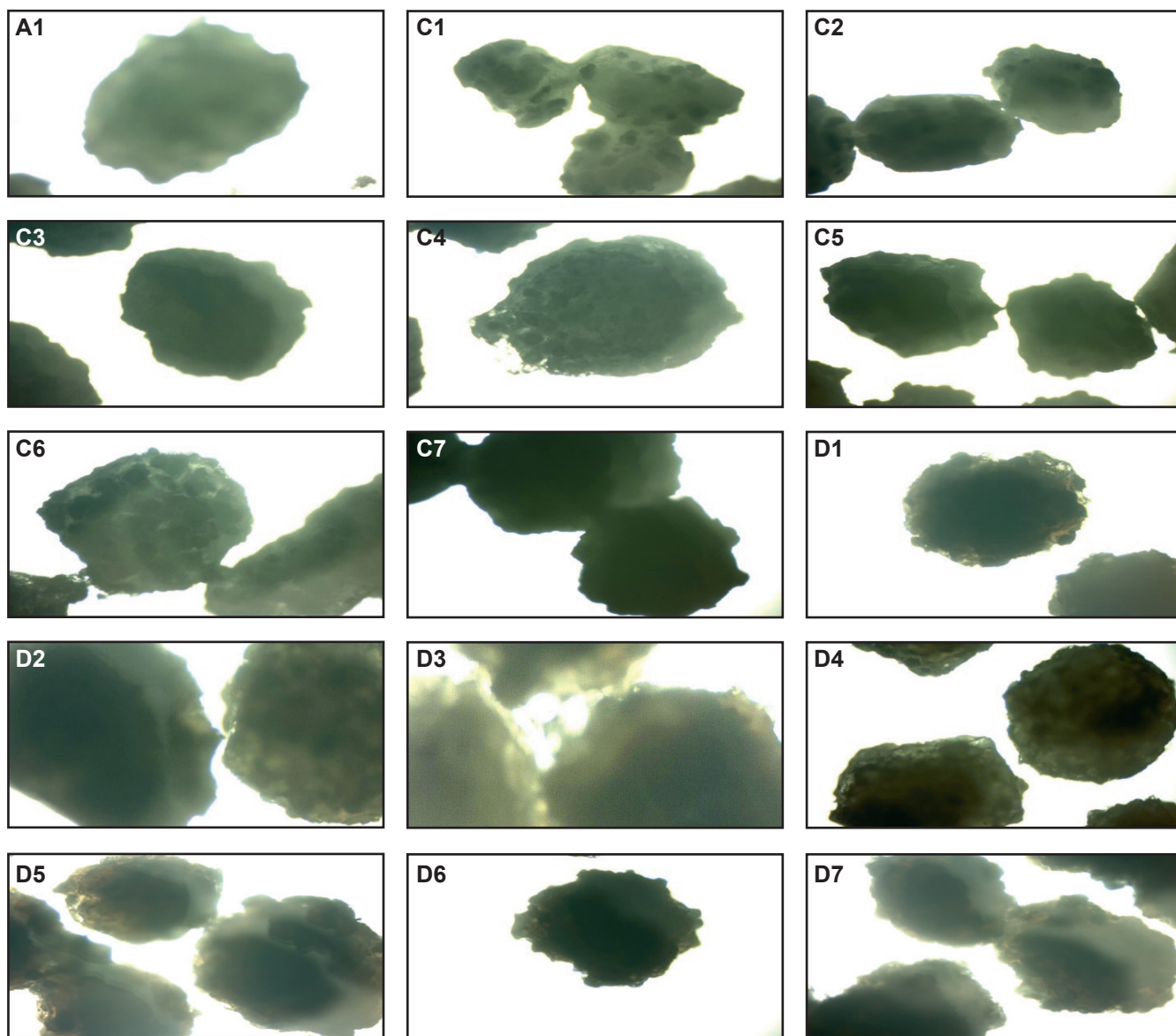
Fig. 2. Photomicrographs of ibuprofen-loaded microbeads containing polymer blends. A1 – Sodium alginate only as polymer. C1–C7 – polymer blends of *Xanthosoma* and alginate. D1–D7 – polymer blends of *Dillenia indica* and alginate

blends was from 170.70 ±50.54 µm to 214.90 ±66.95 µm. The beads were therefore larger than those prepared using *Xanthosoma*. The sizes also increased as the concentration of alginate increased in the blends (D1 to D4), but there was no particular trend for beads which contained more *Dillenia* than alginate (D5 to D7).

The range of encapsulation efficiency (EE) for beads containing *Xanthosoma*/alginate blends in increasing concentrations of alginate (C1 to C4) was from 52.90 ±2.77% to 71.83 ±5.63%. *Xanthosoma*/alginate blends containing increasing amounts of *Xanthosoma* (C5 to C7) yielded beads with an EE range from 40.00 ±3.94% to 83.61 ±6.35%. *Dillenia*/alginate blends with increasing concentrations of alginate (D1 to D4) resulted in EE values ranging from 20.67 ±4.66% to 69.1 ±5.11%. D1, which consisted of an equal blend of *Dillenia* and alginate, offered the highest EE.

The microbeads from polymer blends with increasing concentrations of *Dillenia* (D5 to D7) yielded increasing levels of EE, ranging between 52.39 ±3.79% and 66.07 ±5.35%. This implies that for microbeads prepared using starch, the more the alginate, the higher the EE for *Xanthosoma*/alginate polymer blends C1–C4. For C5–C7, the EE increased as the concentration of starch increased. This implies that the starch and sodium alginate particles interacted in such a way that the EE of the system improved. In both directions of blending starch and sodium alginate, there was a positive outcome on the EE. For microbeads prepared using *Dillenia* and sodium alginate blends, formulation D1 – with an equal concentration of the polymers – offered the highest EE. As the concentration of alginate increased (D1–D4), there seemed to be no particular pattern in the EE. However, as the concentration of *Dillenia* increased in the polymer blend

(D5–D7), there was a consistent increase in EE. This indicates that an increase in the amount of *Dillenia* in the polymer blend favored the encapsulation of ibuprofen.

Drug release properties of the microbeads

In vitro dissolution has been recognized as an important element in drug development. It can also be used as a substitute for the assessment of bio-equivalence. The mechanism of drug release is affected by the properties of the core materials, including solubility, diffusibility and partition coefficient.[24] In addition, diffusion-controlled drug release occurs where the drug molecules are uniformly dispersed within the polymer.[25] The release profiles of ibuprofen from the microbead formulations in Fig. 3 demonstrate a moderate release over time. Formulation C4 from a *Xanthosoma*/alginate blend ratio of 1–4 (i.e., 20% starch), formula D1 from a *Dillenia*/alginate blend ratio of 1:1 (50% mucilage) and formulation A1 (100% sodium alginate) all exhibited a gradual release over time and were considered to deliver optimum properties in this regard. In controlled release formulations, it is not desirable that an initial high rate of drug release – usually referred to as "burst release" (a situation in which 15% of a drug is released within the 1st hour) – should occur. This allows for avoiding adverse drug effects and the possibility of rendering the delivery system ineffective.[26] In formulations C4, D1 and A1, the release profiles show that the embedded drugs were not loosely bound to the surface of the beads, hence the gradual release.

The dissolution times shown in Table 4 for microbeads prepared with starch in alginate polymer blends demonstrate that the concentration of the natural polymers could be used to modulate the dissolution properties from the microbead formulations. Generally, as alginate increased in the starch/alginate blends (1:2 to 1:4), the dissolution times for ibuprofen release increased, show-

ing that delayed release properties were conferred onto the formulation. However, equal quantities of starch and alginate (1:1) did not follow this pattern in the blends, as its dissolution times resembled a 1:3 ratio. Thus, the ranking of dissolution times among the microbead formulations of starch/alginate blends containing increasing alginate quantity was C4 > C1 > C3 > C > C2.

Formulations C5–C7 contained increasing quantities of the starch, and the dissolution times from these blends reduced as the starch concentration increased. This suggests that larger concentrations of the starch may not confer delayed release properties as much as the other concentrations. For delayed release properties, formula C4 produced the longest dissolution times – 25% of the drug was released in nearly 2 h and 80% was released in approx. 6 h; these dissolution times were much longer than those of formulations prepared using alginate alone. The presence of starch modified the dissolution times which the alginate provided to the microbeads.

Generally, formulations containing the mucilage and alginate blends yielded longer dissolution times compared to those containing the starch. The dissolution times of microbeads prepared with blends of mucilage and alginate in increasing alginate concentrations (1:1 to 1:4) were ranked as follows: D1 > D3 > D4 > D2. As with the starch/alginate blends, a 1:2 ratio produced the shortest dissolution times. A 1:1 mucilage/alginate blend yielded the longest dissolution times, whereas with the starch 1:4 was the longest. Formula D1 yielded dissolution times of over 2 h for a release of 25% and almost 6.5 h for 80% drug release. The ranking of dissolution times for formulations obtained from mucilage/alginate blends with increasing concentrations of mucilage (2:1 to 4:1 ratios) was D6 > D7 > D5. This shows that a 3:1 ratio produced microbeads with the slowest release, thus conferring better delayed-release properties on the formulations.

In terms of dissolution times, formula D6 containing a 3:1 mucilage/alginate blend provided optimal values: 25% drug release was achieved in over 2 h, while 80%
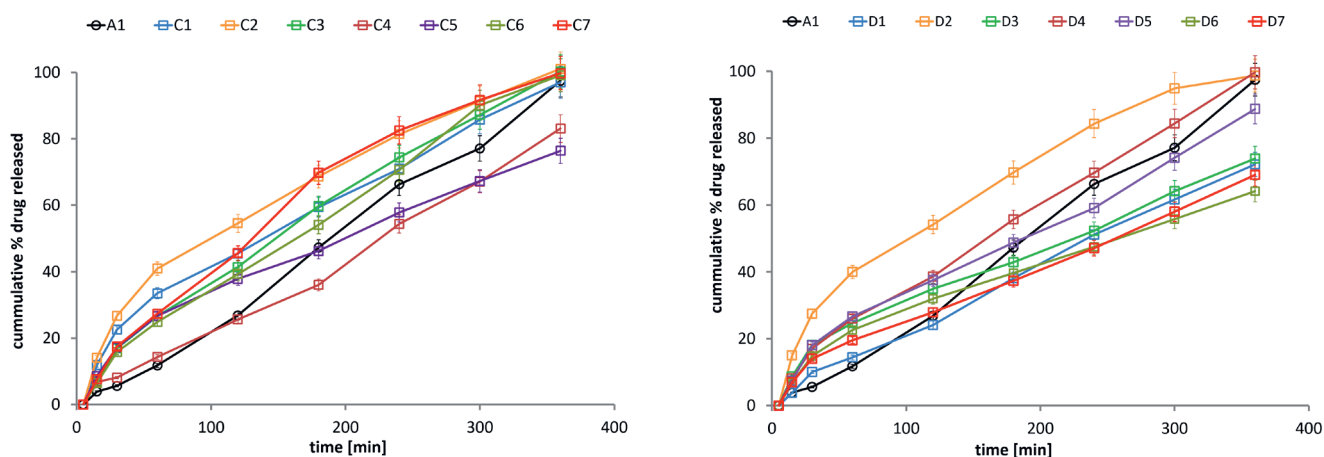
Fig. 3. Dissolution profiles of ibuprofen-loaded microbeads prepared with polymer blends. A1 – Sodium alginate only as polymer. C1–C7 – polymer blends of *Xanthosoma* and alginate. D1–D7 – polymer blends of *Dillenia indica* and alginate

was released after nearly 7 h. These results are comparable to the studies of Odeku et al. on the design of microbeads using 4 natural gums.[26] Their report showed that the dissolution times of beads containing natural gums (irvingia, khaya and cissus) were longer at a ratio of 3:1 for natural gum/alginate blends. In the current study, *Dillenia* mucilage seemed to follow the pattern of 3 of the natural gums.

The kinetics of drug release is important due to its influence on drug bioavailability, dosage intervals, and the occurrence of toxicity or unwelcome side effects.[24] The correlation coefficients obtained from fitting the release data to different kinetic models are presented in Table 5. The kinetics of drug release from the microbeads containing the polymer blends fitted the Korsmeyer–Peppas (A1, C1, C2, C3, C5, C6, and D1–D7) and Hopfenberg (C4 and C7) models using correlation coefficients (r^2 = 0.9902–0.9970).

The Korsmeyer–Peppas model of drug release is useful in describing the release from polymeric systems. The rate of release for the model is related to the structural and geometric properties of the drug delivery systems, in this case with the polymers serving as carriers. The model also provides a release exponent "n", which corresponds to the mechanism of the release. Generally, in this study, the drug release from the microbeads was controlled by a combination of diffusion and erosion mechanisms. The release mechanism using the n-value for most of the beads corresponds to mass transfer following a non-Fickian anomalous $0.5 < n < 1.0$ diffusion. However, formula C4 yielded an n-value of 1.045 and A1 (made from alginate) of 1.105, which indicates that the drug release from these microbeads was controlled

by super case II transport, in which a pronounced acceleration of drug release from the microbeads occurred toward the latter stages of release, resulting in a more rapid relaxation-controlled transport. In addition, the drug release from formulations C4 and C7, prepared from *Xanthosoma*/alginate blends, fit the Hopfenberg model (r^2 = 0.9955 and 0.9966, respectively).

The Hopfenberg model describes the release of a drug from spherical formulations, and the mathematical model is used for correlating the drug release from a surface-eroding polymer for as long as the surface remains constant during the degradation process. The physicochemical properties of the drug and the polymer, as well as the drug-to-polymer ratio, have been shown to govern the release of a drug from formulations, which could mean that the amount of the polymer could be used to modify the release properties of the microbeads.

Conclusions

The polymers obtained from *Xanthosoma sagittifolium* and *Dillenia indica* had different physicochemical properties, such as particle size, shape and viscosity. The ibuprofen microbeads were discrete, generally spherical and with a particle size <250 μm. The bead swelling depended on the type and concentration of the natural polymer present in the polymer blend. The entrapment efficiencies for the beads ranged from 20% to 30% and the microbeads demonstrated controlled release properties. Ibuprofen microbeads were successfully formulated with properties varying according to polymer type and concentration.

Table 5. Correlation coefficients obtained for ibuprofen microbeads using different mathematical models (n = 3)

| Formulation code | Zero order | First order | Higuchi | Korsmeyer–Peppas | | Hixson–Crowell | Hopfenberg |
				r^2	n		
A1	0.9936	0.9257	0.8344	0.9966*	1.105	0.9529	0.9951
C1	0.9189	0.9724	0.9662	0.9918*	0.649	0.9736	0.9743
C2	0.8526	0.9788	0.9809	0.9892*	0.575	0.9720	0.9788
C3	0.9734	0.9712	0.9351	0.9974*	0.772	0.9872	0.9934
C4	0.9940	0.9494	0.8566	0.9945	1.045	0.9679	0.9955*
C5	0.9164	0.9801	0.9678	0.9926*	0.646	0.9700	0.9801
C6	0.9837	0.9584	0.9171	0.9956	0.828	0.9783	0.9924
C7	0.9467	0.9784	0.9427	0.9896	0.718	0.9936	0.9966
D1	0.9947	0.9810	0.8912	0.9970*	0.918	0.9909	0.9965
D2	0.8454	0.9803	0.9798	0.9873*	0.571	0.9759	0.9806
D3	0.9182	0.9687	0.9618	0.9878*	0.652	0.9603	0.9687
D4	0.9782	0.9635	0.9281	0.9960*	0.795	0.9799	0.9887
D5	0.9550	0.9697	0.9403	0.9885*	0.732	0.9742	0.9744
D6	0.9094	0.9704	0.9693	0.9916*	0.636	0.9569	0.9704
D7	0.9621	0.9785	0.9372	0.9902*	0.749	0.9783	0.9789

* Highest correlation coefficient of drug release kinetics.

ORCID iDs

Tolulope Omolola Ajala https://orcid.org/0000-0002-1257-746X
Boladale Olanrewaju Silva https://orcid.org/0000-0003-2115-6090

References

1. Kumar KPS, Bhowmik D, Dutta A, Paswan S, Deb L. Recent trends in scope and opportunities of control release oral drug delivery systems. *Pharm Sci*. 2012;1(1):20–40.
2. Ajala TO, Akin-Ajani OD, Odeku OA. Recent advances in oral drug delivery systems. In: Violiani V, ed. *Recent Advances in Drug Delivery Research*. New York, NY: Nova Science Publishers Inc.; 2013:33–50. ISBN: 978-1-62948-228-6.
3. Chien YW. *Novel Drug Delivery Systems*. 2nd ed. New York, NY: Marcel Dekker Inc.; 1992:2–38.
4. Alagusundaram M, Sudana CM, Umashankari K, Badarinath AV, Lavanya C, Annamacharya RS. Microbeads as a novel drug delivery system: A review. *Int J Chemtech Res*. 2009;1(3):526–534.
5. Bhandari N, Pooni N, Verma P, Gupta R. Microspheres as a novel drug delivery system: A review. *Int J Pharm Res Bios*. 2014;3(14):489–506.
6. Devrim B, Canefe K. Preparation and evaluation of modified release ibuprofen microspheres with acrylic polymers (eudragit) by quasi emulsion solvent diffusion method: Effect of variables. *Acta Pol Pharm*. 2006;63(6):521–534.
7. Bose U, Gunasekaran K, Bala V, Rahman AA. Evaluation of phytochemical and pharmacological properties of *Dillenia indica* Linn. leaves. *J Pharmacol Toxicol*. 2010;5(5):222–228.
8. Pradhan BK, Badola HK. Ethnomedicinal plant use by Lepcha tribe of Dzongu valley, bordering Khangchendzonga Biosphere Reserve, in North Sikkim, India. *J Ethnobiol Ethnomed*. 2008:4(22):32–37.
9. Singh DR, Singh S, Salim KM, Srivastava RC. Estimation of phytochemicals and antioxidant activity of underutilized fruits of Andaman Islands (India). *Int J Food Sci Nutr*. 2012;63(4):446–452.
10. Sekar N, Sukumar R, Leishman M. Waiting for Gajahlan elephant mutualist's contingency plan for an endangered megafaunal disperser. *J Ecol*. 2013;101(6):1379–1388.
11. Chamba MB. Studies on the production and evaluation of starch from yam (Dioscorea spp.) and Cocoyam (*Colocasia esculenta*) tubers cultivated in Nigeria. *EC Nutrition*. 2016;3(2):572–588.
12. Food and Agriculture Organization of the United Nations (FAO). FAOSTAT Statistics Database – Agriculture. Rome, Italy: FAO; 2003. www.fao.org/statistics. http://www.fao.org/statistics/en/. Accessed on November 2019.
13. Akin-Ajani OD, Ajala TO, Okoli UM, Okonta O. Development of directly compressible excipients from *Phoenix dactylifera* (Date) mucilage and microcrystalline cellulose using co-processing techniques. *Acta Pharm. Sci*. 2018;56(3):3–12. doi:10.23893/1307-2080. APS.0561
14. Association of Official Analytical Chemists (AOAC). *Official Methods of Analysis of Association of Official Analytical Chemists*. 15th ed. Arlington, VA: AOAC; 2000.
15. Odeku OA, Aderogba, AA, Ajala TO, Akin-Ajani OD, Okunlola A. Formulation of floating metronidazole microspheres using cassava starch (*Manihot esculenta)* as polymer. *J Pharm Investig*. 2017;47(5):445–451.
16. Singhvi G, Singh M. Review: In-vitro drug release characterization models. *Int J Pharm Stud Res*. 2011;2:77–84.
17. Dash S, Murthy PN, Nath L, Chowdhury P. Kinetic modeling on drug release from controlled drug delivery systems. *Acta Pol Pharm*. 2010;67(3):217–223.
18. Fu Y, Kao WJ. Drug release kinetics and transport mechanisms of non-degradable and degradable polymeric delivery systems. *Expert Opin Drug Deliv*. 2010;7(4):429–444.
19. Siepmann J, Peppas NA. Modeling of drug release from delivery systems based on hydroxypropyl methylcellulose (HPMC). *Adv Drug Deliv Rev*. 2001;48(2–3):139–157.
20. Adebowale AA, Adegoke MT, Sanni SA, Adegunwa MO, Fetuga OA. Functional properties and biscuit-making potentials of sorghum wheat-flour composite. *Amer J Food Technol*. 2012;7(6):372–379.
21. Williams PA, Phillips GO, eds. *Gums and Stabilizers for the Food Industry*. 12th ed. Cambridge, UK: Royal Society of Chemistry; 2004. ISBN 0-85404-891-X.
22. Akin-Ajani OD, Ajala TO, Ikehin M. Date mucilage as co-polymer in metformin-loaded microbeads for controlled release. *J Excipients Food Chem*. 2019;10(1):3–12.
23. Prasanth VV, Akash CM, Sam TM, Rinku M. Microspheres: An overview. *Intern J Pharm Biomed Scs*. 2011;2(2):332–338.
24. Poovi G, Arul J, Deepa J, Lakshmi S, Arun D. Review on microspheres. *Amer J Drug Discov Dev*. 2014;4:153–179.
25. Huynh CT, Lee DS. Controlled release. In: Kobayashi S, Müllen K, eds. *Encyclopedia of Polymeric Nanomaterials*. Berlin-Heidelberg, Germany: Springer Verlag; 2014. doi:10.1007/978-3-642-36199-9_314-1
26. Odeku OA, Lamprecht A, Okunlola A. Characterization and evaluation of four natural gums as polymers in formulations of diclofenac sodium microbeads. *Int J Biol Macromol*. 2013;58:113–120.

Evaluation of starch-clay composites as a pharmaceutical excipient in tramadol tablet formulations

Cecilia O. Alabi[1,B–D], Inderbir Singh[2,A,C,D], Oluwatoyin Adepeju Odeku[1,A,C–F]

[1] Department of Pharmaceutics and Industrial Pharmacy, University of Ibadan, Nigeria

[2] Chitkara College of Pharmacy, Chitkara University, Patiala, India

A – research concept and design; B – collection and/or assembly of data; C – data analysis and interpretation;
D – writing the article; E – critical revision of the article; F – final approval of the article

Address for correspondence
Oluwatoyin Adepeju Odeku
E-mail: pejuodeku@yahoo.com

Abstract

Background. Co-processing starch with clay nanocomposite has been shown to yield a new class of materials, potentially with better properties than pristine starch, that could be used as directly compressible excipients in tablet formulations.

Objectives. In this study, starches from 3 botanical sources, i.e., millet starch from *Pennistum glaucum* (L) RBr grains, sorghum starch from *Sorghum bicolor* L. Moench grains and cocoyam starch from *Colocasia esculenta* L. Schott tubers, were co-processed with montmorillonite clay (MMT) and evaluated as a directly compressible excipient in tramadol tablet formulations. The effects of different starch-to-clay ratios on the material and drug release properties of the resulting tablets were evaluated.

Material and methods. The starch-clay composites were prepared by heating a dispersion of the starch in distilled water, then precipitating the dispersion with an equal volume of 95% ethanol. The starch-clay composites were characterized and used as direct compression excipients for the preparation of tramadol tablets. The mechanical and drug release properties of the tablets were evaluated.

Results. Co-processing MMT with the starches yielded starch-clay composites with different material and tablet properties than the pristine starches. The co-processed starch-MMT biocomposites exhibited improved flowability and compressibility over the pristine starches. The mechanical and drug release properties of tramadol tablets containing starch-clay composites were significantly better than those containing only pristine starches. The properties of the starch-clay composites were not related to the botanical source of the starches.

Conclusions. The study showed that starch-clay biocomposites could be used in the controlled release of tramadol.

Key words: starch, tablets, excipients, biocomposite, dissolution test

Introduction

In recent years, polymer-clay nanocomposites have received more attention due to their enhanced physico-chemical and mechanical properties over the pure polymer systems.[1–4] Biological nanocomposites have become a valuable addition to the existing nanocomposite materials that can be used to substitute petroleum-based composite materials in various applications due to their inherent biodegradability, availability and cost-effectiveness.[4] Biopolymer-clay nanocomposites are prepared by adding low amounts of clay to the biopolymer matrix.[5]

Starch is one of the most abundant natural polymers that has become highly valuable due to its physical and chemical properties. However, native starch has poor compaction properties that have limited its application as a directly compressible excipient in tablet formulation.[6,7] Co-processing starch with a clay nanocomposite has been shown to yield a new class of materials with the potential for more beneficial mechanical properties than the pristine material.[8,9] The synergistic effect of starch and clay and the strong interfacial interactions (e.g., electrostatic and hydrogen bonding interaction) between the particles could improve the mechanical, swelling, water-uptake, thermal, drug-loading efficiency, and controlled-release behavior of the pristine biopolymer matrices.[8] Montmorillonite (MMT) is one of the most commonly used natural clays that has been successfully applied in the preparation of nanocomposite systems.[10–14] Montmorillonite is an aluminosilicate clay composed of tetrahedral layers of silica stacked between the octahedral layers of alumina.[15] The isomorphic substitution of Al^{3+} for Si^{4+} in the tetrahedral layer and Mg^{2+} for Al^{3+} in the octahedral layer results in a net negative surface charge on the clay. Montmorillonite has a large specific surface area, and exhibits good adsorption, cation exchange and drug loading capacity.[16] The individual crystals of MMT clay are not tightly bound, so water can infiltrate, causing the clay to swell and increase in volume when it absorbs water.[4] Starch-MMT composite films have been shown to possess higher tensile strength and better water vapor barrier properties than films from pristine starch, due to the formation of an intercalated nanostructure.[8]

Recent studies have shown the potential of starches from different botanical sources to serve as excipients in tablet formulations.[7,17,18] Native starches from millet (*Pennistum glaucum* (L) R Br, family *Poaceae*), sorghum (*Sorghum bicolor* L. Moench, family *Gramineae*) and cocoyam (*Colocasia esculenta* (L.) Schott, family *Araceae*) have been characterized and used as direct compression excipients in tramadol tablet formulations.[19] One study revealed that the natural starches exhibited poor flowability and compressibility, which was not suitable for the preparation of tablets through direct compression. Therefore, in this study, millet, sorghum and cocoyam starches have been co-processed with MMT and evaluated as a directly compressible excipient for the formulation of tramadol tablets for controlled drug delivery to provide consistent pain control with reduced dosage frequency and improved patient compliance.[20] The effect of different starch-to-clay ratios on the material and drug release properties were also evaluated.

Material and methods

Material

The materials used were tramadol hydrochloride (Banson Pharmaceuticals, Patiala, India), MMT (Sigma-Aldrich, St. Louis, USA), dicalcium phosphate, polyvinylpyrrolidone (K 30), talc, and magnesium stearate (all from Ipza Pharmaceuticals, Patiala, India). Grains of millet (*Pennisetum glaucum*) and sorghum (*Sorghum bicolor*), and tubers of cocoyam (*Colocasia esculenta*) were obtained from local farmers in Ibadan, Nigeria. The plant parts were authenticated and starches were extracted from the relevant plant parts using established procedures.[21] All other reagents used in the trials were of analytical grade.

Methods

Preparation of starch-clay composites

Starch-clay composites containing millet/sorghum/cocoyam starch and MMT in ratios of 1:0.5, 1:1, 1:2.5, and 1:5 were prepared by heating a dispersion of the starch in distilled water for 45 min on a hot plate and adding MMT. The dispersion was left on the hot plate (100°C) with constant heating and stirring for 4 h. The starch-clay mixture was allowed to cool to room temperature and was precipitated with an equal volume of 95% ethanol and stored at 4°C overnight. The precipitate was filtered and dried in a hot air oven at 100°C for 5 h. The starch-clay composite was powdered using a laboratory mill and passed through a 60-mesh sieve, and then stored in an airtight container.

Characterization of starch-clay composites

Scanning electron microscopy

The surface morphology of the starch-clays composites was determined using a scanning electron microscope (SEM; Hitachi Model S 4300 SE/N SEM; Hitachi High Technologies, Singapore) at an accelerator potential of 10 kV. The samples were stuck on a specimen holder using a silver plate and then coated with palladium in a vacuum evaporator.

pH level

The pH of a 1% w/v water dispersion of the starch-clay composites was determined using a digital pH meter at 37 ±2°C.

Loss on drying

The starch-clay composites were weighed (W_1) and heated in an oven at 100 ±5°C until a constant weight was achieved. The samples were cooled in a desiccator and then reweighed (W_2). The percentage loss on drying (% LOD) was calculated using the following formula:

$$LOD = \left[W_1 - \frac{W_2}{W_1} \right] \times 100 \qquad (1)$$

Effective pore radius

The effective pore radius was determined using the method of Goel et al.[22] In brief, a micropipette tip (2 mL, transparent) was filled with a starch-clay composite and weighed (W_1). N-hexane, whose surface tension (γ) is 18.4 mN/m, was poured dropwise on the bed top until the solvent filtered out at the bottom of the tip. The tip was reweighed (W_f) and the effective pore radius was calculated using the following equation:

$$R_{eff.P} = \frac{W_f - W_i}{2\pi\gamma} \qquad (2)$$

Swelling index

The initial bulk volume of the starch-clay composite in a 100-milliliter stoppered, graduated cylinder was determined. Water was then added in a sufficient quantity to produce a uniform dispersion. The sediment volume of the swollen mass was measured after 24 h. The swelling index was calculated as:

$$SwellingIndex = \left[\frac{V_2 - V_1}{V_1} \right] \times 100 \qquad (3)$$

where V_1 and V_2 are the volumes of the starch-clay composite before and after hydration, respectively.

Bulk and tapped density

The bulk density and tapped bulk density of the starch-clay composite was determined in a 250-milliliter measuring cylinder using an automated volumeter (Vardhan Works Pvt. Ltd, Pune, India). Measurements were made in triplicate according to the *European Pharmacopeia*.[23]

Flowability

The Hausner ratio and Carr index were used to determine the flowability of the starch-clay composites.[24] The flow rate of the starch-clay composites was determined using a steel funnel on a Pharmatest flow rate apparatus (Sartorius Pharmatest; Apparatebau GmbH, Hainburg, Germany) with an orifice of 15 mm.

Attenuated total reflectance-Fourier transform infrared spectroscopy

The starch-clay composites were analyzed using an attenuated total reflectance-Fourier transform infrared spectroscopy (ATR-FTIR) spectrophotometer (Alpha; Bruker, Yokohama, Japan). The samples were scanned in the spectral region from 4,000 cm^{-1} to 400 cm^{-1} using the KBr pellet method.

Formulation of tramadol hydrochloride tablets

Tramadol hydrochloride tablets were formulated with the direct compression method according to the formulae provided in Table 1. Batches (100 g) of each formulation were prepared by mixing the specified quantity of each ingredient in a tumble mixer for 15 min. The blend was lubricated with talc and magnesium stearate, and the mixing was done for an additional 5 min. The tramadol tablets were compressed using a multi-punch tableting machine (AK Industries, Nakodar, India) fitted with 6.75-millimeter biconcave round die punches.

Table 1. Composition of tramadol tablets

Ingredients	Weight per tablet [mg]
Tramadol	100
Starch-clay composite	120
Polyvinylpyrrolidone (K 30)	25
Talc	2.5
Magnesium stearate	2.5
Total	250

Tablet properties

Crushing strength

The crushing strength of the tablets was determined using a hardness tester (Perfit, Coimbatore, India). The force required to break a tablet was determined diametrically, and the averages for 6 tablets were calculated.

Friability

The friability of the tablets was measured using a friabilator (Model 902; EI Product, Panchkula, India). Twenty tablets were weighed and rotated at 25 rpm for 4 min. The tablets were reweighed after the removal of fines, and the percentage of weight loss was calculated.

Disintegration time

The disintegration time of the tablets was determined using a United States Pharmacopeia (USP) disintegration apparatus (EI Product) in 900 mL of 0.1 N HCl (pH 1.2, 37°C).

In vitro dissolution studies

The in vitro dissolution time of the tramadol tablets was determined in 900 mL of 0.1 N HCl (pH 1.2) at 37 ±0.5°C using a USP XXIV dissolution apparatus II (DS 8000; Lab India, Pune, India) with a paddle stirring rate of 50 rpm. Aliquots (5 mL) were withdrawn at predetermined intervals and replaced with an equal volume of fresh medium. The samples were filtered through a 0.45-micrometer membrane filter and analyzed for drug content using

a double beam ultraviolet–visible (UV/VIS) spectrophotometer (Model 2202; Systronics, Ahmedabad, India) at 272 nm. The drug concentration was calculated and expressed as a cumulative percent of the drug released.

Statistical analysis

Statistical analysis was carried out using analysis of variance (ANOVA) with GraphPad Prism® v. 4 computer software (GraphPad Software Inc. San Diego, USA). Tukey–Kramer multiple comparison tests were conducted to compare the effects of the excipients on the mechanical and drug release properties of the tablets. At a 95% confidence interval (95% CI), p-values less than or equal to 0.05 were considered significant.

Results and discussion

Characterization of starch-clay composites

The SEM image of the starch-clay composite shown in Fig. 1 indicates irregularly shaped particles which differed from the granular-shaped ones reported for the native starches.[19] Studies have reported that 2 types of hybrids are formed in starch-MMT composites: intercalated hybrids and exfoliated hybrids.[25] In intercalated hybrids, the extended polymer chains are present between the clay layers, resulting in a multilayered structure with polymer/inorganic layers at a repeated distance of a few nanometers. In exfoliated hybrids, the silicate layers are completely separated and dispersed in a continuous polymer
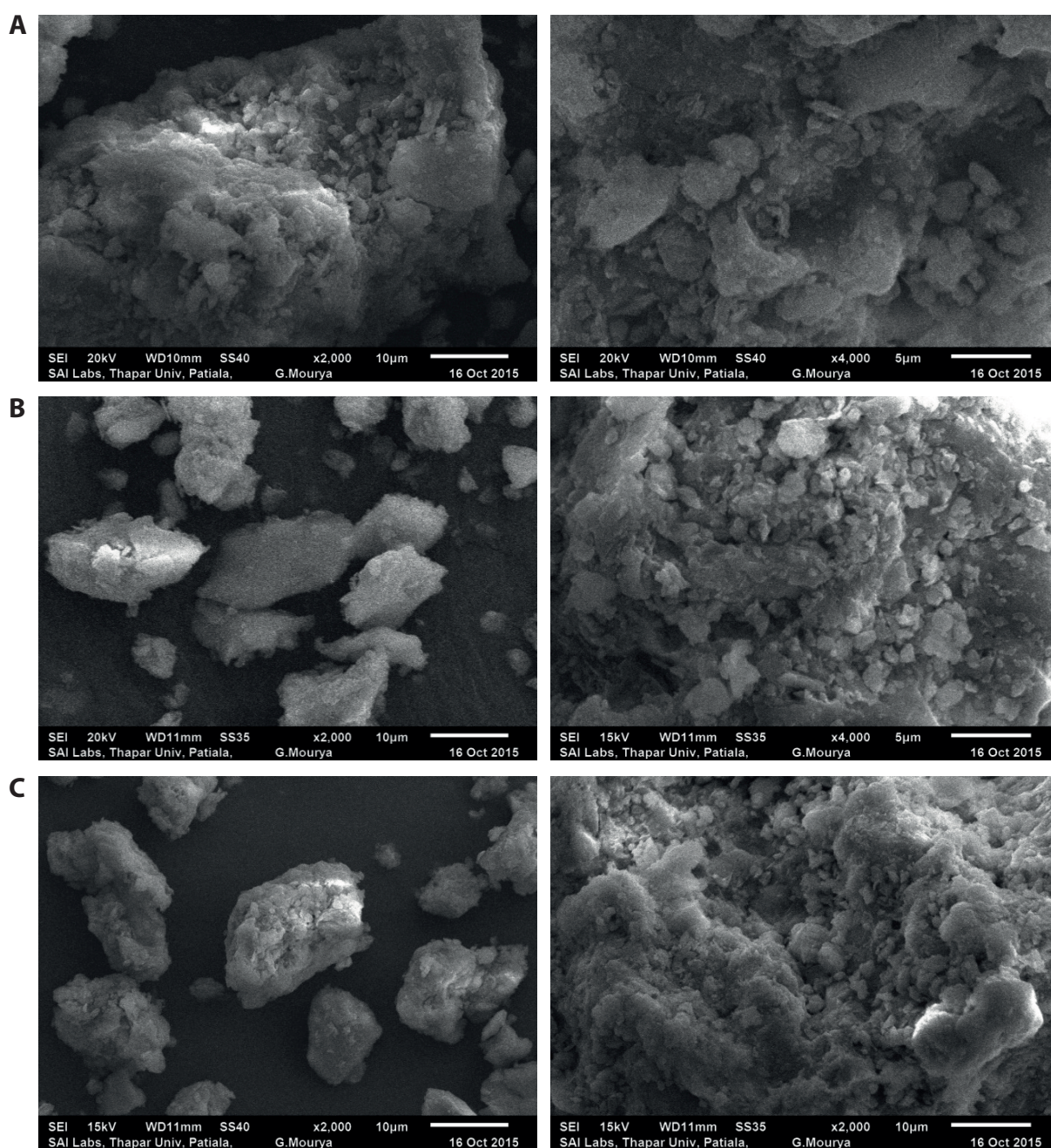

Fig. 1. SEM images of starch-montmorillonite clay composite (1:1) at different magnifications: (A) millet, (B) sorghum and (C) cocoyam

Table 2. Material properties of the pristine starches and starch-clay composites

Parameter material	Starch-clay composite	pH	Loss on drying [%]	Effective pore radius	Swelling index [%]	Bulk density [g/cm³]	Tapped density [g/cm³]	Carr index [%]	Hausner ratio
Millet	1:0	6.0 ±0.0	4.06 ±0.20	1.62 ±0.22	11.0 ±0.0	0.215 ±0.002	0.380 ±0.001	43.42 ±0.02	1.76
	1:0.5	5.6 ±0.1	4.07 ±0.01	2.36 ±0.05	56.2 ±0.2	0.559 ±0.012	0.718 ±0.005	22.15 ±0.03	1.28
	1:1	5.2 ±0.2	4.07 ±0.03	2.42 ±0.07	20.1 ±0.2	0.559 ±0.000	0.685 ±0.003	18.42 ±0.01	0.96
	1:2.5	4.7 ±0.0	4.07 ±0.03	2.14 ±0.03	9.1 ±0.0	0.420 ±0.011	0.580 ±0.002	27.54 ±0.02	0.85
	1:5	4.4 ±0.1	3.85 ±0.02	2.18 ±0.02	1.3 ±0.1	0.419 ±0.002	0.559 ±0.000	25.03 ±0.00	0.96
Sorghum	1:0	6.0 ±0.1	4.07 ±0.02	2.09 ±0.02	17.1 ±0.3	0.268 ±0.001	0.439 ±0.002	38.95 ±0.00	1.64
	1:0.5	8.3 ±0.1	8.02 ±0.22	2.39 ±0.03	367.3 ±0.2	0.514 ±0.002	0.665 ±0.011	22.72 ±0.01	1.29
	1:1	7.4 ±0.0	7.98 ±0.02	2.31 ±0.04	100.4 ±0.0	0.471 ±0.009	0.628 ±0.015	24.99 ±0.02	1.33
	1:2.5	6.0 ±0.0	7.96 ±0.14	2.10 ±0.09	17.2 ±0.2	0.377 ±0.003	0.595 ±0.003	36.66 ±0.01	1.58
	1:5	5.4 ±0.1	7.02 ±0.04	2.09 ±0.22	3.3 ±0.5	0.353 ±0.002	0.565 ±0.000	37.47 ±0.02	1.60
Cocoyam	1:0	6.8 ±0.1	4.07 ±0.03	2.09 ±0.02	17.2 ±0.2	0.317 ±0.022	0.513 ±0.004	38.21 ±0.01	1.62
	1:0.5	7.4 ±0.0	6.01 ±0.01	2.35 ±0.01	220.0 ±0.2	0.580 ±0.001	0.685 ±0.004	15.40 ±0.02	1.18
	1:1	7.7 ±0.0	6.00 ±0.02	2.27 ±0.01	56.1 ±0.1	0.538 ±0.004	0.628 ±0.003	14.28 ±0.02	1.17
	1:2.5	7.8 ±0.0	5.33 ±0.15	2.15 ±0.06	9.1 ±0.0	0.397 ±0.021	0.580 ±0.008	31.58 ±0.03	1.46
	1:5	7.9 ±0.0	5.70 ±0.03	2.06 ±0.03	4.3 ±0.2	0.377 ±0.002	0.538 ±0.002	29.99 ±0.00	1.43
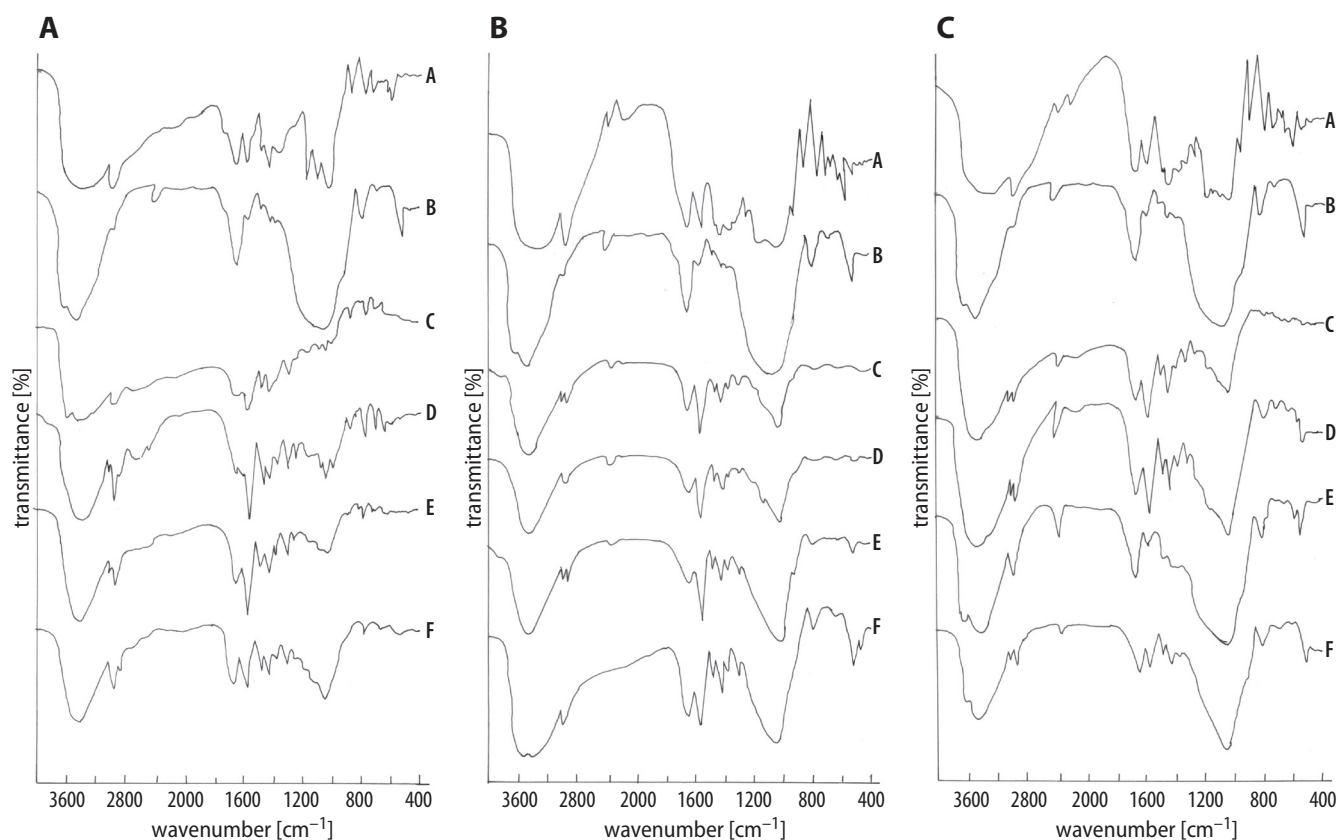
Fig. 2. FTIR spectra of (A) millet, (B) sorghum and (C) cocoyam pristine starch and starch-clay composites: native starch (A), montmorillonite clay (B), 1:0.5 starch-clay composite (C), 1:1 starch-clay composite (D), 1:2.5 starch-clay composite (E), and 1:5 starch-clay composite (F)

matrix.[26] The SEM suggests that exfoliated hybrids were formed with the clay completely dispersed in the starch matrix for a hybrid with completely different properties from the pristine starch.

The results of the physicochemical and material properties of the starch-clay composites presented in Table 2 indicate that the biocomposites varied widely in their properties. The pH of the biocomposites ranged from 5.2

to 8.3. The pH values generally decreased as the concentration of MMT in the biocomposite increased, except for the biocomposite containing cocoyam starch, where the pH increased. This indicates that the co-processing of millet and sorghum starches with MMT resulted in a more acidic biocomposite, while co-processing with cocoyam resulted in a more neutral pH. The loss on drying is used to evaluate the moisture content of pharmaceutical powders; the percentage loss on drying decreased with the concentration of MMT in the biocomposite. The maximum moisture content prescribed for safe storage by most starch-producing countries is 13% w/w, since higher levels of water can lead to microbial spoilage and subsequent deterioration in starch quality.[27] The moisture content of all the biocomposites was within the specified limits for the proper storage of excipients. The pristine starches contain similar moisture content, while the biocomposites showed significantly higher (p < 0.05) moisture content than the pristine starches, except for the millet-MMT biocomposite, which did not demonstrate a significant increase in moisture content with an increase in MMT content.

The effective pore radius ranged from 1.62 to 2.42, with the values decreasing as the concentration of MMT in the composite increased, although there were no significant (p > 0.05) differences between the values. On the other hand, the swelling index of the starch-MMT composite at ratios of 1:0.5 and 1:1 were significantly (p < 0.001) higher than those of the pristine starch, while at a starch-to-MMT ratio of 1:2.5 or 1:5, the values were statistically significant (p < 0.05). There appears to be a limit to the concentration of MMT in the biocomposite mixture that would increase the swelling index of the composite. The degree of swelling also depended on the swelling index of the pristine starch, ranked as sorghum > cocoyam > millet. The starch-clay composites exhibited more wicking action than the pristine starches. Swelling power is not only a measure of the hydration capacity of a material, but it is also indicative of the associative forces in the granules.[28]

The bulk and tapped densities of the starch-clay composites were higher than those of the pristine starch, but they decreased with an increase in the concentration of MMT in the biocomposites. The Carr index values and Hausner ratios generally decreased with an increase in the concentration MMT in the biocomposites. This indicates that the biocomposite exhibited better flowability and compressibility than the pristine starches. However, all the biocomposites showed Carr indices greater than 21 except the cocoyam-MMT biocomposite at ratios of 1:0.5 and 1:1. This indicates that co-processing starch with MMT improves the flowability and compressibility of starches, although the starch-clay composite cannot be said to be free-flowing.

The FTIR-ATR spectroscopy was used to analyze the interaction between the starches and MMT. Representative
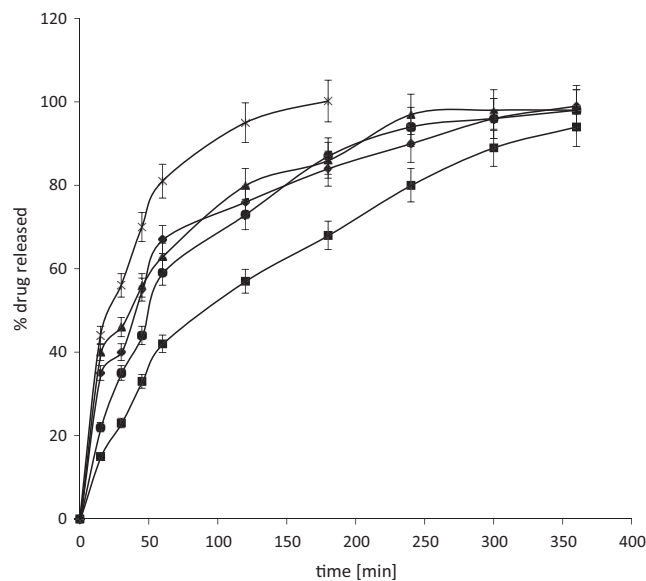

Fig. 3. Drug release profile of tramadol tablets containing native millet starch (✳) and millet starch-clay composites at ratios of 1:0.5 (■), 1:1(●),1:2.5 (◆), and 1:5 (▲)

spectra for millet (Fig. 3) indicate that the pristine starch exhibited a broad band at 3600–3200 cm due to OH groups in the starch molecules, C–H stretching at 2925 cm^{-1}, C=O stretching at 1640 cm^{-1}, CH$_2$ symmetrical stretching vibration observed at 1370 cm^{-1}, and C–C, C–O, C–O–C, and C–O–H stretching from 1350 cm^{-1} to 850 cm^{-1}. The peak at 897 cm^{-1} represents the saccharide group of the starch. On the other hand, the peak at 3619 cm^{-1} corresponds to the OH stretching vibration in MMT, the H–O–H bending of H$_2$O is indicated by the peak at 1633 cm^{-1}, and the peak at 1134 cm^{-1} indicates the Si–O stretching vibrations, while the peak at 520 cm^{-1} indicates Si–O bending. The peak at 919 cm^{-1} corresponds to Al–O vibrations.[9] The peaks around 3413 cm^{-1}, 1650 cm^{-1} and 1081 cm^{-1} show that the band of the starch overlapped with the bands of silicate, while at 1647 cm^{-1} the vibration band of silicate is unaffected. The soluble parts of the biopolymer containing OH and NH$_3$ may form a hydrogen bond with MMT and the amide group of starch visible in the range of 1200–850 cm^{-1} is due to the MMT. The vibration band at 1599 cm^{-1} corresponds to the deformation vibration of the protonated amine group in the biocomposite; this group is shifted towards the lower frequency value of 1517 cm^{-1} in the biocomposite, which further indicates electrostatic interaction between such groups and the negatively charged sites in the clay structure. The intensity of these peaks varied largely due to the concentration of MMT in the composite.

Tablet properties

The crushing strength (CS) and friability (F) provide measures of tablet strength and weakness, respectively,[29] and are a measure of the ability of tablets to withstand

Table 3. Tablet properties of the pristine starches and starch-clay composites

Parameter Material	Starch-clay composite	Hardness [kg/cm²]	Friability [%]	CSFR	Disintegration [min]	CSFR/DT	t_{50}	t_{80}
Millet	1:0	3.3 ±0.0	0.48 ±0.02	6.88	16.50 ±1.02	0.42	20.0 ±2.0	57.0 ±0.5
	1:0.5	3.5 ±0.0	0.49 ±0.01	7.14	29.70 ±2.00	0.24	50.0 ±0.0	240.0 ±3.0
	1:1	5.5 ±0.1	0.26 ±0.04	21.15	44.18 ±1.80	0.48	90.5 ±2.5	147.0 ±1.0
	1:2.5	5.0 ±0.1	0.38 ±0.02	13.16	25.53 ±1.92	0.52	40.5 ±1.0	146.0 ±0.0
	1:5	4.5 ±0.0	0.37 ±0.01	12.16	42.37 ±1.12	0.29	36.6 ±2.0	120.0 ±2.0
Sorghum	1:0	3.0 ±0.1	0.03 ±0.00	100.00	16.6 ±1.02	6.02	16.0 ±1.0	70.0 ±2.0
	1:0.5	4.5 ±0.1	0.15 ±0.01	30.00	27.03 ±1.15	1.11	26.5 ±2.0	76.5 ±3.0
	1:1	3.8 ±0.2	0.27 ±0.01	14.07	26.63 ±1.22	0.53	46.5 ±2.0	192.5 ±1.0
	1:2.5	4.3 ±0.0	0.33 ±0.03	13.03	30.48 ±1.12	0.43	48.5 ±1.5	260.0 ±2.0
	1:5	5.5 ±0.1	0.54 ±0.01	10.19	43.30 ±1.02	0.24	40.5 ±2.0	147.0 ±4.0
Cocoyam	1:0	3.3 ±0.1	0.12 ±0.01	27.50	19.0 ±2.01	1.45	32.0 ±1.5	110.0 ±2.0
	1:0.5	5.5 ±0.0	0.26 ±0.02	21.15	31.92 ±1.23	0.66	52.3 ±1.0	215.0 ±1.0
	1:1	7.0 ±0.1	0.37 ±0.01	18.92	26.02 ±0.92	0.73	50.1 ±3.0	135.0 ±2.5
	1:2.5	5.0 ±0.3	0.38 ±0.02	13.16	18.80 ±1.62	0.70	39.5 ±2.0	125.6 ±2.0
	1:5	5.5 ±0.0	0.51 ±0.01	10.78	16.65 ±1.96	0.65	26.4 ±1.0	170.0 ±1.0

CSFR – crushing strength-to-friability ratio; CSFR/DT – crushing strength-to-friability-to-disintegration ratio.

pressure or stress during handling, packaging, transportation, and subsequent use. The results (Table 3) showed that tablets prepared with starch-clay composites generally exhibited higher crushing strength and friability than those prepared with pristine starches. The nature of the starch used for the starch-clay composite did not have a statistically significant effect ($p > 0.05$) on the mechanical properties of the tablets. All of the tramadol tablets exhibited friability values of less than 1% w/w, which is within the pharmacopeia standards for compressed tablets. The CS-to-F ratio (CSFR) was used as a measure of the mechanical strength of the pharmaceutical tablets: the higher the CSFR, the stronger the tablet.[29] The values of CSFR for the tramadol tablets indicates that the CSFR for tramadol tablets containing the pristine starches was generally higher than those of the starch-clay composites. This indicates that tablets made from the pristine starches exhibited more mechanical strength than those containing the starch-clay composites. The biocomposites containing sorghum starch exhibited the highest mechanical strength, while those containing millet starch exhibited the lowest values. Studies have shown that biocomposites can be considered a brittle or ductile material when the composite breaks with or without significant deformation under stress.[3] Biocomposites that are brittle tend to break when subjected to stress without significant strain, but ductile composites deform before complete failure and tend to absorb energy before fracture. Thus, the biocomposites appeared more brittle than the pristine starches.

The disintegration time (DT) is regarded as the time required for the tablet to break into particles before dissolution occurs. The disintegration times for tra-

madol tablets containing the starch-clay composite are significantly ($p < 0.05$) higher than those containing the pristine starches except for cocoyam starch-clay composite at high-MMT ratios (ratios of 1:2.5 and 1:5), where the DT was lower. The strong interfacial interaction between the particles of the starch and clay yielded a starch-clay composite with a longer disintegration time. However, there is no clear-cut pattern regarding the effects of the clay concentration on the DT of the tablets. This suggests that the effect of the starch-MMT biocomposite is probably due to several interacting factors. The crushing strength-to-friability-to-disintegration ratio (CSFR/DT) was used to evaluate the balance between crushing strength and disintegration. A high CSFR/DT ratio indicates a better balance between the mechanical and disintegration properties of the tablets.[29] The results show that tramadol tablets containing pristine starch exhibited a better balance than those containing the starch-clay composite, with the balance decreasing as the concentration of MMT in the biocomposite increased.

The amount of tramadol released was plotted over time; representative plots for the tramadol tablets containing millet starch-clay composites are shown in Fig. 3. The time for 50% and 80% drug release (t_{50} and t_{80}, respectively) derived from the plots are shown in Table 3. The results showed that the dissolutions times t_{50} and t_{80} generally decreased with an increase in MMT concentration. The DTs for tablets containing the biocomposites were significantly ($p < 0.01$) higher than those containing the pristine starches. There appears to be no clear-cut pattern as to which starch will likely form a more rigid biocomposite that could yield a longer dissolution time.

Conclusions

The results indicate that the co-processing of MMT with the 3 tropical starches yielded starch-clay composites that differed from the pristine starches in both their material and tablet properties. Co-processing starches with MMT improved the flowability and compressibility of the native starches. The mechanical and drug release properties of the tramadol tablets containing the starch-clay composites were significantly better than those containing the pristine starches. There is no clear-cut pattern on the effects of the clay concentration or botanical properties of the starches. The starches from different botanical sources could be useful in the production of starch-clay composites for a variety of formulations depending on the mechanical and drug release profiles desired. The study showed that starch-clay biocomposites could be used in the controlled release of tramadol.

ORCID iDs

Cecilia O. Alabi https://orcid.org/0000-0002-6336-611X
Inderbir Singh https://orcid.org/0000-0002-1860-4246
Oluwatoyin Adepeju Odeku https://orcid.org/0000-0002-0732-1304

References

1. Bagdi K, Muller P, Pukanszky B. Thermoplastic starch/layered silicate composites: Structure, intercalation, properties. *Comp Interf*. 2006; 13(1):1–17.
2. Chiou BS, Yee E, Wood D, Shey J, Glenn G, Orts W. Effects of processing conditions on nanoclay dispersion in starch-clay nanocomposites. *Cereal Chem*. 2006;83(3):300–305.
3. Chung YL, Ansari S, Estevez L, Hayrapetyan S, Giannelis EP, Lai HM. Preparation and properties of biodegradable starch-clay nanocomposites. *Carbohyd Polym*. 2010;79:391–396.
4. Madhumitha G, Fowsiya J, Mohana RS, Thakur VK. Recent advances in starch-clay nanocomposites. *Inter J Polym Analy Charac*. 2018; 23(4):331–345.
5. Zhao R, Torley P, Halley PJ. Emerging biodegradable materials: Starch and protein-based bio-nanocomposites. *J Mater Sci*. 2008;43: 3058–3071.
6. Odeku OA, Picker-Freyer KM. Analysis of the material and tablet formation properties of four *Dioscorea* starches. *Starch/Stärke*. 2007; 59(9):430–444.
7. Odeku OA. Potentials of tropical starches as pharmaceutical excipients: A review. *Starch/Stärke*. 2013;65(1–2):89–106.
8. Tang X, Alavi S, Herald TJ. Barrier and mechanical properties of starch-clay nanocomposite films. *Cereal Chem*. 2008;85(3):433–439.
9. Thakur G, Singh A, Singh I. Formulation and evaluation of transdermal composite films of chitosan-montmorillonite for the delivery of curcumin. *Int J Pharm Investig*. 2016;6(1):23–31.
10. Giannelis EP. Polymer layered silicate nanocomposites. *Advan Mat*. 1996;8(1):29–35.
11. Paul DR, Robeson LM. Polymer nanotechnology: Nanocomposites. *Polymer*. 2008;49(15):3187–3204.
12. Pavlidou S, Papaspyrides CD. A review on polymer-layered silicate nanocomposites. *Prog Polym Sci*. 2008;33(12):1119–1198.
13. Raquez JM, Narayan R, Dubois P. Recent advances in reactive extrusion processing of biodegradable polymer-based compositions. *Macromol Mat Eng*. 2008;293:447–470.
14. Ray SS, Okamoto M. Polymer/layered silicate nanocomposites: A review from preparation to processing. *Prog Poly Sci*. 2003;28(11): 1539–1641.
15. Barton CD, Karathanasis AD. Clay minerals. In: *Encyclopedia of Soil Science*. New York, NY: Marcel Dekker Inc. US; 2007:187–190.
16. Yang H, Wang W, Zhang J, Wang A. Preparation, characterization, and drug-release behaviors of a pH-sensitive composite hydrogel bead based on guar gum, attapulgite, and sodium alginate. *Int J Polym Mater Polym Biomater*. 2012;62(7):369–376.
17. Odeku OA, Awe OO, Popoola B, Odeniyi MA, Itiola OA. Compression and mechanical properties of tablet formulations containing corn, sweet potato, and cocoyam starches as binders. *Pharm Tech*. 2005;29(4):82.
18. Dare K, Akin-Ajani DO, Odeku OA, Odusote OM, Itiola OA. Effects of pigeon pea and plantain starches on the compressional, mechanical and disintegration properties of paracetamol tablets. *Drug Dev Ind Pharm*. 2006;32(3):357–365.
19. Alabi CO, Singh I, Odeku OA. Evaluation of natural and pregelatinized forms of three tropical starches as excipients in tramadol tablet formulation. *J Pharm Investig*. 2018;48(3):333–340.
20. Kizilbash A, Ngô-Minh C. Review of extended-release formulations of tramadol for the management of chronic non-cancer pain: Focus on marketed formulations. *J Pain Res*. 2014;7:149–161.
21. Young AH, In: Whistler RL, BeMiller JN, Pashall EF, eds. *Starch Chemistry and Technology*. London, UK: Academic Press; 1984:183–184,249–283.
22. Goel H, Kaur G, Tiwary A. K, Rana A. Formulation development of stronger and quick disintegrating tablets: A crucial effect of chitin. *Yakugaku Zasshi*. 2010;130(5):729–735.
23. *European Pharmacopoeia: Directorate for the Quality of Medicines of the Council of Europe*. 5th ed. Strasbourg, France. 2007.
24. Carr RL. Evaluating flow properties of solids. *Chem Eng*. 1965;72: 163–168.
25. Müller CMO, Laurindo JB, Yamashita F. Composites of thermoplastic starch and nanoclays produced by extrusion and thermopressing. *Carbohyd Polym*. 2012;89(2):504–510.
26. Weiss J, Takhistov P, McClements J. Functional materials in food nanotechnology. *J Food Sci*. 2006;71(9):R107–R116.
27. Odeku OA, Schmid W, Picker-Freyer KM. Material and tablet properties of pregelatinized (thermally modified) *Dioscorea* starches. *Eur J Pharm Biopharm*. 2008;70(1):357–371.
28. Manek RV, Builders PF, Kolling WM, Emeje M, Kunle OO. Physicochemical and binder properties of starch obtained from *Cyperus esculentus*. *AAPS PharmSciTech*. 2012;13(2):379–388.
29. Odeku OA, Itiola OA. Evaluation of the effects of khaya gum on the mechanical and release properties of paracetamol tablets. *Drug Dev Ind Pharm*. 2003;29(3):311–320.

Preparation and characterization of poly(ethylene oxide)/zinc oxide nanofibrous scaffold for chronic wound healing applications

Hamed Nosrati[1,A–F], Mohammad Khodaei[2,A–C,E,F], Mehdi Banitalebi-Dehkordi[3,C,E,F], Morteza Alizadeh[1,B,C,F], Shiva Asadpour[1,3,F], Esmaeel Sharifi[4,A,F], Jafar Ai[5,A,C,E,F], Mostafa Soleimannejad[1,3,A–F]

[1] Department of Tissue Engineering and Applied Cell Sciences, School of Advanced Technologies, Shahrekord University of Medical Sciences, Shahrekord, Iran

[2] Department of Materials Science and Engineering, Golpayegan University of Technology, Golpayegan, Iran

[3] Cellular and Molecular Research Center, Basic Health Sciences Institute, Shahrekord University of Medical Sciences, Shahrekord, Iran

[4] Department of Tissue Engineering and Biomaterials, School of Advanced Medical Sciences and Technologies, Hamadan University of Medical Sciences, Hamadan, Iran

[5] Department of Tissue Engineering and Applied Cell Sciences, School of Advanced Technologies in Medicine, Tehran University of Medical Sciences, Tehran, Iran

A – research concept and design; B – collection and/or assembly of data; C – data analysis and interpretation;
D – writing the article; E – critical revision of the article; F – final approval of the article

Address for correspondence
Mostafa Soleimannejad
E-mail: soleimannejad@yahoo.com

Abstract

Background. Skin, the first barrier to pathogens, loses its integrity and function after an injury. The presence of an antibacterial dressing at the wound site may prevent bacterial invasion and also improve the healing process.

Objectives. The current study aimed to fabricate a biomimetic membrane with antibacterial properties for healing chronic wounds.

Material and methods. The membranes, fabricated through electrospinning, are comprised of poly(ethylene oxide) (PEO) and zinc oxide nanoparticles (ZnO-NPs) as the main biomaterial and antibacterial agent, respectively. Antibacterial activity, cell attachment and viability were tested to evaluate the biological properties of the membranes. The optimal cell compatible concentration of ZnO-NPs was determined for further studies. In vitro characterization of the membranes was performed to confirm their suitable properties for wound healing.

Results. The antibacterial PEO/ZnO-NP membrane containing 2% of nanoparticles showed no cell toxicity, and human fibroblast cells were able to adhere and proliferate on the scaffold. The in vitro results from the tensile test, wettability, porosity, and protein adsorption revealed appropriate properties of the membrane as a scaffold for skin tissue engineering.

Conclusions. Synthetic polymers have been widely used for tissue engineering applications. The proper characteristics of PEO nanofibers, including a high ratio of surface/volume, moderate hydrophilicity and good mechanical properties, make this polymer interesting for skin regeneration. The results demonstrate the potential of the antibacterial PEO/ZnO-NP membrane to be used as an engineered scaffold to improve the wound healing process.

Key words: zinc oxide, wound healing, antibacterial, electrospun membrane, poly(ethylene oxide)

Introduction

Skin, the largest and heaviest organ of mammals, provides a functional barrier to protect the human body from its surroundings. It protects the underlying tissues against microbial pathogens. As the primary barrier, it is exposed to harmful situations, such as chemical, mechanical and thermal influences, as well as microbial invasions.[1] Engineered scaffolds can encourage regeneration in cases of excessive skin loss due to severe dermal wounds. Significant effort has been made over the last decades to produce biomimetic substitutes.[2] Tissue engineering approaches are promising tools for creating scaffolds that could mimic the microstructure of the native tissue in order to regenerate it. In the field of skin tissue engineering, an ideal biomimetic scaffold/substitute should protect the injured area from infection and prevent fluid loss. The appropriate mechanical properties of these scaffold/substitute could also improve the wound healing process.[3]

Different synthetic and natural polymers are used to fabricate protective scaffolds for wound healing. (Hydro-)gels, membranes, films, as well as micro- and nanofibers are the most common scaffolds in skin tissue engineering.[4] Among skin substitutes, nanofibers have captured great attention for use as wound dressings and scaffolds. Nanofibers provide a topography similar to the native extracellular matrix (ECM) that encourages cell attachment, migration and differentiation.[5] High porosity, large surface area/volume ratio and suitable mechanical properties make nanofibers interesting for biomedical applications. Nanofibers can be fabricated with different methods and techniques such as self-assembly, drawing, phase separation, and electrospinning. The high surface area of electrospun fibers facilitates cell adhesion as well as gas exchange.[6]

Through the selection of biomaterial and optimization of electrospinning process, parameters such as flow rate, polymer solution concentration, solvent, distance, and voltage, a wide range of scaffolds that vary in morphology, fiber size and porosity can be obtained.[7] Most of the biomaterials used for skin tissue engineering have been natural-based biopolymers. Although these polymers induce cell adhesion well, they usually have poor mechanical properties; the electrospinning of these polymers is also challenging. To overcome such drawbacks, synthetic polymers such as poly(ethylene oxide) (PEO), polyvinyl alcohol (PVA) and poly(lactide-co-glycolide) (PLGA) have been blended with natural biopolymers to enable the production of nanofibrous scaffolds.[8,9]

Poly(ethylene oxide) is a synthetic polymer usually used as a second component to facilitate the electrospinning of other polymers such as silk fibroin, chitosan and collagen. Using this spinnable synthetic polymer singly could provide high mechanical properties and enhance cell adhesion. It can also limit the use of organic solvents to improve the biocompatibility of the fibers.[10]

Zinc oxide is a biologically safe material that has captured much attention due to its antibacterial properties. The nanosized forms of this material have a larger surface area, resulting in a greater impact. The presence of ZnO-NPs in nanofibers reportedly improves the antibacterial activity of fibrous membranes.[11,12]

In the present study, an antibacterial electrospun scaffold composed of PEO fibers and ZnO-NPs was prepared. In vitro characterization of the electrospun scaffold was performed to evaluate the biocompatibility and potential of the nanofibrous membrane to be used as an engineered scaffold for wound healing and skin tissue engineering applications. This is the first report of the preparation and in vitro characterization of PEO/ZnO-NP electrospun membranes for skin tissue engineering applications.

Material and methods

Solution preparation

Poly(ethylene oxide) solutions were prepared by dissolving PEO (Sigma-Aldrich, St. Louis, USA; CAS No. 25322-68-3) (average molecular weight: ~900,000) in 80% acetic acid (Sigma-Aldrich; CAS No. 64-19-7) at a concentration of 4% w/v. ZnO-NPs were purchased from US Research Nanomaterials (Houston, USA; Stock #US3590). Prior to loading, the size distribution and morphology of the ZnO-NPs were determined using dynamic light scattering (DLS) (Horiba Scientific SZ-100 Nanoparticle Analyzer; Horiba, Kyoto, Japan) and scanning electron microscopy (SEM) (S3400 Scanning Electron Microscope; Hitachi, Tokyo, Japan). After characterization of the nanoparticles, different concentrations of ZnO-NPs (0.5%, 1%, 2%, 3%, and 4% w/w) were added to the PEO solution while stirring.

Electrospinning process

Each sample was sonicated for 5 min and loaded in a 5-mL plastic syringe with an 18-gauge stainless steel needle. Fibers were collected on a rotating drum collector at a speed of 700 rpm. The PEO-ZnO solutions were electrospun on an electrospinning device (Model ANSTCO-N/VI; Asian NanoStructure Technology Company, Tehran, Iran) at a voltage of 22 kV, flow rate of 0.8 mL/h and needle-to-collector distance of 180 mm. The PEO solution was electrospun to produce PEO fiber as a control group.

Cross-linking of membranes

The electrospun membranes were dried for 48 h at room temperature and then cross-linked by exposure to glutaraldehyde (Grade I, 25% in H_2O; Sigma-Aldrich; CAS No. 111-30-8) vapor for 12 h. The cross-linked mats were heated at 80°C for 4 h to remove residual amounts of glutaraldehyde.

Biological properties of the electrospun membranes

Evaluation of antibacterial activity

The antibacterial activity of ZnO-NP-containing PEO scaffolds were studied against gram-negative (*Escherichia coli*) and gram-positive (*Staphylococcus aureus*) bacteria using the disc diffusion method.[13] A Mueller–Hinton (MH) agar plate was prepared by dissolving 38 g of MH (ibresco, Tehran, Iran; CAT No. i23118) powder in 1 L of distilled water heated with frequent agitation and boiled to completely dissolve the powder. The prepared liquid medium was sterilized at 120°C for 1 h in the autoclave. The medium was allowed to cool to room temperature and poured into sterilized 9-cm Petri dishes. After cooling overnight, the bacteria were swabbed across the culture dishes. The scaffolds were punched into discs with a diameter of 6 mm. The punched discs were placed on the surface of the culture medium. The Petri dishes were incubated at 37°C for 24 h. The effectiveness of the antibacterial components was determined by measuring the inhibition zone, i.e., the area around the disc where no colonies were formed. The diameters of the inhibition zones were measured using ImageJ Software v. 1.52v (National Institutes of Health, Bethesda, USA) and presented in millimeters.

Evaluation of cell viability

Adult human dermal fibroblasts were seeded on electrospun membranes with different concentrations of the ZnO-NPs (0%, 0.5%, 1%, 2%, 3%, and 4%). After sterilization with ethanol 70%, 5×10^3 cells were seeded on each sample in 96-well plates and incubated at 37°C with 94% humidity and 5% CO_2. Cell viability and proliferation were monitored at days 1, 3 and 7 using MTT assay. Dulbecco's modified Eagle's medium (DMEM) (Gibco, Waltham, USA; Mfr. No. Gibco™ 31600083) enriched with 10% of fetal bovine serum (FBS) (Gibco, Mfr. No. Gibco™ 10082139) and 1% penicillin/streptomycin (Gibco, Mfr. No. Gibco™ 15140122) was used as culture medium. At each time point, 20 μL of MTT solution (Sigma-Aldrich; CAS No. 298-93-1) was added to each well. Cell culture plates were incubated for 3 h; then, the media was replaced with 200 μL of dimethyl sulfoxide (DMSO) (Sigma-Aldrich; CAS No. 67-68-5), and the cultures were incubated for another 30 min.[14,15] Finally, the absorbance of each sample was determined using a BioTek 800™ TS Absorbance Reader (BioTek Instruments Inc., Winooski, USA) at 570 nm. Each sample was evaluated in triplicate.

Cell attachment and morphology

Following the determination of the optimal cell-compatible concentration of ZnO-NPs, adherence of human fibroblast cells to the membrane was observed using SEM.

Scaffolds were placed into 48-well plates, and 50×10^4 cells were seeded onto the membranes and cultured for 2 days. Membranes were washed 3 times with phosphate-buffered saline (PBS) (Merck Millipore, Burlington, USA; Millipore Sigma™ 65074L). Then, paraformaldehyde 4% (Thermo Fisher Scientific, Waltham, USA; MDL No. MFCD00133991) was added for 90 min. The samples were dehydrated in ascending concentrations of ethanol (60%, 70%, 80%, 90%, and 96%) for 10 min in each. Samples were sputtered with gold and studied using SEM.

Characterization of the electrospun membranes

SEM, FESEM and EDS analyses of the electrospun fibers

The morphology and size of PEO nanofibers were determined with the obtained SEM images. The average diameters of the fibers were determined by measuring random fibers selected from different fields. Field emission scanning electron microscopy (FESEM) and energy-dispersive X-ray spectroscopy (EDS) were performed to investigate the incorporation and dispersion of the ZnO-NPs.

ATR-FTIR analysis

To characterize the final composition of the nanofibrous scaffolds, attenuated total reflectance-Fourier transform infrared spectroscopy (ATR-FTIR) analyses were performed. The spectra were obtained using a Thermo Fisher Scientific iS10 FTIR spectrophotometer. The resolution and spectral range were 4 cm^{-1} and $4000–400 \text{ cm}^{-1}$, respectively.

Mechanical properties

The mechanical properties of the membranes were evaluated with tensile tests using a SANTAM testing machine (STM-5 Model; SANTAM Co. Ltd., Tehran, Iran). The tested membranes were 80×20 mm in size and had thicknesses of 0.45–0.59 mm. The testing speed was 1 mm/min for all samples. Stress-strain curves of the samples obtained from force-extension curves. The average for 5 samples (n = 5) was measured to determine the mechanical properties of each membrane.

Determination of porosity of the scaffolds

The porosity of the electrospun membranes was determined using a method described elsewhere.[16] In this method, dry weights of the scaffolds were recorded, and then the scaffolds were immersed in absolute ethanol for 1 h. Wet weights were also recorded. Three specimens were evaluated for each sample and the averages were reported. The porosity of each sample was determined through the following equation:

$$p\ (\%) = \frac{W_s - W_d}{D_{ethanol} - V_{scaffold}} \times 100$$

where (P – porosity, W_s – swollen scaffold weight, W_d – dry scaffold weight, $D_{ethanol}$ – ethanol density, $V_{scaffold}$ – volume of the swollen scaffold).

Wettability of membrane surface

The wettability of the scaffolds was determined by measuring the contact angle at the surface of the electrospun membranes. The water contact angles of 3 (n = 3) samples were measured using ImageJ software and the average was reported as the contact angle of each membrane.

Protein adsorption

Protein adsorption on membrane surfaces was assessed with a procedure described by Miguel et al.[8] The scaffolds were placed in a 48-well plate. Then, 300 μL of bovine serum albumin (BSA) (Sigma-Aldrich; CAS No. 9048-46-8) was added to the surface of the scaffolds, and they were incubated at 37°C for 0.5 h, 1 h, 2 h, 6 h, and 12 h. Phosphate-buffered saline was used to wash the non-adherent BSA, and then 300 μL of 2% sodium dodecyl sulfate (SDS) (Sigma-Aldrich; CAS No. 151-21-3) was added to each sample. After overnight incubation, a bicinchoninic acid (BCA) kit (DNAbiotech Co., Tehran, Iran; Cat No.: DB9684-50 mL) was used to investigate the protein absorption of the membranes.

Statistical analysis

One-way analysis of variance (ANOVA) with the Newman–Keuls post hoc test was performed to evaluate the results. Statistical comparisons between 2 groups were carried out using the t-test. A p-value lower than 0.05 was considered a significant change.

Results

Nanoparticles characterization

The results from DLS and SEM analyses revealed the size distribution, average size and morphology of the ZnO-NPs. As seen in Fig. 1, the average size of the ZnO-NPs was 74 nm and the size distribution was from 60 nm to 90 nm. The SEM image confirmed the nanosize of the particles. Nanoparticles in this range of size can easily be incorporated into electrospun fibers as other studies have reported.[17]

SEM, FESEM, and EDS analyses of electrospun fibers

The diameter of the fibers was determined with SEM analysis, as shown in Fig. 2. The images show randomly oriented electrospun PEO fibers with an average diameter of 362.5 nm. The PEO/ZnO-NPs fibers exhibit a similar morphology with a mean diameter of 315.3 nm
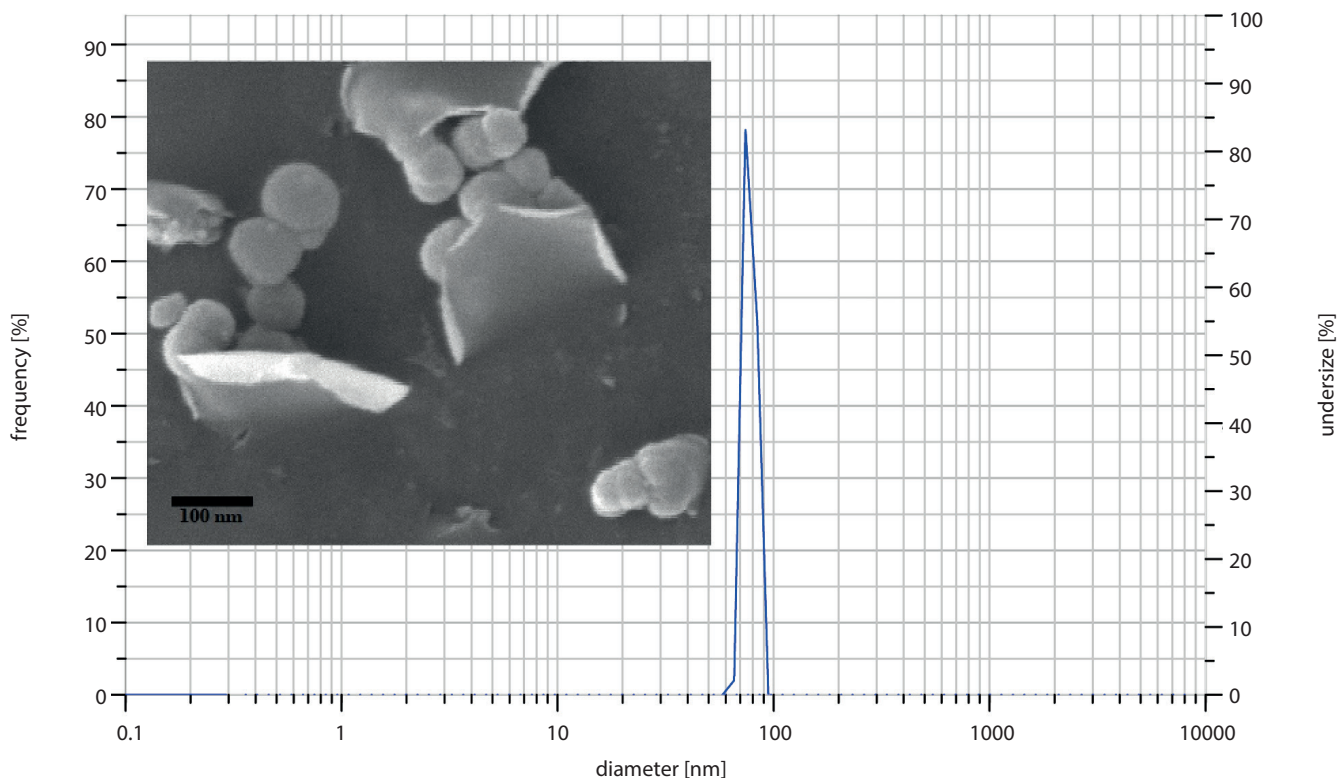

Fig. 1. SEM image and particle size distribution of zinc oxide nanoparticles measured using dynamic light scattering (DLS) method
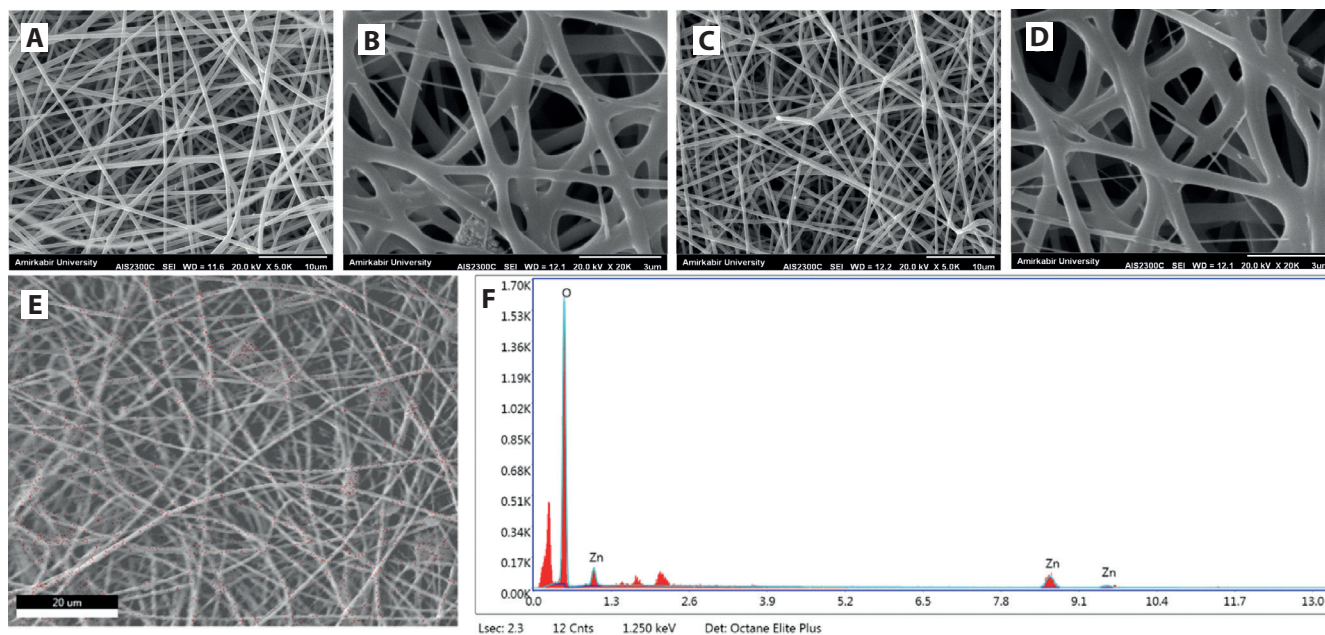
Fig. 2. SEM, FESEM and EDS analyses of the electrospun fibers. A. PEO fibers. B. Cross-linked PEO fibers. C. PEO/ZnO-NPs fibers. D. Cross-linked PEO/ZnO-NPs fibers. E. FESEM analysis of PEO/ZnO-NPs fibers. F. EDS analysis of PEO/ZnO-NPs fibers
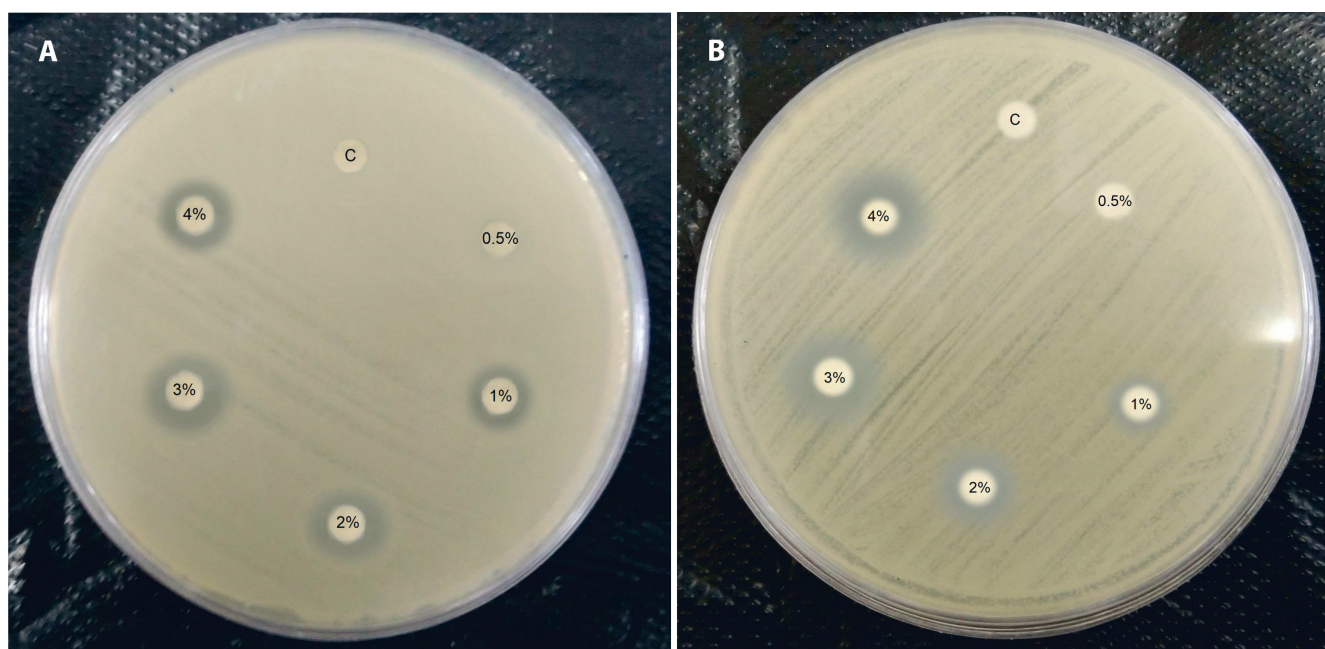

Fig. 3. Antibacterial activity of ZnO-NPs loaded into PEO fibers with different concentrations (0–4% w/w) against (A) *E. coli* and (B) *S. aureus*

(Fig. 2A,C). The images also confirmed the suitability of the crosslinking procedure (Fig. 2B,D). The FESEM image of ZnO-NP-loaded nanofibers demonstrated the proper ZnO-NP dispersion inside the PEO fibers (Fig. 2E). The EDS analysis of PEO/ZnO-NP fibers confirmed the presence of zinc and oxygen in the structure of the incorporated scaffold (Fig. 2F).

Biological properties of the electrospun membranes

Evaluation of antibacterial activity

Antibacterial properties were characterized with the disc diffusion method using gram-negative (*E. coli*) and gram-positive (*S. aureus*) bacteria.[18] The inhibition zones (Fig. 3) were measured and presented in Table 1.

Table 1. Effects of the incorporated ZnO-NPs on the antibacterial properties of the scaffolds

Scaffold type	PEO (control)	PEO/ZnO-NPs (0.5% ZnO-NPs)	PEO/ZnO-NPs (1% ZnO-NPs)	PEO/ZnO-NPs (2% ZnO-NPs)	PEO/ZnO-NPs (3% ZnO-NPs)	PEO/ZnO-NPs (4% ZnO-NPs)
Inhibition zone for *E. coli* [mm]	0	0.2	2.16	3.67	4.06	4.09
Inhibition zone for *S. aureus* [mm]	0	0	1.95	3.21	3.98	4.46

Evaluation of cell viability

The viability of human fibroblast cells was evaluated on day 1, 3 and 7 after cell seeding in the presence of scaffolds through the MTT assay (Fig. 4). Membranes containing 0.5%, 1%, 2%, and 3% of ZnO-NP showed no significant cytotoxicity effect ($p > 0.05$). Cell viability decreased significantly over 7 days for the 4% group compared to the control ($p < 0.01$). Scaffolds containing 2% of ZnO-NPs showed the best compatibility compared to other groups. Therefore, PEO/ZnO-NPs containing 2% of nanoparticles were selected for further studies.

Cell attachment and morphology

The adhesion and morphology of human fibroblast cells were analyzed with SEM. Figure 5 shows the attachment of cells onto the PEO and PEO/ZnO-NP (containing 2% of nanoparticles) membranes.

Characterization of the electrospun membranes

ATR-FTIR analysis

The ATR-FTIR spectra of PEO and PEO/ZnO-NPs electrospun membranes are presented in Fig. 6. The spec-
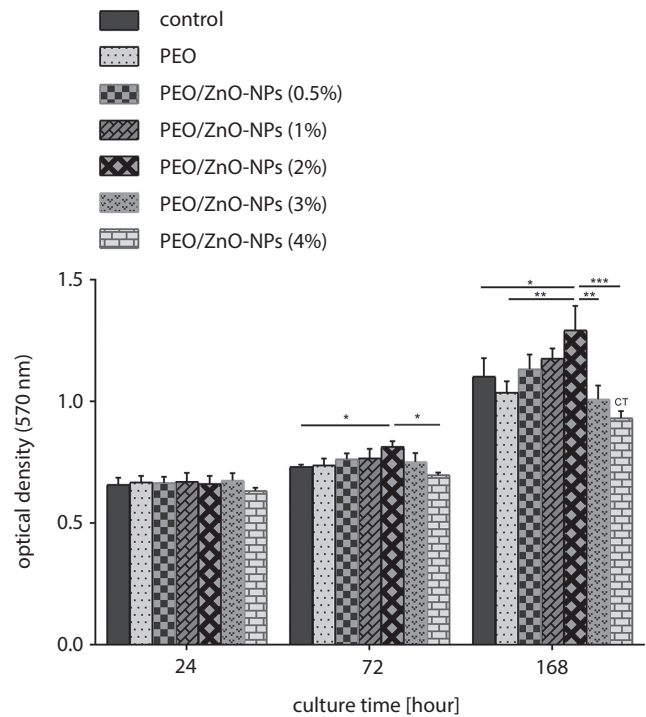

Fig. 4. In vitro cytotoxicity and cell viability of the scaffolds. MTT assay results for adult skin fibroblast proliferation on PEO and PEO/ZnO-NPs fibers and control. Data is shown as mean ±SD (n = 3)

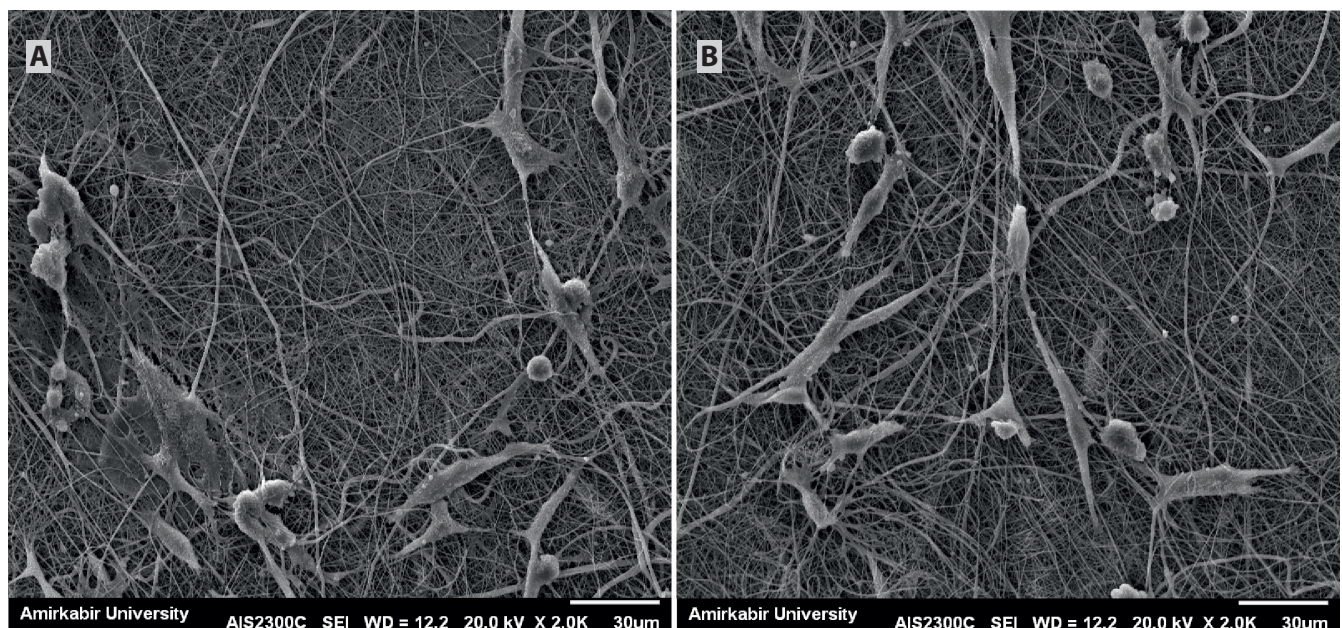*$p < 0.05$; **$p < 0.01$; ***$p < 0.001$; CT – cell toxicity.

Fig. 5. SEM micrographs of cell attachment onto (A) PEO fibers and (B) PEO/ZnO-NPs (2%) scaffolds

Fig. 6. ATR-FTIR spectra of (A) PEO and (B) PEO/ZnO-NPs (2%) fibers

Fig. 7. Mechanical properties of electrospun PEO and PEO/ZnO-NPs (2%) fibers before and after cross-linking

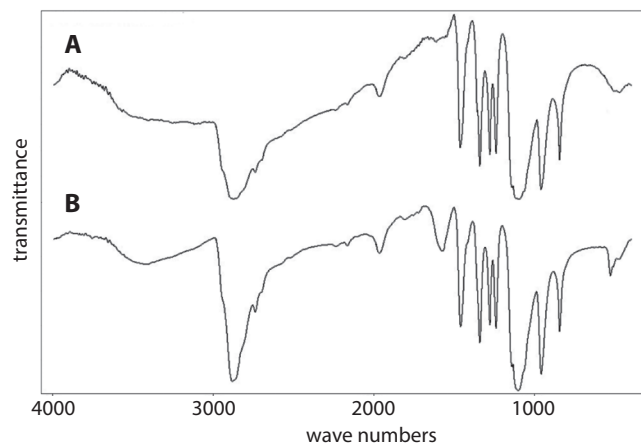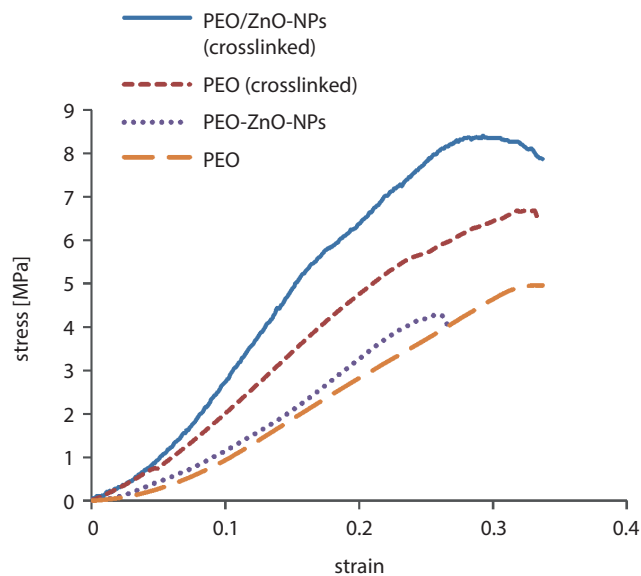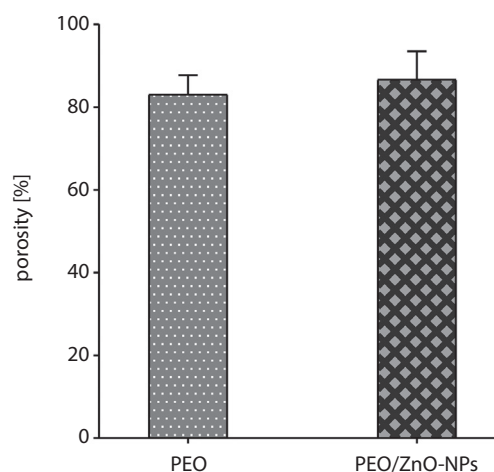Fig. 8. The porosity of electrospun fibers: (A) PEO and (B) PEO/ZnO-NPs (2%)

trum of the pure PEO (Fig. 6A) shows characteristic peaks in the regions of 1462 cm^{-1}, 1342 cm^{-1}, 1280 cm^{-1}, and 844 cm^{-1} that represent different bonds of CH_2 in scissoring, wagging, twisting, and rocking forms. The sharp peak at 2881 cm^{-1} is related to CH stretching, and the smooth peak at 3464 cm^{-1} shows the presence of the OH group. Other peaks at 1141 cm^{-1}, 1095 cm^{-1} and 956 cm^{-1} are related to C–O–C stretching, which are responsible for the semi-crystalline phase of PEO.[19] The spectrum of the PEO/ZnO-NPs (Fig. 6B) displays the characteristic peaks of ZnO-NPs at 3410 cm^{-1} (OH groups on the surface), 1577 cm^{-1} (Zn hydroxo-acetate complex) and 528 cm^{-1} (Zn–O bond).[20]

Mechanical properties

The PEO membranes showed a Young Modulus of 13.72 ±3.11 MPa, whereas cross-linked ones showed a value of 24.98 ±4.26 MPa, which indicated a statistically significant difference after crosslinking (p < 0.05). Similar changes were observed for PEO/ZnO-NPs scaffolds, which were 15.67 ±2.96 MPa before crosslinking and 28.15 ±4.49 MPa for the cross-linked scaffolds (p < 0.05) (Fig. 7).

Determination of scaffolds porosity

Porosities of the PEO and PEO/ZnO-NPs scaffolds were determined using the ethanol displacement method.[21] As seen in Fig. 8, the PEO membranes revealed a porosity of 83.10 ±3.50%. Incorporation of ZnO-NPs slightly increased the porosity of the membrane to 86.78 ±7.42%. This increase was not statistically significant (p > 0.05).

Wettability of membrane surface

The electrospun PEO and PEO/ZnONP membranes showed water contact angle values of 41.06 ±3.26° and 35.41 ±3.44°, respectively (Fig. 9).

Protein adsorption

The BCA assessment kit for protein adsorption revealed a time-dependent increase in adsorbed albumin after 0.5 h, 1 h, 2 h, 6 h, and 24 h of incubation for both membranes. No statistically significant changes were detected at different times between the 2 groups (p > 0.05). The results are presented in Fig. 10.

Discussion

When engineered scaffolds are used as skin substitutes or wound dressings, they are meant to protect the injured site from infection, moisture loss and physical damage. They are also supposed to support the wound mechanically. Cell attachment, as a key issue in the healing process, is affected by the porosity and surface hy-
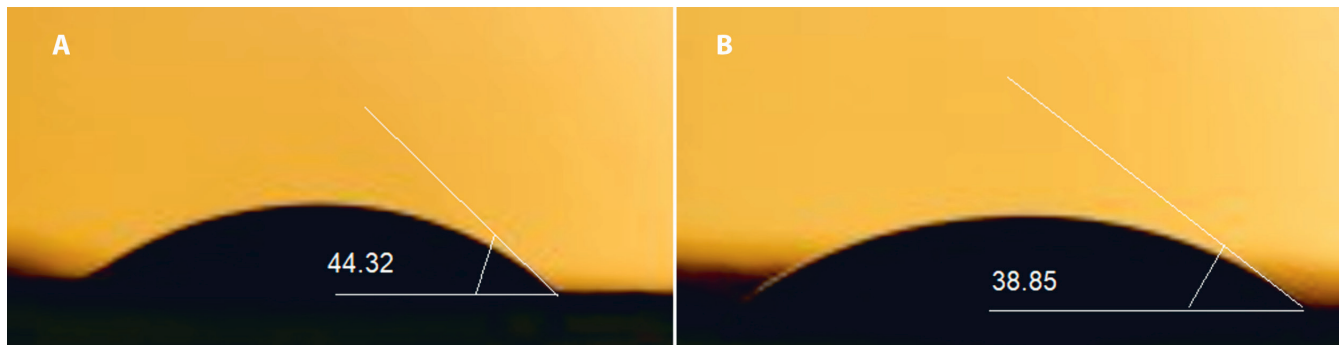
Fig. 9. Contact angles of deionized water droplet on (A) PEO and (B) PEO/ZnO-NP (2%) membranes
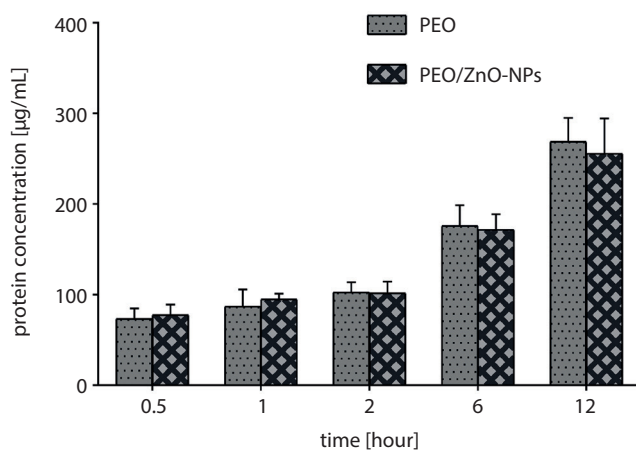

Fig. 10. Protein adsorption on the membrane surface. Amount of albumin absorbed on the surface of scaffolds after 0.5 h, 1 h, 2 h, 6 h, and 12 h

drophilicity of the substrate.[22] A wide range of materials and various techniques are used to produce such scaffolds. In the present study, antibacterial electrospun scaffolds were fabricated using PEO as the main supportive biomaterial and ZnO-NPs as the antibacterial agent. Poly(ethylene) glycol confers to the membrane good mechanical properties, preserves wound moisture and mimics native ECM topography.[23,24] The porous structure of the PEO and PEO/ZnO-NP scaffolds was designed to be able to promote the exchange of gas and nutrients, and to support cell proliferation and migration. Biological assessments and in vitro characterization of membranes were performed to evaluate their suitability for skin tissue engineering.

The results of the SEM analysis and the DLS demonstrate the nanosize of the particles that make them ideal for incorporation into electrospun fibers (Fig. 1). Thinner fibers were fabricated by incorporating ZnO-NPs due to a slight decrease in the viscosity of the solution (Fig. 2A,C). Scanning electron microscopy images of the cross-linked scaffolds (Fig. 2B,D) confirm the suitable method of crosslinking for PEO and PEO/ZnO-NP nanofibers. Other studies had previously reported a similar effect on the diameter of synthetic polymer fibers when nanoparticles or other agents were added to the so-

lution.[8] Furthermore, the nanofibers produced in the current study have an average diameter comparable to that of the collagen fibers present in native ECM (60–400 nm). Son et al. developed ultrafine nanofibrous membranes by electrospinning PEO dissolved in different types of solvents.[25] The average diameters were close to those in the current study.

Skin is the first barrier against microorganisms. Microorganism invasion could occur during wound healing and interfere with the healing process. Therefore, antibacterial activity is a significant advantage for a wound dressing or skin scaffold.[26,27] The PEO membrane had no bactericidal impact. The inhibition zone for E. coli and S. aureus increased slightly with increasing ZnO-NPs (Fig. 3). Therefore, the antibacterial activity of the PEO/ZnO-NPs could be attributed to the nanoparticles of ZnO. Other investigations have demonstrated the bactericidal properties of these nanoparticles when they are incorporated into other natural or synthetic polymers.[11,28,29] The greatest inhibition zone belongs to the PEO/ZnO-NP membrane with 4% w/w of nanoparticles. The MTT assay results, however, showed cell toxicity effects. The optimum cell-compatible concentration of ZnO-NPs with no toxicity was 2% w/w with inhibition zones of 3.67 mm and 3.21 mm for E. coli and S. aureus, respectively (Table 1). Other studies have shown the dose-dependent cytotoxicity of ZnO-NPs for human epidermal keratinocytes and lung epithelial cells.[30] Some other studies have shown the cytotoxicity of these nanoparticles in different cell types.[31,32] As a result, the PEO membrane comprised of 2% w/w ZnO-NPs was chosen for further studies.

Interaction between cells and ECM components is critical for stabilizing the three-dimensional structure and retrieving tissue function during tissue remodeling in the wound healing process.[33,34] A skin scaffold should improve cell adhesion, proliferation and migration to enhance the wound healing process. Scanning electron microscopy images revealed the adhesion of human fibroblast cells to the PEO/ZnO-NP membrane containing 2% nanoparticles (Fig. 5). Fibroblast cells are responsible for the synthesis of collagen and ECM bio-macromolecules as well as the secretion of adherent proteins such as fibronectin.[35] Therefore, the cell compatibility of the membrane

keeps the normal rate of ECM synthesis, which is necessary for skin regeneration at the wounded site. The attachment of fibroblast cells revealed the compatibility of the electrospun membranes, confirming the results of the cell viability test. Cells exhibited normal morphology of fibroblasts on PEO and PEO/ZnO membranes (Fig. 5).

Skin scaffolds and wound dressings must have appropriate mechanical properties to support the healing process as well as the structures found in skin layers such as vessels and nerves.[8,36] Herein, the mechanical properties of cross-linked and non-cross-linked electrospun scaffolds were evaluated and are presented in Fig. 7. At first glance, it is clear that cross-linked scaffolds exhibit higher mechanical parameters. As expected, the crosslinking of the membranes significantly improved their mechanical properties, which are comparable to those of native skin. The presence of ZnO-NPs increased the Young modulus. Using wound dressings or scaffolds with great differences in mechanical properties leads to side effects caused by the stress-shielding mechanism during tissue regeneration.[37] The excellent mechanical properties of the produced membranes could be attributed to the presence of a synthetic polymer (PEO) and the appropriate crosslinking protocol.[38] The literature shows that metal nanoparticles enhance the mechanical characteristics of polymer nanofibers,[39,40] but this was not significant in the current study due to the low concentration of ZnO-NPs.

The porosity of scaffolds is crucial to accommodate cells and facilitate their migration as well as the exchange of gas and nutrients.[15] Incorporating ZnO-NPs increased the porosity of the membrane, which can be explained by a lower diameter of PEO/ZnO-NP fibers and wider spaces between them. Other investigations have previously revealed that scaffolds with more than 90% porosity could provide the best opportunity for cell migration, ECM production, and gas and nutrient exchange for skin regeneration.[41,42] In the current research, PEO/ZnO-NP membranes displayed porosity close to 90% (Fig. 8), which demonstrates the suitability of the membrane for use in skin tissue engineering applications.

The physicochemical properties of the scaffold surface affect cell adhesion, proliferation and differentiation.[43] Wettability is one of the most significant features of the surface of the material.[44] Measuring water contact angle determines the surface wettability.[45] According to other studies, moderate hydrophilic surfaces with a water contact angle between 30° and 70° have been shown to encourage cells to adhere and expand. Surface hydrophobicity and high hydrophilicity exhibit lower cell adhesion.[46,47] In the current study, the electrospun PEO and PEO/ZnO-NP membranes showed water contact angle values similar to those of moderate hydrophilic substrates (Fig. 9). Such hydrophilicity could be attributed to the presence of functional groups such as hydroxyl groups. The presence of ZnO-NPs in the structure decreased the water contact angle (increased hydrophilicity) due to the presence of hydroxyl groups on its surface.[48] In addition to cell adhesion, hydrophilic biomaterials can also provide the required moisture during the wound healing process.[49]

Body fluids contain large amounts of protein. Skin scaffolds and wound dressings are exposed to body fluids when they are placed at the wounded site, and protein adsorption begins immediately. The biological compatibility and cell adhesion of the material are directly affected by protein adsorption. Cells attach to the adsorbed proteins through their integral receptors, which anchor specific amino acids in the structure of adhesive proteins such as fibronectin.[8] Albumin, the most abundant serum protein, is accumulated at the injured site during the primary phase of the wound healing process. The absorbed albumin is then replaced by cell adhesive proteins.[50]

The current results revealed that albumin absorption increased with time (Fig. 10). As expected, no statistically significant changes were observed between PEO and PEO/ZnO-NP membranes due to their hydrophilic and porous surfaces. In addition to the moderate hydrophilicity (water contact angle measurement), the potential of these membranes for protein adsorption provides a qualified substrate for cell attachment, as shown in Fig. 5.
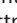
Conclusions

In the current investigation, the electrospinning technique was employed to fabricate scaffolds composed of PEO and ZnO-NPs. These membranes were supposed to mimic the native skin ECM in order to improve the wound healing process. To achieve the optimal concentration of incorporated ZnO-NPs, different concentrations of these nanoparticles were incorporated into PEO nanofibers and evaluated with disc diffusion and cell viability tests. The electrospun PEO containing 2% of ZnO-NPs exhibited antibacterial activity against *E. coli* and *S. aureus* without any toxicity to human fibroblast cells. Based on the results, the PEO membrane containing 2% of ZnO-NPs was selected as the most biocompatible scaffold for further studies.

Evaluation of the physicochemical properties of the PEO/ZnO-NPs also confirmed the suitability of this highly porous (86.78 ±7.42% porosity) membrane for use as a skin scaffold. The high porosity of the membrane facilitates cell migration, nutrients and gas exchange, and provides adequate space for new ECM formation. The PEO/ZnO-NP scaffold showed a water contact angle value of 35.41 ±3.44°. The moderate hydrophilicity of the membrane could improve cell adhesion. Young's modulus of the cross-linked membrane (28.15 ±4.49 MPa) indicates the appropriate mechanical support that can protect the wound during tissue remodeling and regeneration.

In conclusion, the PEO electrospun nanofibrous membrane containing 2% of ZnO-NPs showed suitable biological, physicochemical and mechanical properties as a skin scaffold. For further studies, the incorporation of alternative bioactive agents and molecules, such as vitamins, growth factors and ECM components, could improve the biological properties and enhance the performance of these electrospun membranes in skin tissue engineering.

ORCID iDs

Hamed Nosrati https://orcid.org/0000-0002-6952-1109
Mohammad Khodaei https://orcid.org/0000-0002-0598-8543
Mehdi Banitalebi-Dehkordi https://orcid.org/0000-0002-4109-1493
Morteza Alizadeh https://orcid.org/0000-0003-4214-6502
Shiva Asadpour https://orcid.org/0000-0001-5574-7142
Esmaeel Sharifi https://orcid.org/0000-0003-3400-3106
Jafar Ai https://orcid.org/0000-0001-8417-5913
Mostafa Soleimannejad https://orcid.org/0000-0002-9097-4356

References

1. Ehterami A, Salehi M, Farzamfar S, et al. Chitosan/alginate hydrogels containing alpha-tocopherol for wound healing in rat model. *J Drug Deliv Sci Technol*. 2019;51:204–213.
2. Dash BC, Setia O, Gorecka J, et al. A dense fibrillar collagen scaffold differentially modulates secretory function of iPSC-derived vascular smooth muscle cells to promote wound healing. *Cells*. 2020;9(4):966.
3. MacEwan MR, MacEwan S, Kovacs TR, Batts J. What makes the optimal wound healing material? A review of current science and introduction of a synthetic nanofabricated wound care scaffold. *Cureus*. 2017;9(10):e1736.
4. Keirouz A, Chung M, Kwon J, Fortunato G, Radacsi N. 2D and 3D electrospinning technologies for the fabrication of nanofibrous scaffolds for skin tissue engineering: A review. *Wiley Interdiscip Rev Nanomed Nanobiotechnol*. 2020;12(4):e1626.
5. Amiri N, Rozbeh Z, Afrough T, Sajadi Tabassi SA, Moradi A, Movaffagh J. Optimization of chitosan-gelatin nanofibers production: Investigating the effect of solution properties and working parameters on fibers diameter. *BioNanoScience*. 2018;8(3):778–789.
6. Vasita R, Katti DS. Nanofibers and their applications in tissue engineering. *Int J Nanomedicine*. 2006;1(1):15–30.
7. Okutan N, Terzi P, Altay F. Affecting parameters on electrospinning process and characterization of electrospun gelatin nanofibers. *Food Hydrocolloids*. 2014;39:19–26.
8. Miguel S, Ribeiro M, Coutinho P, Correia I. Electrospun polycaprolactone/aloe vera chitosan nanofibrous asymmetric membranes aimed for wound healing applications. *Polymers (Basel)*. 2017;9(5):183.
9. Miguel SP, Moreira AF, Correia IJ. Chitosan based-asymmetric membranes for wound healing: A review. *Int J Biol Macromol*. 2019;127:460–475.
10. Duan B, Dong C, Yuan X, Yao K. Electrospinning of chitosan solutions in acetic acid with poly(ethylene oxide). *J Biomater Sci Polym Ed*. 2004;15(6):797–811.
11. Augustine R, Malik HN, Singhal DK, et al. Electrospun polycaprolactone/ZnO nanocomposite membranes as biomaterials with antibacterial and cell adhesion properties. *J Polym Res*. 2014;21(3):347.
12. Ahmed R, Tariq M, Ali I, et al. Novel electrospun chitosan/polyvinyl alcohol/zinc oxide nanofibrous mats with antibacterial and antioxidant properties for diabetic wound healing. *Int J Biol Macromol*. 2018;120(Pt A):385–393.
13. Hwang J-J, Ma T-W. Preparation, morphology, and antibacterial properties of polyacrylonitrile/montmorillonite/silver nanocomposites. *Mater Chem Phys*. 2012;136(2–3):613–623.
14. Sharma M, Yadav S, Ganesh N, Srivastava MM, Srivastava S. Biofabrication and characterization of flavonoid-loaded Ag, Au, Au–Ag bimetallic nanoparticles using seed extract of the plant *Madhuca longifolia* for the enhancement in wound healing bio-efficacy. *Prog Biomater*. 2019;8(1):51–63.
15. Zafari M, Mansouri Boroujeni M, Omidghaemi S, et al. Physical and biological properties of blend-electrospun polycaprolactone/chitosan-based wound dressings loaded with N-decyl-N, N-dimethyl-1-decanaminium chloride: An in vitro and in vivo study. *J Biomed Mater Res B Appl Biomater*. 2020;108(8):3084–3098.
16. Antunes BP, Moreira AF, Gaspar V, Correia I. Chitosan/arginine-chitosan polymer blends for assembly of nanofibrous membranes for wound regeneration. *Carbohydr Polym*. 2015;130:104–112.
17. Liverani L, Lacina J, Roether JA, et al. Incorporation of bioactive glass nanoparticles in electrospun PCL/chitosan fibers by using benign solvents. *Bioact Mater*. 2018;3(1):55–63.
18. Samzadeh-Kermani A, Miri S. Synthesis, characterization and bactericidal property of chitosan-graft-polyaniline/montmorillonite/ZnO nanocomposite. *Korean J Chem Eng*. 2015;32(6):1137–1141.
19. Anžlovar A, Orel ZC, Kogej K, Žigon M. Polyol-mediated synthesis of zinc oxide nanorods and nanocomposites with poly(methyl methacrylate). *J Nanomater*. 2012;2012:31.
20. Kooti M, Naghdi Sedeh A. Microwave-assisted combustion synthesis of ZnO nanoparticles. *J Chem*. 2012;2013:562028.
21. Fradique R, Correia TR, Miguel S, et al. Production of new 3D scaffolds for bone tissue regeneration by rapid prototyping. *J Mater Sci Mater Med*. 2016;27(4):69.
22. Lin X, Li Y, Luo W, et al. Leucine-activated nanohybrid biofilm for skin regeneration via improving cell affinity and neovascularization capacity. *J Mater Chem B*. 2020;8(35):7966–7976.
23. Chang W, Ma G, Yang D, Su D, Song G, Nie J. Electrospun ultrafine composite fibers from organic-soluble chitosan and poly(ethylene oxide). *J Appl Polym Sci*. 2010;117(4):2113–2120.
24. Cha JH, Didwal PN, Kim JM, Chang DR, Park C-J. Poly(ethylene oxide)-based composite solid polymer electrolyte containing Li7La3Zr2O12 and poly(ethylene glycol) dimethyl ether. *J Membrane Sci*. 2020;595:117538.
25. Son WK, Youk JH, Lee TS, Park WH. The effects of solution properties and polyelectrolyte on electrospinning of ultrafine poly(ethylene oxide) fibers. *Polymer*. 2004;45(9):2959–2966.
26. Bray R. Antibacterial wound dressing. Google Patents; 2014.
27. Kazımoğlu H, Uysal E, Dokur M, Günerkan RH. Evaluation of the relationship between neutrophil lymphocyte ratio and the most common bacterial urinary tract infections after transplantation. *Bratisl Lek Listy*. 2019;120(2):161–165.
28. Bui VKH, Park D, Lee Y-C. Chitosan combined with ZnO, TiO₂ and Ag nanoparticles for antimicrobial wound healing applications: A mini review of the research trends. *Polymers (Basel)*. 2017;9(1):21.
29. Zhang X, Ren S, He X, et al. Preparation and characterization of cellulose nanofiber/zinc oxide composite films. *J Biobased Mater Bioenergy*. 2020;14(2):203–208.
30. Xia T, Kovochich M, Liong M, et al. Comparison of the mechanism of toxicity of zinc oxide and cerium oxide nanoparticles based on dissolution and oxidative stress properties. *ACS Nano*. 2008;2(10):2121–2134.
31. Lin W, Xu Y, Huang C-C, et al. Toxicity of nano-and micro-sized ZnO particles in human lung epithelial cells. *J Nanoparticle Res*. 2009;11(1):25–39.
32. Bondarenko O, Juganson K, Ivask A, Kasemets K, Mortimer M, Kahru A. Toxicity of Ag, CuO and ZnO nanoparticles to selected environmentally relevant test organisms and mammalian cells in vitro: A critical review. *Arch Toxicol*. 2013;87(7):1181–1200.
33. Ghalei S, Nourmohammadi J, Solouk A, Mirzadeh H. Enhanced cellular response elicited by addition of amniotic fluid to alginate hydrogel-electrospun silk fibroin fibers for potential wound dressing application. *Colloids Surf B Biointerfaces*. 2018;172:82–89.
34. Dill V, Mörgelin M. Biological dermal templates with native collagen scaffolds provide guiding ridges for invading cells and may promote structured dermal wound healing. *Int Wound J*. 2020;17(3):618–630.
35. Maione-Silva L, de Castro EG, Nascimento TL, et al. Ascorbic acid encapsulated into negatively charged liposomes exhibits increased skin permeation, retention and enhances collagen synthesis by fibroblasts. *Sci Rep*. 2019;9(1):522.
36. Niu X, Wei Y, Liu Q, et al. Silver-loaded microspheres reinforced chitosan scaffolds for skin tissue engineering. *Eur Polym J*. 2020;134:109861.
37. Elsner JJ, Zilberman M. Novel antibiotic-eluting wound dressings: An in vitro study and engineering aspects in the dressing's design. *J Tissue Viability*. 2010;19(2):54–66.

38. Bianco A, Calderone M, Cacciotti I. Electrospun PHBV/PEO co-solution blends: Microstructure, thermal and mechanical properties. *Mater Sci Eng C Mater Biol Appl*. 2013;33(3):1067–1077.

39. Dong H, Fey E, Gandelman A, Jones WE. Synthesis and assembly of metal nanoparticles on electrospun poly(4-vinylpyridine) fibers and poly(4-vinylpyridine) composite fibers. *Chem Mater*. 2006;18(8): 2008–2011.

40. Radwan-Pragłowska J, Janus L, Piatkowski M, Bogdal D, Matýsek D. Hybrid bilayer PLA/chitosan nanofibrous scaffolds doped with ZnO, Fe3O4, and Au nanoparticles with bioactive properties for skin tissue engineering. *Polymers (Basel)*. 2020;12(1):159.

41. Doulabi AH, Mirzadeh H, Imani M, Bagheri-Khoulenjani S. Chitosan/polyethylene glycol fumarate blend films for wound dressing application: In vitro biocompatibility and biodegradability assays. *Prog Biomater*. 2018;7(2):143–150.

42. Ababzadeh S, Farzin A, Goodarzi A, et al. High porous electrospun poly(ε-caprolactone)/gelatin/MgO scaffolds preseeded with endometrial stem cells promote tissue regeneration in full-thickness skin wounds: An in vivo study. *J Biomed Mater Res B Appl Biomater*. 2020; 108(1):2961–2970.

43. Tserepi A, Gogolides E, Bourkoula A, et al. Plasma nanotextured polymeric surfaces for controlling cell attachment and proliferation: A short review. *Plasma Chem Plasma Processing*. 2015;36.

44. Rahimipour S, Salahinejad E, Sharifi E, Nosrati H, Tayebi L. Structure, wettability, corrosion and biocompatibility of nitinol treated by alkaline hydrothermal and hydrophobic functionalization for cardiovascular applications. *Appl Surface Sci*. 2020;506:144657.

45. Talebi A, Labbaf S, Karimzadeh F. Polycaprolactone-chitosan-polypyrrole conductive biocomposite nanofibrous scaffold for biomedical applications. *Polym Composites*. 2020;41(2):645–652.

46. Kumbar SG, Nukavarapu SP, James R, Nair LS, Laurencin CT. Electrospun poly(lactic acid-co-glycolic acid) scaffolds for skin tissue engineering. *Biomaterials*. 2008;29(30):4100–4107.

47. Miguel SP, Ribeiro MP, Brancal H, Coutinho P, Correia IJ. Thermoresponsive chitosan-agarose hydrogel for skin regeneration. *Carbohydr Polym*. 2014;111:366–373.

48. Ennaceri H, Wang L, Erfurt D, et al. Water-resistant surfaces using zinc oxide structured nanorod arrays with switchable wetting property. *Surf Coat Technol*. 2016;299:169–176.

49. Jones V, Grey JE, Harding KG. ABC of wound healing: Wound dressings. *BMJ*. 2006;332(7544):777–780.

50. Arima Y, Iwata H. Effect of wettability and surface functional groups on protein adsorption and cell adhesion using well-defined mixed self-assembled monolayers. *Biomaterials*. 2007;28(20):3074–3082.

Polimery w Medycynie

Polymers in Medicine